Boundary Conditions and Multi-Scale Modeling for Micro-and Nano-flows

by

Lin Guo

A dissertation submitted to The Johns Hopkins University in conformity with the requirements for the degree of Doctor of Philosophy.

Baltimore, Maryland

March, 2016

Abstract

The development of micro- and nanofluidic devices requires detailed knowledge of interfacial phenomena. This thesis addresses two important effects at wall-fluid interfaces, boundary slip and electroosmosis, through numerical simulations.

The first study uses molecular dynamics (MD) simulations to probe the influence of surface curvature on the slip boundary condition for a simple fluid. The slip length is measured for flows in planar and cylindrical geometries. As wall curvature increases, the slip length decreases dramatically for close-packed surfaces and increases slightly for sparse ones. The magnitude of the variation depends on the crystallographic orientation and the flow direction. The different patterns of behavior are related to the curvature-induced variation in the ratio of the spacing between fluid atoms to the spacing between minima in the potential from the solid surface. The results are consistent with a microscopic theory for the viscous friction between fluid and wall that expresses the slip length in terms of the lateral response of the fluid to the wall potential and the characteristic decay time of this response.

The second study performs MD simulations to explore the effective slip boundary conditions over surfaces with one-dimensional sinusoidal roughness for two different flow orientations: transverse and longitudinal to the corrugations, and different atomic geometries of the wall: smoothly bent and stepped. The results for the sparse

ABSTRACT

bent surfaces quantitatively agree with the continuum predictions with a constant local boundary condition. The effective slip length decreases with increasing corrugation amplitude, and the reduction is larger for the transverse direction. Atomic effects become significant for the close-packed bent and for the stepped surfaces, which may even enhance the effective slip along the longitudinal direction.

In the third study, an efficient multi-scale method is developed to simulate electroosmotic flows. MD is used in the near wall region where the atomistic details are important, while continuum incompressible fluctuating hydrodynamics is applied in the bulk region. The two descriptions are coupled in an overlap region. Because of the low ion density and the long-range of electrostatic interactions, discrete ions are retained in the bulk region and simulated by a stochastic Euler-Lagrangian method (SELM). The MD and SELM descriptions seamlessly exchange ions in the overlap region. This hybrid approach is validated against full MD simulations for different geometries and types of flows. [1]

Thesis Advisor: Professor Mark O. Robbins

Thesis Advisor: Professor Shiyi Chen

Thesis Reader: Professor Andrea Prosperetti

[1]This material is based on work supported by the National Science Foundation under Grants No. DMR-1411144 and No. DMR-1006805.

Acknowledgments

First, and foremost, I would like to express my sincere and deepest gratitude to my advisors, Professors Mark O. Robbins and Shiyi Chen. Their guidance, patience, and encouragement have supported me to grow throughout this dissertation process, as well as the entire graduate training.

I would also like to thank all the faculty and staff members, both in the Mechanical Engineering and the Physics and Astronomy departments, for their kind help during my Ph.D. study. In particular, I would like to thank Professor Andrea Prosperetti for serving as my dissertation reader. I want to thank Professors Charles Meneveau, Joseph Katz, Omar M. Knio, Cila Herman and Lester Su, for spending time teaching me.

Thank you to our research group members, Jin Liu, K. Michael Salerno, Ting Ge, Lars Pastewka, Tristan A. Sharp, Thomas O'Connor, Joel Clemmer, Vikram Jadhao, Joseph Monti and Marco Aurelio Galvani Cunha. I appreciate all their help and the motivating and fun environment in which to learn and grow.

Finally, I would like to express my heartfelt gratitude to my family, particularly my wife, for their love and support along the way.

Contents

List of Tables

List of Figures

Chapter 1

Introduction

Studies of fluid transport in micro-and nano-systems have recently received great attention due mainly to modern developments in micro-and nano-technologies. At these small scales, interfacial effects become increasingly important because of the greatly magnified surface-volume ratio. This results in special flow phenomena, fundamentally different from macroscopic flows, which generate a wide range of opportunities for applications from biomedical engineering to energy technology.[1–8] As the characteristic dimensions approach molecular or atomic size, the continuum descriptions become inadequate, and the discrete nature of matter in the finite interfacial regions cannot be neglected.

This thesis addresses two important interfacial effects at solid surfaces: boundary slip and electroosmosis. The thesis is organized as follows. In the remaining part of this chapter, we briefly introduce the topics of the studies. Chapters 2 and 3 present molecular dynamics (MD) studies of slip boundary conditions over curved surfaces and effective slip boundary conditions over sinusoidally corrugated surfaces, respectively. In Chapter 4, a multi-scale method is developed to accelerate simulations of electroosmotic flows.

1.1 Slip Boundary Condition

Solving the continuum hydrodynamic equations requires boundary conditions at the bounding walls. The traditional no-slip boundary condition assumes that the liquid at the surface moves with the same velocity as the surface, and has been proved to be very successful at describing flows at the macroscopic level. However, the assumption is phenomenological and cannot be derived from first principles. Numerous experiments have reported that slip, i.e., a tangential velocity of the fluid at the surface deviating from that of the solid wall, may occur and become significant at micro-and nano-scales.[6–20] Slip is very important in micro- and nanofluidics since it can dramatically reduce the force required to drive fluid flows.

For a Newtonian fluid over a flat surface, Navier proposed the first and the most widely used slip boundary condition.[21] He argued that the frictional force between the fluid and wall is proportional to the slip velocity of the fluid, and it is balanced by the viscous stress within the fluid. Applying Newton's law of viscosity for the bulk fluid, he concluded that the slip velocity is proportional to the shear rate of the fluid at the surface. The slip length L_s (also referred to as intrinsic slip length) is introduced as the ratio of the viscosity over the friction coefficient, and is used to characterize the degree of interfacial slip. For the planar flow geometry, the slip length measures the distance from the actual surface to the virtual plane where the extrapolated fluid velocity would equal that of the solid surface.

Understanding slip behavior requires probing the atomic details of liquids at the surface, where molecular dynamics (MD) simulations become a powerful tool. Molecular dynamics studies for atomically flat surfaces[22–27] have indicated that when the shear rate is small, the slip length is flow-independent and only depends on the properties of the fluid (e.g., viscosity, temperature, fluid structure) and the microscopic properties of the local interface (e.g., wall-fluid interaction strength, atomic structure of the surface).

Panzer *et al.*[28,29] extended the Navier slip boundary condition to curved surfaces, with the rate of strain tensor modified corresponding to the local curvature of the surface. The slip length can be assumed to be the same as on the flat surface only if the surface normal changes on length scales that are much larger than the atomic scale and all the microscopic properties remain the same. These assumptions may not hold when the radius of curvature of the surface approaches the molecular-scale. Previous MD simulations have reported contradictory results. Falk *et al.* found very large changes with slip length in axial flow along nanotubes.[30,31] However, a more recent study by Chen *et al.* reported that slip length barely changes with curvature.[32]

In Chapter 2, molecular dynamics simulations are used to investigate the influence of surface curvature on the slip boundary condition for a simple fluid. The slip length is measured for flows in planar and cylindrical geometries with a range of wall-fluid interactions. As wall curvature increases, the slip length decreases dramatically for close-packed surfaces and increases slightly for sparse ones. The magnitude of the

changes depends on the crystallographic orientation and is different for flow along and perpendicular to the direction of curvature. These different patterns of behavior are related to the curvature-induced variation in the ratio of the spacing between fluid atoms to the spacing between minima in the potential from the solid surface. The results are consistent with a microscopic theory[33,34] for the viscous friction between fluid and wall that expresses the slip length in terms of the lateral response of the fluid to the wall potential and the characteristic decay time of this response.

1.2 Effective Slip Boundary Condition

In real experiments, most solid surfaces have finite roughness down to nanometer scales. It is of practical interest to use an effective slip boundary condition to account for the mean effects from the variations along the real surface.[35–40] The effective slip length L_{eff} measures the distance from the location of the mean height of the surface roughness to the virtual plane where the extrapolated velocity from the bulk flow profile coincides with that of the solid wall. A larger (more positive) effective slip length corresponds to a smaller hydrodynamic drag coefficient between the fluid and wall.

Many studies have been carried out on the effect of roughness on L_{eff}, but no simple and unique conclusion has been drawn. It is widely reported that wall roughness decreases the degree of effective slip in the Wenzel state,[18,35,37,38,41–46] whereas highly hydrophobic rough surfaces may trap gas bubbles and form a Cassie state, which can

dramatically enhance the effective slip.[47–58] In contrast, it has also been reported that roughness may generate very large effective slip even in the Wenzel state.[59,60] The effective slip length can become anisotropic over surfaces with anisotropic corrugations.[39,57,61–67]

In Chapter 3, molecular dynamics simulations are performed to explore the effective slip boundary conditions for a simple fluid over surfaces with one-dimensional sinusoidal roughness in the Wenzel state. Different types of corrugated surfaces are compared: smoothly bent surfaces where atoms of a crystalline solid are displaced to follow a sine wave, and stepped surfaces that are cut from a crystalline solid. The wavelength is more than an order of magnitude larger than the atomic diameter, so that the atomic-scale roughness can be separated from the large scale roughness. The wall density and the wall-fluid interaction are varied.

The behavior of the effective slip length is explored by shearing the fluid along two different orientations: transverse and longitudinal to the corrugations. The results for sparse bent surfaces quantitatively agree with continuum hydrodynamic predictions with a constant local boundary condition. The effective slip length decreases monotonically with increasing corrugation amplitude and the reduction is weaker for the longitudinal direction. Atomic effects become significant for the close-packed bent surfaces and for the stepped ones. Very anisotropic behavior can be found: the effective slip is strongly suppressed in the transverse direction, but remarkably increased along the longitudinal direction. The findings in Chapter 2 can be applied for the

bent case, to incorporate the intrinsic variations in the local slip boundary condition, and then to construct a more accurate continuum model.

1.3 Electroosmotic Flow

Electroosmotic transport in micro-and nano-channels has important applications in biological and engineering systems.[68–76] It is facile to control and its efficiency scales more favorably with system size for small systems than the conventional pressure driven flow.

For an electrolyte solution on a dielectric solid surface, an electrical double layer (EDL) can be formed at the interface, due to an electrochemical potential difference between the solid and liquid phases.[77,78] The solid surface becomes charged and the counterions in the solution are attracted until they screen the electric field created by the surface charge. Electroosmotic flow is the bulk liquid motion that is generated when an externally applied electric field drags the net surplus of counterions in the diffuse part of an electrical double layer. In general, the continuum description of electroosmotic flows is given by the Poisson-Boltzmann (PB) equation combined with the Navier-Stokes (NS) equations.[77,79–88]

The driving force for electroosmotic flow is greatest at the wall-fluid interface, where the continuum approximations break down and discrete atomic effects become significant.[89–94] For example, the ion distribution may be influenced by the strong electrostatic interactions and the finite sizes of the discrete molecules, and the trans-

port properties of the fluid molecules may be affected by their ordered structure near the surface. These atomic effects near the wall are of essential importance for the accurate modeling of the fluid flow over the whole channel domain, because the electroosmotic effect mainly takes place in the region very close to the surface where the charge concentration is highest.

1.4 Multi-Scale Simulation

Molecular dynamics simulations have become a powerful tool for studying nanoscale physical phenomena.[95,96] As long as accurate interaction potentials are implemented, they can fully resolve the atomic details and provide accurate results. However, because of the high computational cost, MD simulations can only probe very limited length and time scales (e.g., tens of nanometers and tens of nanoseconds), which are much below the requirement for most systems of experimental or practical interest.

To overcome this challenge in simulating fluid dynamics problem, a variety of multi-scale hybrid methods have been developed in the past two decades. A key characteristic of these hybrid methods is that they aim to take advantage of both the efficiency of the continuum description and the accuracy of molecular dynamics by dynamically coupling them with each other. In general, there are two categories of methods under the hybrid framework: the domain-decomposition-based[97–117] and the Euler-Lagrangian-decomposition-based methods.[118–132]

Typically, the domain-decomposition-based method uses MD to accurately resolve

the important atomistic details in a small region of the system, which is embedded into or coupled with a coarse-grained continuum description. The solutions of the different descriptions are forced to match in a certain overlap region. The Euler-Lagrangian methods are usually designed to simulate solute-solvent systems: the solute is modeled with the Lagrangian particle approach while the solvent is coarse-grained and simulated as a continuum fluid on a Eulerian mesh.

In Chapter 4, a multi-scale method is developed to simulate electroosmotic flows. The method combines both types of hybrid schemes. Specifically, the whole simulation domain is decomposed to the near-wall and bulk subdomains. Molecular dynamics is used in the near-wall subdomain where the atomistic details are important, while the continuum hydrodynamics are solved in the bulk region. The two descriptions are coupled in a finite overlap region. A discrete description of ions is retained in the continuum bulk region because of the low density of ions and the long-range of electrostatic interactions. A stochastic Euler-Lagrangian method (SELM) is used to simulate the dynamics of these ions suspended in the implicit continuum solvent. The stochastic Euler-Lagrangian and molecular dynamics descriptions freely exchange charges in the middle of the overlap region. To incorporate effects of hydrodynamic fluctuations on the diffusive transport of the SELM ions, incompressible fluctuating NS equations are implemented for the bulk continuum hydrodynamics. This hybrid approach is validated against full molecular dynamics simulations for different geometries and types of flows.

Chapter 2

Slip Boundary Conditions over Curved Surfaces

2.1 Introduction

Modern developments in micro- and nanotechnologies have created great interest in studying and modeling fluid transport at these small scales. Solving continuum hydrodynamic equations requires boundary conditions at solid-fluid interfaces. As the system size shrinks to micro- or nanoscales, these boundary conditions play increasingly important roles because of the large surface-volume ratio. The traditional no-slip boundary condition for macroscopic flows may break down, and a slip boundary condition is then needed to describe the fluid velocity at the solid surface.[1,6,7,133,134]

Navier proposed the first and the most widely used slip boundary condition,[21] which states that the slip velocity is proportional to the shear rate of the fluid at the surface. The slip length is introduced as the proportionality coefficient and is used to characterize the degree of fluid slip at the surface. In the simple case of flow past a flat surface, the slip length measures the distance from the actual surface to

the virtual plane where the extrapolated fluid velocity would equal that of the solid surface.

Molecular dynamics studies for flat surfaces [22–27] have indicated that when the shear rate is small, the slip length is flow-independent and only depends on the properties of the fluid (e.g., viscosity, temperature, and fluid structure) and the microscopic properties of the local interface (e.g., wall-fluid interaction strength and atomic structure of the surface). For surfaces with more complicated geometries, one can apply the Navier slip boundary condition locally with the same slip length but only if the surface normal changes on length scales that are much larger than the atomic scale and all the microscopic properties remain the same.[28,29] This geometrical independence is of practical importance. For example, one can measure the local slip length from a surface with a simple geometry (e.g., cylindrical for surface forces apparatus experiments, spherical for atomic force microscopy experiments),[6,7,19,135] and use it as the local intrinsic property for other surfaces as long as they are microscopically the same.

In the limit where the radius of curvature of the surface approaches the molecular-scale, the separation of the characteristic length scales fails and the small scale curvature becomes one of the microscopic properties of the surface. Some simulations suggest that curvature may affect the local slip length.[30,31,35,37] In particular, Falk *et al.* found very large changes with slip length in axial flow along nanotubes.[30,31] A more recent study[32] argued that these nanotubes were so slippery that no velocity

gradient occurred in the fluid and the effective slip length was infinite. The authors argued that slip was a material property and presented MD simulations that showed almost no change in slip length with curvature.

In this chapter, we present MD simulations of slip over curved solids with a wide range of solid/fluid interactions and solid geometries. Curved walls are generated by smoothly rolling up planar walls into cylinders while preserving the local atomic structure of the surface. Studies of flow between cylinders give slip boundary conditions at walls with negative (outer) and positive (inner) curvature. Both axial flow along the cylinder and rotational Couette flow are studied.

We find very different changes in slip length with curvature for different surfaces and different flow directions. As curvature increases there can be little change in slip length, as found by Chen *et al.*,[32] large decreases in slip length, as found by Falk *et al.*, or increases in slip length. The key factor is the ratio of the lateral spacing between minima in the wall potential to the spacing between fluid atoms. Slip is suppressed when these spacings are comparable and fluid atoms can lock in registry with the substrate.[22,30,31,33,34] Curvature increases the spacing between minima, which may enhance or suppress locking. Since curvature does not affect the spacing along the cylinder axis, the change in slip length can be much greater for rotational flow around the cylinder than for axial flow.

All of the simulation results can be collapsed using a theory for friction between a solid and fluid layer.[33,34] In this theory the key measure of the strength of viscous

coupling between fluid and solid is the magnitude of lateral density modulations in the first fluid layer due to the periodic potential from the solid. Most of the variation in slip length with curvature is related to changes in this response. Slip also depends on the lifetime of these density modulations which is found to be a material property of the fluid, depending only on the ratio of the spacing between solid atoms to the mean spacing between fluid atoms. The relation between this theory and the later work of Falk *et al.*[30,31] is discussed.

The chapter is organized as follows. In Sec. 2.2, we describe the details of molecular dynamics simulations, and how key quantities such as fluid layering, lateral structure factor and slip length are defined and measured from the simulations. In Sec. 2.3, results for slip length and fluid structure are presented and the behavior of the slip length is interpreted by a microscopic theory. The summary and conclusions are given in Sec. 2.4.

2.2 Details of molecular simulations

2.2.1 Interaction Potentials and Equations of Motion

We use standard molecular dynamics to simulate simple fluid flows over rigid solid walls. The simulations are performed using LAMMPS from Sandia National Laboratories.[136] A truncated Lennard-Jones (LJ) potential is used to model the

Wall Type	ϵ_{wf}/ϵ	σ_{wf}/σ	$r_{c,wf}/\sigma$
A	0.1	1	2.2
B	0.4	1	2.2
C	0.4	1	1.12
D	0.057	1.27	2.2

Table 2.1: The four sets of wall-fluid interaction parameters (subscript wf) studied in this chapter. The energy ϵ_{wf}, interaction length σ_{wf} and cutoff distance $r_{c,wf}$ are normalized by the fluid interaction energy ϵ and length σ. The surface lattice spacing was $a/\sigma = 0.75$, 0.86, 1.0, 1.09 or 1.20. For walls aligned with the (110) direction along the cylinder axis the inner and outer cylinder radii are 3.85σ and 23.0σ or 7.67σ and 26.83σ. For the (100) direction along the axis, the radii are 4.09σ and 21.69σ or 8.14σ and 25.75σ. The surface corrugation is decreased and slip length increased when ϵ_{wf} is decreased or σ_{wf} is increased.

interactions between fluid atoms:

$$V_{LJ}(r) = 4\epsilon\left[\left(\frac{\sigma}{r}\right)^{12} - \left(\frac{\sigma}{r}\right)^{6}\right] - V_c, \text{ for } r < r_c \tag{2.1}$$

where r is the distance between the two atoms and ϵ and σ define the characteristic energy and length scales of the fluid, respectively. V_{LJ} is truncated at a distance $r_c = 2.2\sigma$ to save computational cost, and V_c is chosen so that $V_{LJ}(r_c) = 0$. Wall (w) and fluid (f) atoms also interact through a truncated LJ potential with parameters ϵ_{wf}, σ_{wf} and $r_{c,wf}$. The four sets of wall-fluid interaction parameters studied are listed in Table 2.1. If not stated otherwise, then $\sigma_{wf} = 1\sigma$ and $r_{c,wf} = 2.2\sigma$.

The equations of motion are integrated using the velocity-Verlet algorithm with a time step $\Delta t = 0.005\tau$, where $\tau = \sigma\sqrt{m/\epsilon}$ is the characteristic time scale and m is the mass of a fluid atom. For most simulations, fluid temperature is maintained

at $T = 1.1\epsilon/k_B$ by imposing a Langevin thermostat on all fluid atoms in the flow-irrelevant y direction.[22,137] The thermostatted equation of motion in the y direction is given by

$$m\ddot{y} = f_{LJ} - m\Gamma\dot{y} + F(t) \tag{2.2}$$

where f_{LJ} is the total LJ force from all other particles. The damping rate Γ controls the heat flux between the system and the heat bath and $F(t)$ is a random force sampled from a Gaussian distribution with zero mean and variance $2m\Gamma k_B T/\Delta t$. We use a damping rate $\Gamma = 0.5\tau^{-1}$, which is small enough that the atomic motions are underdamped, but large enough to eliminate viscous heating. We checked that varying Γ by a factor of 2 does not change the results. Past studies of slip boundary conditions have shown there is little effect of thermostats on the low rate limit of interest here.[22,138,139] Effects are observed when rates are high enough that heating occurs.[138,139]

For simulations of axial flow between cylinders, instead of the Langevin thermostat, an isotropic dissipative particle dynamics (DPD) thermostat with a damping rate $0.5\tau^{-1}$ is applied on the fluid.[140–142] Thus the angular invariance of the fluid flow is preserved. Changes in damping rate and comparison to the Langevin results for flat surfaces confirmed that this thermostat has negligible impact (<2%) on the presented results for flow, slip length and fluid structure.

The bulk density of fluid is fixed at $\rho = 0.81\sigma^{-3}$. The strain rates in our simulations are low enough ($\lesssim 0.07\tau^{-1}$) to ensure that the bulk fluid is Newtonian with

shear viscosity $\mu \sim 2.13\epsilon\tau\sigma^{-3}$. In this low strain rate regime, linear response is also observed at the wall-fluid interface and the slip length is insensitive to shear rate.[22,23,27,32]

2.2.2 Planar Geometry

For the planar Couette geometry, fluid is confined in a channel between two solid walls parallel to the x-y plane (Figure 2.1(left)). Flow is generated by moving the top wall along x at a speed U_w. Periodic boundary conditions are imposed along x and y directions. Each planar wall consists of three (001) layers of a FCC crystal. Wall atoms are fixed rigidly to lattice sites. Past studies show thermal vibrations affect the value of slip length but do not change the trends with surface geometry and interactions.[22,26] The x axis is aligned with either the (110) or the (100) vector of the FCC lattice. We take the nominal height of the wall surfaces to coincide with the center of the wall atoms in the layer closest to the fluid. The separation distance between wall surfaces is $H = 30\sigma$. The spatial periods along the x and y directions are $L_x = L_y = 24.08\sigma$ and $L_x = L_y = 25.54\sigma$ for cases of flow along the (110) and (100) directions, respectively.

A key parameter of the wall is the lateral separation of the nearest neighbor atoms in the first layer, designated by the surface lattice spacing a. The surface lattice spacing determines the characteristic length of the atomic-scale corrugations in the wall potential felt by fluid atoms, and it has been disclosed to be an essential factor that regulates the degree of slip.[22] Here we investigate slip boundary conditions for

four values of the surface lattice spacing on the bottom wall ($a = 1.20\sigma$, 1.09σ,1.00σ, 0.86σ, and 0.75σ), and for various sets of the wall-fluid LJ parameters (Table 2.1). The results serve as the reference cases for flat surfaces, i.e., curvature $\kappa = 0$. For top wall surfaces, no-slip boundary conditions are always enforced by using large values of ϵ_{wf}.

2.2.3 Fluid Structure near Wall

2.2.4 Cylindrical Geometry

As shown in Figure 2.1(right), fluid is confined in the region between two coaxial cylindrical walls, whose central axes lie along the y axis. A periodic boundary condition with a period of length $L_y = 24.08\sigma$ or 25.54σ is applied along the y (axial) direction.

Each cylindrical wall is made by curving a planar wall along the x direction, while the atomic arrangement remains unchanged along the y direction. As depicted in Figure 2.2, the cylindrical wall is formed by three rolled-up layers of solid atoms, and the atoms of a given layer have the same radial distance from the central axis. Each layer consists of N_θ rows of atoms along the axial direction and the azimuth angle between neighboring rows is $2\pi/N_\theta$. The value of N_θ is chosen so the surface layer adjacent to the fluid has a locally square structure with nearest-neighbor spacing a. Two orientations of the flat wall relative to the cylindrical axis are considered. In the first, the nearest-neighbor direction, (110), is aligned with the axis. In the second, the next-nearest neighbor direction (100) is aligned with the axis. Carbon nanotubes

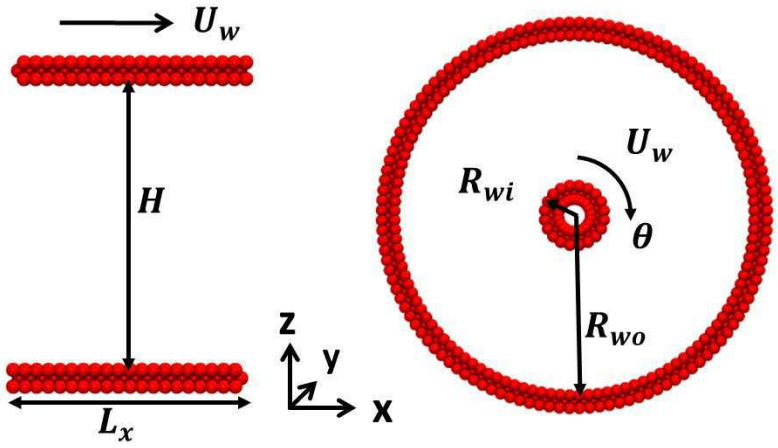

Figure 2.1: Geometry of planar (left) and cylindrical (right) geometries. In the planar case fluid is confined between rigid walls separated by height H and periodic boundary conditions are applied in the plane of the wall. Flow is generated by moving the top wall along x at a speed U_w. In the cylindrical case the walls are rigid coaxial cylinders with R_{wi} and R_{wo} the inner and outer radii of the solid surfaces, respectively. Angular and axial flow are generated by rotating the inner wall or translating it along the y axis, respectively, so surface atoms have speed U_w. Periodic boundary conditions are applied along the axial, y direction.

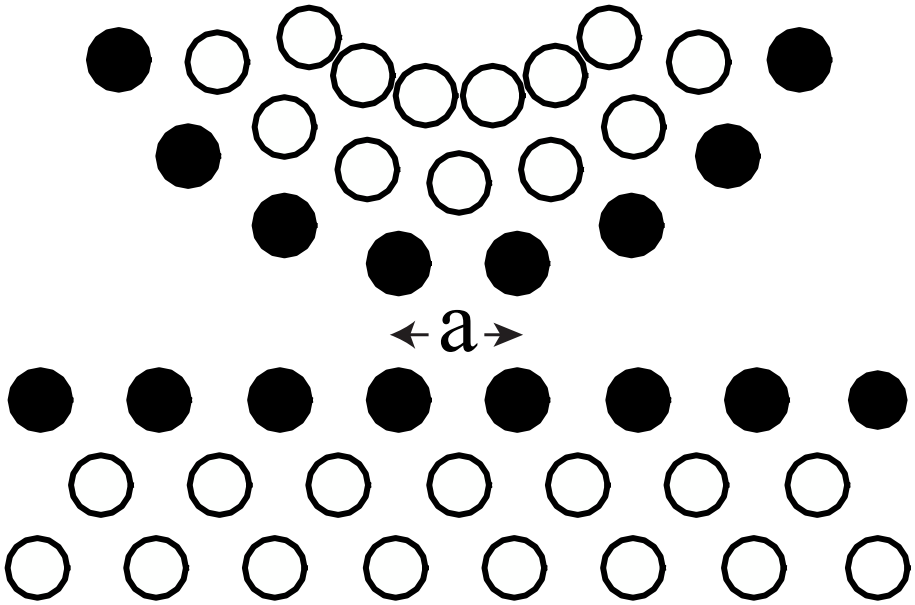

Figure 2.2: Close up side views of the wall geometry for planar (bottom) and cylindrical (top) simulations with the nearest-neighbor direction aligned with flow. Circles show lattice sites and closed circles indicate atoms on the surface closest to the fluid. Surface atoms are separated by a and successive layers are separated by $a/\sqrt{2}$. The spacing between subsurface atoms changes with radius for curved surfaces.

grow with a wide range of axis orientations and this is known to play an important role in determining their properties, such as conductivity.[143–147]

The nominal position of the wall surface is defined by the first layer of wall atoms, such that the surface radius R_w equals the radial coordinate of surface atoms. The surface curvature κ is defined as $\kappa = 1/R_{wi}$ for the inner wall and $\kappa = -1/R_{wo}$ for the outer one, where R_{wi} and R_{wo} denote the surface radii of the inner and the outer walls, respectively. In this study, for walls aligned with the (110) direction along the cylinder axis the inner and outer cylinder radii are 3.85σ and 23.0σ or 7.67σ and $26.83\ \sigma$. For walls aligned with the (100) direction along the axis, the radii are 4.09σ and 21.69σ or 8.14σ and 25.75σ.

The procedure used to generate the curved walls may produce very small or large separations between atoms in the layers away from the fluid. These might lead to plastic rearrangements in experimental systems. However, the structure of these inner layers has very little effect on the flow boundary condition. Simulations without the third layer gave indistinguishable results for the slip length. The main effect of the second layer is to prevent fluid atoms from penetrating between atoms of the outer solid layer.[22] As shown in Sec. 2.4 only the response to the periodic potential from the outer layer is needed to explain the detailed trends in slip length. This is why results for very short range interactions where fluid atoms only feel the outer layer ($r_c = 2^{1/6}\sigma$) show the same trends as simulations with larger r_c. It also explains why our results are very similar to those of Chen and Koplik,[32] who used a very different

crystalline structure under the outer solid layer.

Figure 2.3 shows the time-averaged fluid density profile as a function of distance from the wall for flat surfaces with $a = 1.2\sigma$ and 0.75σ. In the near wall region, the distribution of fluid atoms becomes non-isotropic and layering emerges in the density profile.[22,25,95,148–157] The first peak corresponds to the preferred spacing between wall and fluid atoms. The density profile then oscillates with peaks separated by one fluid atom diameter, and gradually relaxes to a uniform bulk density after a few oscillations. Near a wall surface, layers can be associated with each density peak and the boundaries between layers with local density minima. Trends in layering with wall geometry and interactions are discussed in Sec. 2.3.2.

Layering is less related to the slip length than the degree of lateral structure within the first layer of fluid.[22,26,27,30,31,35,155,158–160] To describe the in-layer structure, the 2D static structure factor, $S_1(\vec{q})$, is calculated as a function of wave vector $\vec{q}$ for the first layer of fluid atoms.

For the flat surface, $S_1(\vec{q})$ is evaluated according to

$$S_1(\vec{q}) = S_1(q_x, q_y) = |\sum_j \exp[i(q_x x_j + q_y y_j)]|^2 / N_1, \tag{2.3}$$

where x_j and y_j are the two-dimensional (2D) coordinates of atom j and N_1 is the number of fluid atoms in the first layer. The allowed wave vectors are determined by the periods of the system in the x-y plane, $\vec{q} = (2\pi h/L_x, 2\pi k/L_y)$ where h and k are integers. The periodic potential of the wall produces sharp peaks in $S_1(\vec{q})$ at the

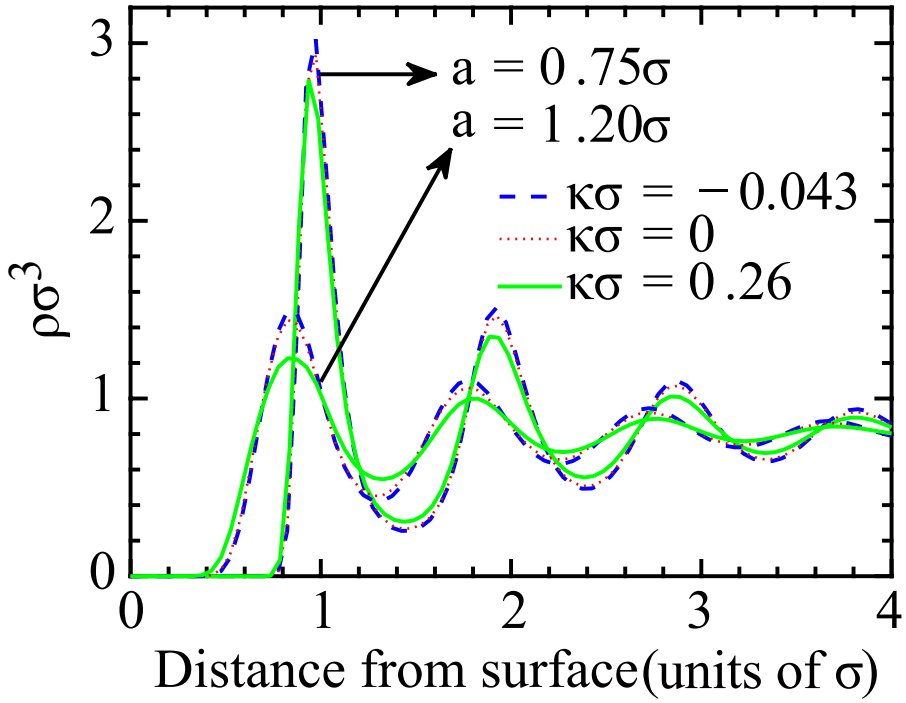

Figure 2.3: Fluid density as a function of distance from wall surface for lattice spacing $a = 1.20\sigma$ and 0.75σ at the indicated curvatures. Surfaces have wall-fluid interaction strength $\epsilon_{wf} = 0.4\epsilon$, $\sigma_{wf} = 1\sigma$, and the density is averaged over $10^4\tau$. The oscillations reflect layering and the layer boundaries are typically associated with the density minima. Here the (110) direction is along the cylinder axis but similar results are found for the (100) orientation.

corresponding reciprocal lattice vectors $\vec{G}_{m,n}$ of the wall. For the fcc (100) surface with nearest neighbors along x and y, $\vec{G}_{m,n} = (2\pi m/a, 2\pi n/a)$.

The squared relative amplitude of the areal density modulation $n_1(\vec{G})$ produced at each $\vec{G}$ is

$$|n_1(\vec{G})/\bar{n}_1|^2 = \tilde{S}_1(\vec{G})/N_1 \tag{2.4}$$

where $\bar{n}_1 = N_1/A_1$ is the number of particles per area in the first layer. This response to the substrate potential is independent of system size while the intrinsic diffusive background $S_{1,eq}(\vec{q})/N_1$ decreases linearly with system size. We increase the system size until the diffusive background is small and then subtract it from the total signal. The induced peaks are confined to only one of the wave vectors allowed by periodic boundary conditions, and the background is obtained by averaging over the four closest allowed $\vec{q}$.

For the cylindrical surface, we approximate the first fluid layer by a 2D cylindrical sheet located at the radius corresponding to the first peak in the fluid density. As noted below this radius is associated with the flow boundary condition and is denoted R_{bc}. The polar coordinates of each atom in the first layer $(r\theta, y)$ are mapped to 2D coordinates on a sheet (x, y) with $x = R_{bc}\theta$.[30,31] Then the lateral structure factor is evaluated with respect to the 2D coordinates. The main difference from the planar case is that the period L_x is replaced by the circumference of the layer, $2\pi R_{bc}$, in determining the allowed wavevectors.

The structure factors shown below are obtained for equilibrium systems. They are

nearly the same in sheared systems because the shear rates are kept in the limit of linear response. Structure factors are typically evaluated every 0.05τ and temporally averaged over up to 500τ.

2.2.5 Calculating the Slip Length

2.2.5.1 Planar Couette flow

For stationary Newtonian fluid flow past an impenetrable solid surface, Navier's slip model assumes that the friction force per unit area between the fluid and the solid surface is proportional to the slip velocity Δu_t, i.e., the relative velocity of fluid and solid. This force is balanced by the viscous shear stress Π_{nt} of the fluid at the surface,

$$\beta \Delta u_t = \Pi_{nt}, \tag{2.5}$$

where β is the drag coefficient between the fluid and the solid surface, and n and t represent the normal and tangential directions to the surface, respectively. Newton's law for the bulk fluid relates the shear stress to the strain rate $\partial u_t / \partial n$:

$$\Pi_{nt} = \mu \frac{\partial u_t}{\partial n}. \tag{2.6}$$

where μ denotes the fluid viscosity. Combining these equations one arrives at Navier's slip boundary condition,

$$\Delta u_t = \frac{\mu}{\beta} \frac{\partial u_t}{\partial n} = L_s \frac{\partial u_t}{\partial n} \tag{2.7}$$

where the slip length $L_s \equiv \mu / \beta$ quantifies the degree of slip at the surface.

For planar Couette flow, the viscous stress Π_{xz} is constant throughout the channel, and the incompressible Navier-Stokes equations reduce to $\mu\partial^2 u_x/\partial z^2 = \partial\Pi_{xz}/\partial z = 0$. Solving this equation, one arrives at a linear velocity profile,

$$u_x = A_1 z + A_2. \tag{2.8}$$

The two constants, A_1 and A_2, are determined by the boundary conditions at the wall-fluid interfaces.

Mean velocity profiles from two very different lattice constants are presented in Figure 2.4(a). Both profiles exhibit the expected linear velocity profile [Eq. (2.8)] in the central region of the fluid. Deviations begin to become apparent within one or two atomic diameters of the wall due to the layering and in-plane structure discussed above.[22] At the top wall there is a strong interaction that causes the fluid velocity to saturate to the wall velocity inside the fluid. This is called a stick boundary condition and is kept the same for all runs. The behavior near the stationary bottom wall is very sensitive to wall density. For the sparse surface case ($a = 1.2\sigma$) the velocity approaches zero, but for the closely packed surface there is a substantial velocity difference at the wall, i.e. slip.

The definition of the slip length in Eq. (2.7) requires both the strain rate and slip velocity. For Couette flow the strain rate is uniform in the central region and given by the coefficient A_1 in Eq. (2.8). The value of slip velocity is more ambiguous. Since the goal is to determine boundary conditions for the continuum equations, the slip

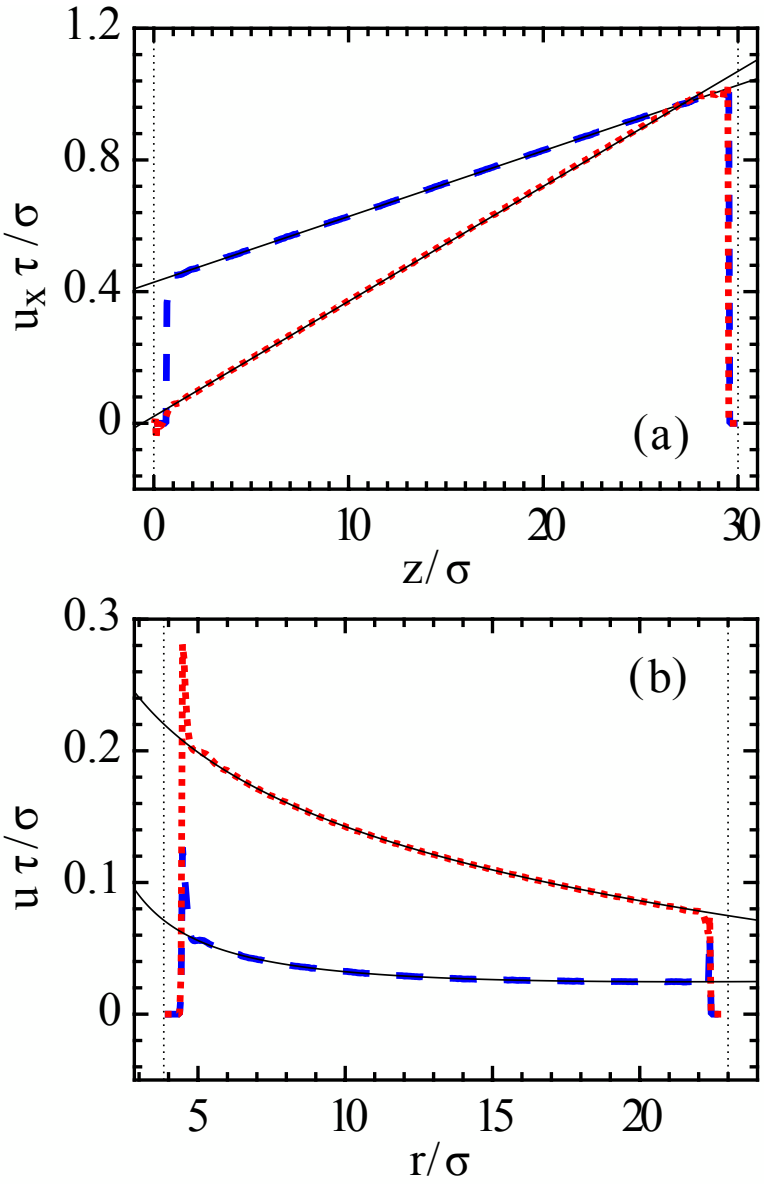

Figure 2.4: Velocity profiles for (a) planar Couette flow at $a = 0.75\sigma$ (dashed blue) and 1.2σ (dotted red), and (b) angular (dashed blue) and axial (dotted red) flow in the cylindrical geometry at $a = 0.75\sigma$. Thin solid black lines show fits to continuum theory and dotted vertical lines show the positions of wall surface atoms. Flows are along the (110) orientation with $\epsilon_{wf} = 0.1\epsilon$.

velocity is evaluated from the extrapolation of the continuum solution rather than the actual velocity profile.[134] The answer still depends on the location of the wall which is uncertain up to lengths of order σ. We choose the height d_1 where the density peak associated with the first fluid layer is located (Fig. 2.3) as the hydrodynamic boundary. The slip velocity Δu_t then corresponds to the velocity difference between the first fluid layer and the solid wall. This is the natural quantity for Eq. (2.5) and the calculation of frictional drag discussed below. For the planar Couette case any other choice (e.g., in Refs. [22, 27, 161, 162]) gives a constant shift in the slip length and other common choices of the reference plane differ by less than the layer spacing.

For the planar flow simulations, the velocity profiles are averaged within horizontal bins of thickness $\Delta z = 0.05\sigma$ for a time period of $10^4\tau$ at steady state. The resulting flow profile is fit to Eq. (2.8) over the region more than 3σ from either surface. We verified that changing this condition by $\pm\sigma$ does not produce any noticeable changes. The slip length is then obtained from the fit coefficients as

$$L_s = d_1 + A_2/A_1 \tag{2.9}$$

The fit results are further averaged over five independent realizations of the system to quantify statistical errors and remove any long-time correlations.

2.2.5.2 Cylindrical Couette Flow

For the case of angular flow between rotating cylinders, the viscous shear stress at the curved cylindrical surface is given by

$$\Pi_{n\theta} = \mu \left(\frac{\partial u_\theta}{\partial n} - \kappa u_\theta \right) \tag{2.10}$$

where κ denotes the local curvature of the surface. For the convex inner surface in Figure 2.1, $\kappa > 0$, and for the concave outer surface, $\kappa < 0$. Plugging Eq. (2.10) into the force balance condition, Eq. (2.5), one arrives at the slip boundary condition for a curved surface,[28,29]

$$\Delta u_\theta = \frac{\mu}{\beta} \left(\frac{\partial u_\theta}{\partial n} - \kappa u_\theta \right) = L_s \left(\frac{\partial u_\theta}{\partial n} - \kappa u_\theta \right). \tag{2.11}$$

In terms of the local angular velocity, $\omega = u_\theta / r$, Eq. (2.11) can be rewritten into a form similar to Eq. (2.7):[32]

$$\Delta \omega = L_s \frac{\partial \omega}{\partial n}. \tag{2.12}$$

Therefore the slip length along the direction of curvature can be interpreted as the distance inside the wall to which the fluid angular velocity is linearly extrapolated to reach the angular velocity of the wall surface.

For bulk flow between two rotating concentric cylinders, the incompressible Navier-Stokes equations reduce to

$$\frac{dp}{dr} = \rho \frac{{u_\theta}^2}{r}, \tag{2.13}$$

$$\frac{d}{dr}\left(\frac{1}{r}\frac{d}{dr}(ru_\theta)\right) = 0, \tag{2.14}$$

where the pressure p and the tangential velocity u_θ are functions only of the radial coordinate r and there is no flow along the cylinder axis. The general solution of the velocity profile is given by

$$u_\theta(r) = B_1 r + B_2/r, \tag{2.15}$$

where the constants B_1 and B_2 are determined by the boundary conditions.

In simulations, the angular flow is generated by rotating the inner wall at a rotation rate U_w/R_{wi}, where U_w is the speed of the surface atoms (closest to the fluid). For the cylindrical simulations, the velocity is averaged within cylindrical slabs of thickness $\Delta r = 0.05\sigma$ every $5 \times 10^3\tau$ over a simulation time of $10^5\tau$. The slip length is then calculated for each average velocity profile, and further averaged over 20 consecutive time intervals.

Figure 2.4(b) shows that the mean flow profiles from MD simulations are well fitted by the continuum solution except for regions within a few sigma of the walls [Eq. (2.15)]. As found in past work, the viscosity of the fluid may be modified in the layers closest to the walls.[22,156,163] The sharp peak shown in Fig. 2.4 (b) near the inner wall comes from a very low density of atoms that are so close to the wall that their velocity is close to that of the wall. They make up a very small fraction of the first density peak. This effect is not visible near stationary walls because the density and wall velocity are both going to zero.

To measure the slip length from the MD velocity profiles, we rewrite Eq. (2.15) as

$$ru_\theta(r) = B_1 r^2 + B_2, \tag{2.16}$$

and fit the simulation data by this parabolic function. Combining Eq. (2.15) and Eq. (2.11), plugging in the fitted parameters B_1 and B_2, and solving for L_s, the slip length of the inner wall is given by

$$L_s = -\left(B_1 R_{bc} + \frac{B_2}{R_{bc}} - U_{bc}\right)\frac{{R_{bc}}^2}{2B_2}, \tag{2.17}$$

where $R_{bc} = R_{wi} + d_1$ denotes the position of the hydrodynamic boundary, and $U_{bc} = U_w(1 + d_1/R_{wi})$ designates the fluid velocity at the effective hydrodynamic boundary R_{bc}. For the outer surface,

$$L_s = \left(B_1 R_{bc} + \frac{B_2}{R_{bc}} - U_{bc}\right)\frac{{R_{bc}}^2}{2B_2}, \tag{2.18}$$

where $R_{bc} = R_{wo} - d_1$, and $U_{bc} = 0$ since the outer wall is held at rest.

As for the planar case, the wall position is defined at the center of the first density peak in the above analysis. For the cylindrical geometry, changing this definition does not produce a constant shift in the slip length because the flow is nonlinear. Shifting the reference plane to the midpoint between wall and first fluid layer[30–32] can reduce L_s by up to $\sim 4\sigma$ for the smallest radii and largest slip lengths but the trends with curvature remain the same. The definition used here is most natural for the theory described in Sec. 2.4 which relates the friction between the first fluid layer

and substrate to structure in the first layer.

2.2.5.3 Axial Flow in Cylindrical Geometry

For the axial flow case, the viscous shear stress at the cylindrical surface is $\Pi_{ny} = \mu\partial u_y/\partial n$ and thus the slip boundary condition has the same form as Eq. (2.7), $\Delta u_y = L_s(\partial u_y)/\partial n$. The Navier-Stokes equations for the bulk flow reduce to

$$\frac{\mu}{r}\frac{d}{dr}\left(r\frac{du_y}{dr}\right) = \frac{dp}{dy} = 0, \tag{2.19}$$

and the velocity profile is given by

$$u_y(r) = C_1 \ln(r) + C_2. \tag{2.20}$$

In simulations, the axial flow is produced by moving the inner cylinder along the y direction at a speed U_w. To measure the slip length, Eq. (2.20) is fitted to the mean velocity profile (as illustrated in Figure 2.4(b)), and the slip length along the axial direction is calculated by

$$L_s = (C_1 \ln(R_{bc}) + C_2 - U_w)\frac{R_{bc}}{C_1}, \tag{2.21}$$

$$\text{and } L_s = -(C_1 \ln(R_{bc}) + C_2)\frac{R_{bc}}{C_1}, \tag{2.22}$$

for the inner and the outer wall, respectively.

2.3 Results

2.3.1 Slip Length

Calculated slip lengths are tabulated in Appendix B for all the flow geometries and surface properties included in this study. For each case we verified that the results are in the low strain rate limit by varying the strain rate by at least a factor of 2. The quoted values were evaluated for planar flows with top wall speed $U_w = 1.0\sigma/\tau$, for cylindrical angular flows with inner wall speed $U_w = 0.2\sigma/\tau$, and for cylindrical axial flows with inner wall speed $U_w = 0.6\sigma/\tau$. In all cases the maximum strain rate is less than $0.071/\tau$, which Chen *et al.*[32] also find is in the linear response limit.

In Figure 2.5(a), the value of the slip length is plotted against the surface curvature for cylindrical Couette flow with different surface lattice spacings. Here $\epsilon_{wf} = 0.1\epsilon$, $\sigma_{wf} = 1\sigma$ and flow is along the (110) direction between nearest neighbors of the fcc surface. For this rotational flow case, three typical patterns are clearly observed. For the highly packed surfaces, $a = 0.75\sigma$ or 0.86σ, the slip length L_s decreases by up to a factor of 5 as curvature increases. The opposite trend is observed for sparse surfaces, $a = 1.20\sigma$ or 1.09σ, where L_s increases slightly ($\sim 30\%$). Nonmonotonic behavior is found for $a = 1.00\sigma$: L_s drops as $\kappa\sigma$ increases from -0.043 to 0.13 and then rises as $\kappa\sigma$ further increases from 0.13 to 0.25, These trends with curvature are determined by surface density and are not affected by changing the wall-fluid LJ interaction, although the absolute slip lengths are affected. Note that Chen *et al.*[32] considered

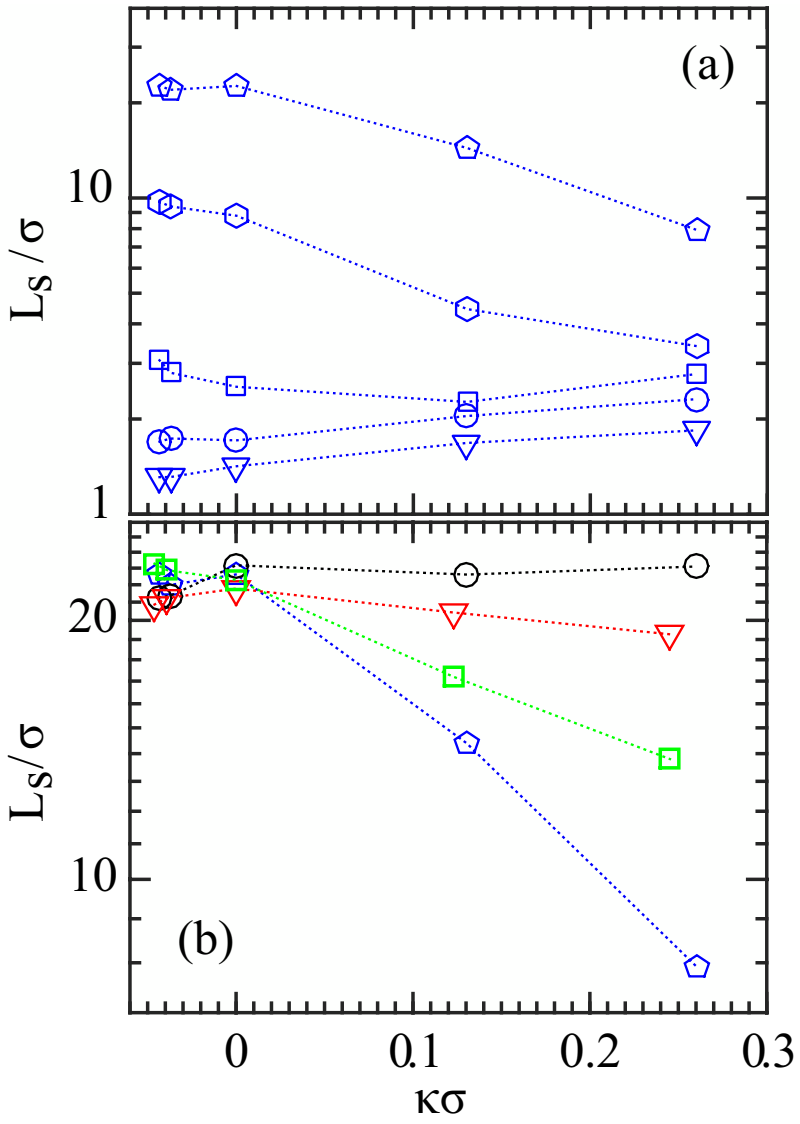

Figure 2.5: Slip length L_s as a function of surface curvature κ for $\epsilon_{wf} = 0.1\epsilon$. (a) L_s for cylindrical Couette flows along (110) direction with different lattice spacing: $a = 1.2\sigma$ (triangles), 1.09σ (circles), 1.00σ (squares), 0.86σ (hexagons) and 0.75σ (pentagons). (b) L_s with $a = 0.75\sigma$ for cylindrical Couette flows along (110) (blue pentagons) and (100) direction (red triangles), and axial cylindrical flows along (110) (black circles) and (100) direction (green squares). Dotted lines are guides to the eye.

$a = 1.09\sigma$ and positive curvatures. We also find little change in L_s for this special case.

The changes in slip length with curvature are very dependent on surface orientation as shown in Figure 2.5(b). For the nearest-neighbor (110) orientation, the slip length for rotational flow shows the large changes illustrated in Figure 2.5(a) while there is very little ($\sim$ 10%) change in the slip length for axial flow. In contrast, for the (100) orientation, curvature affects axial flow more strongly than rotational flow. Both follow the trend with curvature for rotational (110) flow but change more gradually. Note that for flat surfaces L_s is the same for flow along (100) and (110) even though the directions are not crystallographically equivalent.

The different patterns of behavior of slip length for different flow directions, atomic spacings and lattice orientations can only be understood from the microscopic perspective. We first consider how curvature affects the structure of the fluid and then present a quantitative theory for the variations in slip length.

2.3.2 Fluid Structure

The correlation between the atomic spacing on flat surfaces and the degree of fluid layering has been discussed in Refs. [22, 25]. As illustrated in Figure 2.3, denser surfaces (smaller a) lead to sharper density peaks. One reason is that a higher density increases the number of wall atoms that interact with a given fluid atom and thus deepens the potential energy minimum at the first layer. Increasing the density also reduces the ability of fluid atoms to penetrate in between wall atoms. Figures

2.6(a) and 2.6(b) illustrate the lateral variation of constant energy surfaces above flat and curved walls, respectively. As wall atoms move closer, the depth of local minima decreases rapidly. The decrease in the corrugation of the equipotential surface reduces fluctuations in the preferred height of fluid atoms and thus sharpens the first density peak.

Figure 2.3 provides information about how curvature affects layering. For all cases considered we found a monotonic increase in layering as the curvature went from positive to negative. The effect is particularly noticeable for large $\kappa\sigma$ where the radius of curvature approaches atomic scales. Figure 2.6(c) provides insight in to the origin of this trend. While the spacing between wall atoms remains fixed, the first fluid layer forms at a different radius. Since the number of atoms is fixed, the spacing between potential minima scales as the radius of the fluid layer divided by that of the wall layer. This produces an effective decrease in the wall density with increasing $\kappa\sigma$. As for flat surfaces, the decrease in wall density leads to a broader and lower density peak.

Past work shows that the degree of slip correlates more strongly with lateral structure than fluid layering or wetting.[22,26,27,30,31,35,155,158–160,164,165] Even featureless walls that are perfectly wetting produce strong layering peaks, but they provide a translationally invariant surface that cannot transmit friction. The drag coefficient β only depends on the variation in surface potential that is related to lateral corrugation (Figure 2.6). As noted in Sec. 2.2.3 this lateral corrugation produces in-plane density

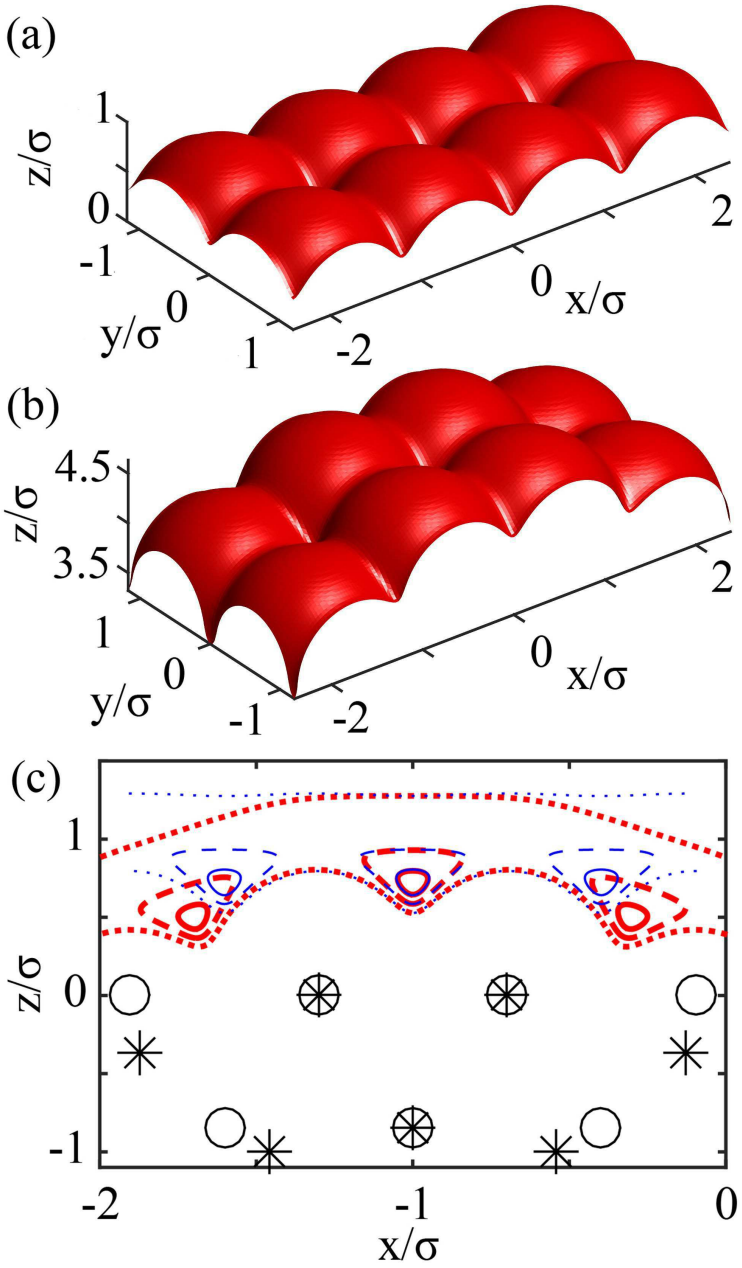

Figure 2.6: Equipotential surfaces at $V_{wall} = 1.1\epsilon$ for (a) planar wall and (b) cylindrical wall with positive curvature and radius $R_w = 3.84\sigma$. (c) Potential contours over the xz-plane at $y = 0$ for the same flat (thin blue) and cylindrical (thick red) surfaces presented in (a) and (b). Different line patterns correspond to different energy contours: $V_{wall} = -0.4\epsilon$ (solid), -0.3ϵ (dashed) and -0.1ϵ (dotted). The black circles and asterisks mark atomic positions of the flat and the cylindrical wall, respectively. The z coordinate is shifted so the topmost atoms of cylindrical and flat surfaces coincide. Here $\epsilon_{wf} = 0.1\epsilon$ and $a = 1.20\sigma$.

modulations $n_1(\vec{G})$ [Eq. (2.4)] at the reciprocal lattice vectors $\vec{G}$ that characterize the periodicity of the substrate. The squared relative amplitude $|n_1(\vec{G})/\bar{n}_1|^2 = \tilde{S}_1(\vec{G})/N_1$.

Figures 2.7(a) and 2.7(b) show $S_1(\vec{q})/N_1$ for flat walls with high and low density. Only positive q_x and q_y are shown since the structure factor has the 4-fold symmetry of the wall. The weak circular ridges at a wave vector $|\vec{q}_f| \approx 2\pi/\sigma$ reflect the intrinsic short range order within a fluid. They are insensitive to wall density but decrease with system size as $1/N_1$ since $S_1(\vec{q}_f)$ is constant. There are also sharp peaks at the reciprocal lattice vectors characterizing the periodicity of the substrate. These Bragg peaks represent the response of the fluid to the surface corrugation and are independent of system size.[22,33,34]

Previous studies of flat surfaces found that β increased with the in-layer response to the substrate potential at reciprocal lattice vectors.[22,33,34,164] For flat surfaces the largest response is at the shortest reciprocal lattice vectors, $\vec{G}_{\pm1,0}$ and $\vec{G}_{0,\pm1}$. As noted above, a denser surface tends to have a weaker corrugation and thus smaller values of $S_1(\vec{G})/N_1$. In Figures 2.7(a) and 2.7(b) the peaks for $a = 1.2\sigma$ are about 40 times larger than those for $a = 0.75\sigma$. Larger systems had to be used for $a = 0.75\sigma$ to reduce the circular ridge from the diffuse background below the Bragg peaks.

Figures 2.7(c) and 2.7(d) show $S_1(\vec{q})/N_1$ for the same atomic spacings but with curvature $\kappa\sigma = 0.26$. Here the cylinder axis is along the (110) direction and the curvature breaks the symmetry between x and y directions. The peaks along the axis of the cylinder change relatively little ($\sim 10\%$) from the values for flat surfaces, but

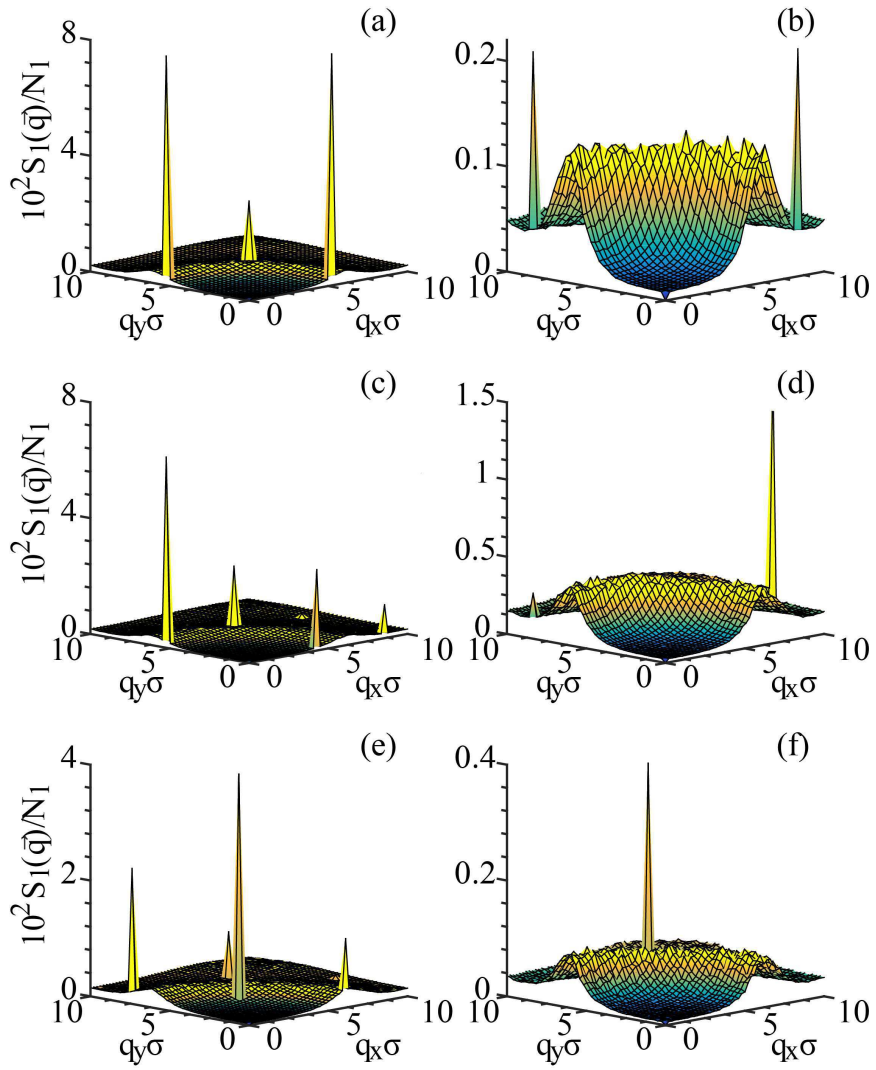

Figure 2.7: In-plane order as characterized by normalized structure factor $S_1(\vec{q})/N_1$ for two lattice spacings, $a = 1.20\sigma$ [(a),(c), and (e)] and 0.75σ [(b),(f),and (d)], with $\epsilon_{wf} = 0.1\epsilon$. Panels (a) and (b) show results for flat walls with x axes along (110). Panels (c) and (d) show results for cylindrical walls with $\kappa\sigma = 0.26$ and axes along (110) direction. Panels (e) and (f) show results for cylindrical walls with $\kappa\sigma = 0.24$ and axes along the (100) direction.

the peaks along the direction of curvature change dramatically. From our previous arguments we expect the curvature to produce a larger effective spacing and thus a larger Bragg peak. This is consistent with the order of magnitude increase in the peak height for the dense surface, $a = 0.75\sigma$. However the Bragg peak for the sparse surface, $a = 1.2\sigma$, is smaller by about a factor of 3. The reason is that the relative spacing of fluid and wall atoms is also important. The fluid can respond more to the potential when the Bragg peak is close to the circular ridge. Curvature moves the peak away from the ridge for $a = 1.2\sigma$ and towards the ridge for $a = 0.75\sigma$.

In the following we focus on the wall induced portion of the Bragg peaks, $\tilde{S}_1(\vec{G})$. We verified that increasing the system size reduced the background from the circular ridge and did not affect the value of $\tilde{S}_1(\vec{G})$ obtained by subtracting this background. The calculated values of $\tilde{S}_1(\vec{G})/N_1$ at the smallest reciprocal lattice vectors are also tabulated in Appendix B for all the flow geometries and surface properties included in this study.

The variation of $\tilde{S}_1(\vec{G}_{1,0})/N_1$ with surface curvature κ is manifested in Figure 2.8 for (110) flow at different surface lattice spacings a. Note that the trends with curvature in $\tilde{S}_1(\vec{G}_{1,0})/N_1$ are exactly opposite to the trends in L_s shown in Figure 2.5(a). For dense surfaces the Bragg peak rises by an order of magnitude as curvature increases and the effective corrugation increases. For the sparse surfaces, the Bragg peak decreases monotonically because the associated wave vector is moving away from the circular ridge associated with the intrinsic spacing between fluid atoms. For the

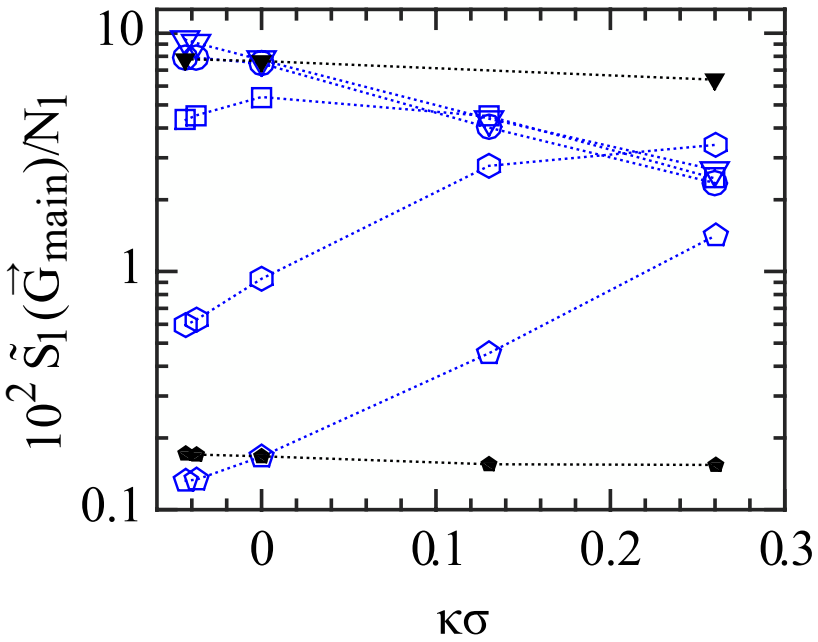

Figure 2.8: Variation of $\tilde{S}_1(\vec{G}_{1,0})/N_1$ (open blue) and $\tilde{S}_1(\vec{G}_{0,1})/N_1$ (closed black) with surface curvature for the same surfaces shown in Fig. 2.5(a), i.e., $\epsilon_{wf} = 0.1\epsilon$ and lattice spacing $a = 1.2\sigma$ (triangles), 1.09σ (circles), 1.00σ (squares), 0.86σ (hexagons) and 0.75σ (pentagons). Dotted lines are guides to the eye.

intermediate wall density the two effects compete and the peak height has a maximum at intermediate curvature.

The fundamental cause of these variations is the change in the effective spacing a_{eff} between potential energy minima divided by the intrinsic spacing between fluid atoms. The spacing between fluid atoms scales as $\bar{n}_1^{-1/2}$ where $\bar{n}_1$ changes by of order 10% with interaction strength and other parameters. The effect of curvature on a_{eff} depends on orientation. For the (110) orientation the axial spacing is not affected while the spacing around the circumference scales as $a_{eff} = aR_{bc}/R_w = a(1 + \kappa d_1)$.

Figure 2.9(a) presents a clear picture of how the Bragg peak height varies against $a_{eff}\bar{n}_1^{1/2}$ for the full range of wall densities studied. Similar results are obtained for other wall/fluid interaction strengths. The largest response is obtained for $a_{eff}\bar{n}_1^{1/2}$ around 0.8 to 0.9, where the Bragg peak is near the center of the circular ridge. The peak height falls off as a_{eff} increases or decreases because the peak position moves away from the intrinsic fluid spacing. The decrease in corrugation with decreasing a_{eff} produces a very asymmetric curve that drops much more rapidly as a_{eff} decreases. Note that curvature does not change a_{eff} along the cylindrical axis for the (110) orientation and we observe little ($< 10\%$) change in $\tilde{S}_1(\vec{G}_{0,1})/N_1$ with κ. Figure 2.9(b) replots the data from Figure 2.5(a) as a function of a_{eff}. Note that the trends in L_s are exactly opposite to those in $\tilde{S}_1(\vec{G})/N_1$. Stronger order induced by the solid leads to less slip.

The effect of curvature on $\tilde{S}_1(\vec{G})/N_1$ differs considerably for the (100) orientation

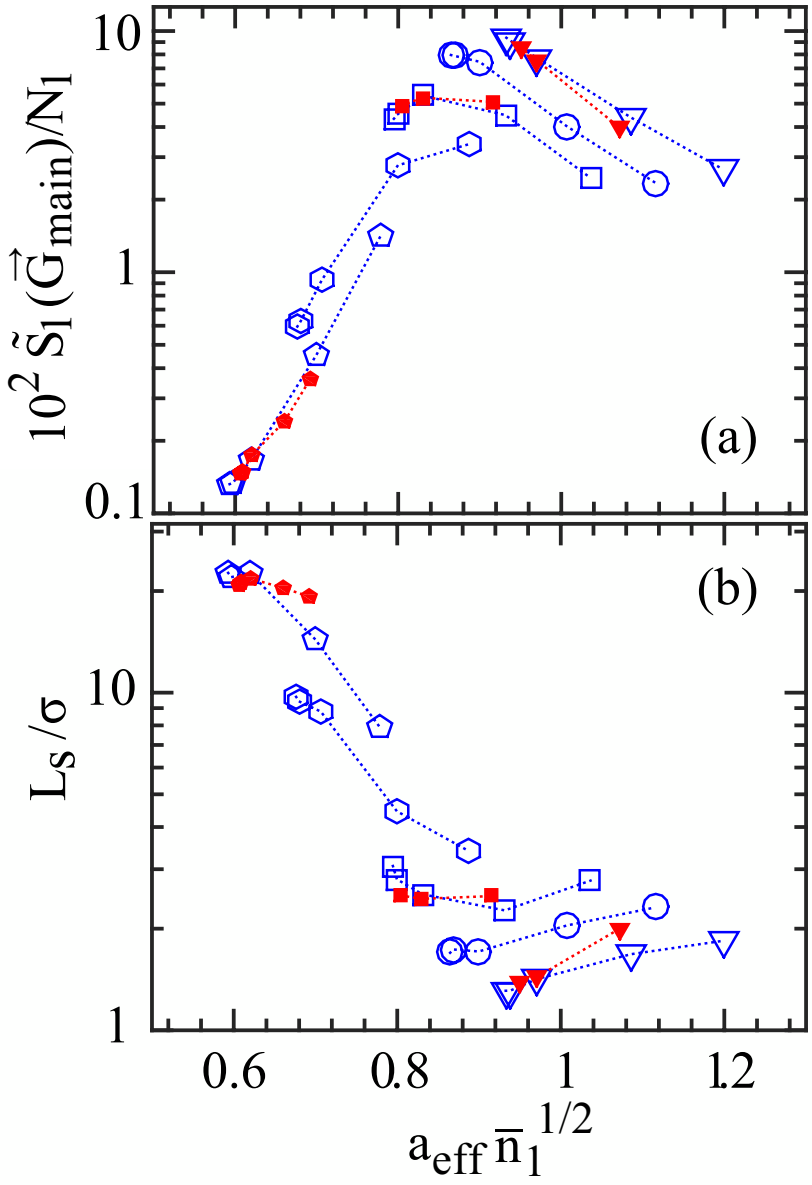

Figure 2.9: (a) Variation of $\tilde{S}_1(\vec{G})/N_1$ at $\vec{G}_{1,0}$ for y-axis (110) orientation (open blue) and at the smallest $\vec{G}$ for y-axis along (100) orientation (closed red) as a function of the relative effective spacing $a_{eff}\bar{n}_1^{1/2}$, i.e., the effective spacing of minima in the wall potential energy a_{eff} normalized by the mean spacing of atoms in the first layer $\bar{n}_1^{-1/2}$. The symbols indicate lattice spacing $a = 1.2\sigma$ (triangles), 1.09σ (circles), 1.00σ (squares), 0.86σ (hexagons) and 0.75σ (pentagons). (b). Variation of L_s as a function of effective spacing for cylindrical Couette flow and for the same surfaces in (a). Dotted lines are guides to the eye and $\epsilon_{wf} = 0.1\epsilon$.

where flow is along the next-nearest neighbor direction. Curvature now rotates the angle θ between the cylinder axis and the nearest potential energy minima as well as changing the distance. Accounting for the change in spacing around the circumference we find:

$$a_{eff} = a(1 + \kappa d_1 + \kappa^2 d_1^2)^{1/2} \sim a(1 + \kappa d_1/2) \quad (2.23)$$

$$\tan(\theta) = 1/(1 + \kappa d_1) \sim 1 - \kappa d_1 \quad . \quad (2.24)$$

Figures 2.7(e) and 2.7(f) show $S_1(\vec{q})/N_1$ for the same curvature as Figures 2.7(c) and 2.7(d) but with this new orientation. As expected, the smaller change in a_{eff} leads to smaller changes in the Bragg peak heights. This is also consistent with the smaller change in L_s with curvature for this wall orientation. Note that the reciprocal lattice vectors rotate in the opposite direction from the vector to adjacent potential energy minima and thus towards the cylinder axis. As we now discuss, this change in direction explains why curvature affects axial flow more strongly than rotational flow for the (100) direction.

2.3.3 Relating Slip Length to Structure

In this section, we describe a microscopic theory that provides a quantitative relationship between the slip length, curvature and fluid structure, and thus gives a deeper insight into the mechanism of the wall-fluid coupling. By definition, the slip length L_s is the fluid viscosity divided by the interfacial drag coefficient. We have verified that for our simulations the viscosity can be treated as a constant parameter.

Thus, the slip length is only a function of the strength of the viscous friction at the wall-fluid interface, i.e., L_s is inversely proportional to the drag coefficient β.

The force between the wall and the first fluid layer dominates the drag force. It can be calculated using a model for the closely related problem of friction between an adsorbed monolayer and a solid substrate.[33,34,164,165] While the fluid layer slides over the substrate, the density modulation produced by the periodic substrate potential remains locked in phase with the substrate. The relative motion of the wall-induced modulation and the center of mass of the layer leads to dissipation and thus a viscous drag. The rate of energy dissipation is proportional to the energy stored in the modulation and to the decay rate of energy into other modes.[33,34] Equating this dissipation to the power per unit area dissipated by drag, $\beta\Delta u^2$, gives an expression for β and an associated time $\tau_{slip} = m\bar{n}_1/\beta$.

Smith *et al.*[34] present expressions for β in the limit of linear response where the modulation in areal number density at wave vector $\vec{q}$ and frequency ω, $n(\vec{q},\omega)$, is proportional to the substrate potential $U(\vec{q},\omega)$:

$$n_1(\vec{q},\omega) = -\alpha(\vec{q},\omega)U(\vec{q},\omega) \tag{2.25}$$

where $\alpha(\vec{q},\omega)$ represents a linear susceptibility to the substrate potential. Their Eq. (10) gives

$$\beta = \sum_{\vec{G}} |U(\vec{G})|^2 |\hat{G}\cdot\Delta\hat{u}|^2 |\vec{G}|^2 \;\; \frac{\mathrm{Im}[\alpha(\vec{G},\vec{G}\cdot\Delta\vec{u})]}{\vec{G}\cdot\Delta\vec{u}}, \tag{2.26}$$

where $\vec{G}\cdot\Delta\vec{u}$ represents the oscillation frequency produced by relative motion at slip

velocity $\Delta\vec{u}$ and the last term on the right-hand side becomes independent of $\Delta\vec{u}$ as $\Delta\vec{u}$ goes to zero. $\hat{G}$ and $\Delta\hat{u}$ are unit vectors along $\vec{G}$ and $\Delta\vec{u}$, respectively. Note that β scales as the square of the Fourier components of the substrate potential. The authors of Refs. [33, 34] tested this scaling over 3 orders of magnitude in β.

One of the complexities associated with using Eq. (2.26) is that the substrate potential depends upon height. One can calculate the Fourier transform averaged over the density profile in the first layer or one can use the Bragg peaks in the structure factor to measure the effective potential. Using the general relation

$$\frac{\tilde{S}_1(\vec{G})}{N_1} = \left|\frac{n_1(\vec{G},0)}{\bar{n}_1}\right|^2 = \left|\frac{\alpha(\vec{G},0)}{\bar{n}_1}\right|^2 |U(\vec{G})|^2, \tag{2.27}$$

one can rewrite the drag coefficient as

$$\beta = m\bar{n}_1 \sum_{\vec{G}} |\hat{G}\cdot\Delta\hat{u}|^2 \frac{\tilde{S}_1(\vec{G})}{N_1} \frac{1}{t_{ph}(\vec{G})}, \tag{2.28}$$

where

$$t_{ph}(\vec{G}) \equiv \lim_{\omega\to 0} \frac{m}{\bar{n}_1|\vec{G}|^2} \frac{\omega|\alpha(\vec{G},0)|^2}{\mathrm{Im}[\alpha(\vec{G},\omega)]}, \tag{2.29}$$

can be interpreted as the lifetime of acoustic phonons in the fluid layer,[34] and is inversely proportional to the rate at which the energy stored in this induced modulation is dissipated into other density waves. The first factor in the sum of Eq. (2.28) reflects the fact that only modulations with a component along the direction of flow $\Delta\hat{u}$ are affected by the motion and contribute to dissipation.

Equation (2.28) explains many of the trends found above, including the inverse

correlation between $S_1(\vec{G})$ and L_s seen in Figure 2.8 and in previous studies of flat surfaces.[22,26,27,155,158–160,166] In the case of flat surfaces the predicted slip length is independent of direction by symmetry (Table 2.2 in Appendix B). For example for flow along the (110) orientation two of the four reciprocal lattice vectors are along the flow and contribute to β while the others are perpendicular. For the (100) orientation, all four contribute to β but only half as much, since they are at 45 degrees to the flow. Curvature breaks this symmetry. For the (110) orientation, curvature only affects the magnitude of $\vec{G}$ and $\tilde{S}_1(\vec{G})$ along the rotation direction. This explains why rotational slip lengths change but axial do not. For the (100) orientation all four $\vec{G}$ change in magnitude and all have the same $\tilde{S}_1(\vec{G})$. Thus the axial and rotational slip lengths change in the same direction. The axial slip length is smaller because $\vec{G}$ rotates to be more along the axial direction [Eq. (2.24)].

In the cases considered in Refs. [33, 34], the phonon lifetime was nearly constant and the slip length scaled inversely with the sum over the smallest wave vectors of $\tilde{S}_1(\vec{G}_{main})/N_1$. Figure 2.10(a) shows there is a strong inverse correlation between slip length and $\tilde{S}_1(\vec{G})/N_1$ for all curvatures and orientations considered. However there is a significant spread that must reflect a variation in t_{ph}.

Figure 2.10(b) shows the value of the phonon lifetime calculated from Eq. (2.28) as a function of the ratio between minima spacing and fluid atom spacing, $a_{eff}\bar{n}_1^{1/2}$. All the data collapse onto a universal curve that represents the intrinsic response of the fluid layer. This represents a very compelling confirmation of Eq. (2.28).

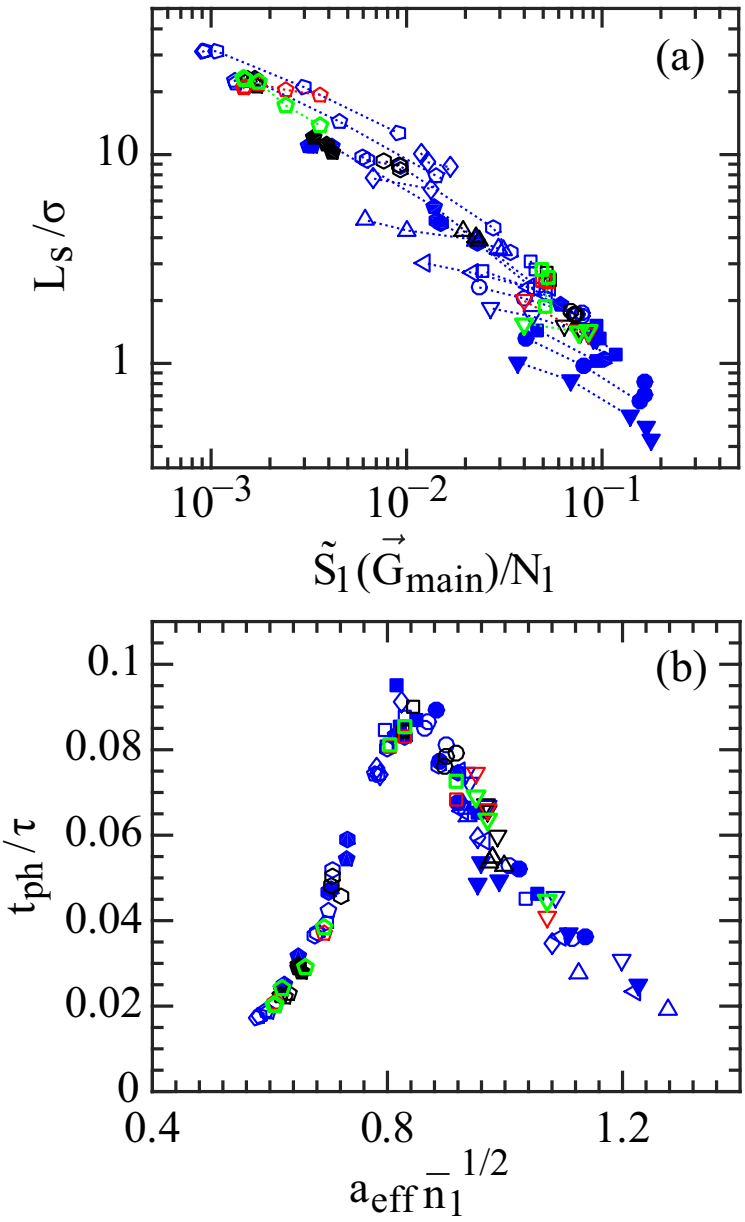

Figure 2.10: (a) Variation of slip length L_s as a function of the first peak in the structure factor $\tilde{S}_1(\vec{G}_{main})/N_1$ for cylindrical Couette flows along (110) (blue) and (100) (red) directions, and axial cylindrical flows along (110) (black) and (100) (green) directions. Results are shown for lattice spacing $a = 1.2\sigma$ (triangles), 1.09σ (circles), 1.00σ (squares), 0.86σ (hexagons) and 0.75σ (pentagons) and different wall-fluid interactions from Table I: A (open), B (closed), C (right-side left triangle and pentagon) and D (diamond and right-side up triangle). Dotted lines are guides to the eye. (b) Variation of phonon lifetime t_{ph} from Eq. (2.28) with $\tilde{S}_1(\vec{G})$ integrated over the entire first layer as a function of the relative effective spacing $a_{eff}\bar{n}_1^{1/2}$.

We have attempted to calculate t_{ph} independently by measuring the susceptiblity to a sinusoidal potential. As discussed in Appendix A, the potential oscillated with time but was constant for heights below the first minimum in the density shown in Fig. 2.3. For $a = 1.0$ ($a_{eff}\bar{n}_1^{1/2} = 0.82$) we find $t_{ph}/\tau = 0.92$, which is in excellent agreement with the numerical results in Fig. 2.10(b). However, for $a_{eff}\bar{n}_1^{1/2} = 0.6$ and 1.0 the calculated values of t_{ph} are much larger than the numerical results, $t_{ph}/\tau = 0.62$ and 0.61, respectively. This deviation reflects the fact that Equations 2.25 to 2.28 assume that the density modulations in the first layer are independent of height. This assumption is reasonably accurate for $a_{eff} = 1.0$ but there are strong variations with height for larger and smaller a_{eff}.

Figure 2.11 shows the cosine Fourier transform $n(\vec{G})$ of the local area density as a function of height for flat surfaces of different a. A negative value corresponds to density peaks out of phase with the solid substrate so that fluid atoms lie in gaps between solid atoms. Positive values correspond to fluid atoms lying above solid atoms.

For $a = 1.00\sigma$ the order is similar to that in an fcc crystal with all atoms in the first fluid layer above gaps in the solid. Atoms in the second layer lie above gaps in the first layer and thus above solid atoms. For smaller and larger a the oscillations in in-plane order do not correspond with the peaks and troughs in the density versus height. The sign of $n(\vec{G})$ changes within the first layering peak in both cases. Indeed for $a = 0.75\sigma$ the sign change occurs near the density peak of the first layer. The

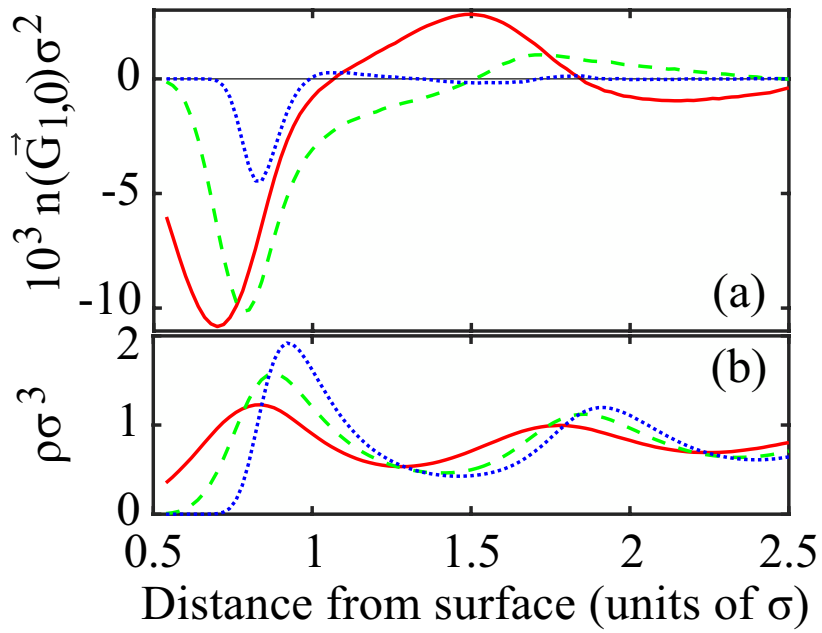

Figure 2.11: (a) Variation of cosine Fourier transform $n(\vec{G})$ of the local area density (averaged over a thin slice) as a function of height for flat surfaces where $\epsilon_{wf} = 0.1\epsilon$ and $a = 1.2\sigma$ (red solid), 1.00σ (green dashed), and 0.75σ (blue dotted). The solid line designates $n(\vec{G}) = 0$. (b) Fluid density profiles for the same surfaces.

transition to $n(\vec{G}) > 0$ indicates that the atoms are not responding to the direct interaction with the wall, but instead to the density modulation in fluid atoms that lie closer to the wall where $n(\vec{G}) < 0$. The lack of coherence in the first density peak reduces the lifetime of the associated mode and thus t_{ph} is smaller than in the two dimensional approximation of Eq. (2.29).

It is possible to choose different definitions of the layer width that improve the quantitative agreement with Eq. (2.28). For example, choosing the top of the first layer to coincide with the height where $n(\vec{G})$ first becomes positive, improves quantitative agreement in all cases. However, deviations for large a_{eff} remain larger than the statistical uncertainties.

In Refs. [30, 31], the drag coefficient β along the axial direction was explored for carbon nanotubes. They used a fluctuation dissipation argument that is closely related to the above discussion in the linear response limit. They find

$$\beta = \frac{t_F \bar{n}_1}{k_B T} \sum_{\vec{G}} S_{1,eq}(\vec{G}) f_1^2(\vec{G}), \tag{2.30}$$

where t_F is the force decorrelation time at equilibrium and $f_1(\vec{G})$ is the Fourier component of the force field along the flow direction. They did not specifically state that the equilibrium structure factor rather than the induced peak should be used in Eq. (2.30) but the density modulations were too small to influence $S_1(\vec{G})$ in their system and this identification is consistent with their discussion.

Note that Eq. (2.30) has many similarities to Eq. (2.26). Since $f_1(\vec{G}) = U(\vec{G})(\vec{G} \cdot$

$\Delta\hat{u}$), both expressions predict quadratic scaling of β with substrate potential. This is the lowest order scaling allowed by symmetry and the quadratic scaling was confirmed in Refs. [33,34] over 3 orders of magnitude in β. As discussed above, $S_{1,eq}(\vec{G})$ is related to the response to the substrate potential.

In Appendix A we show that Eq. (2.30) is quantitatively consistent with both L_s and the theory of Smith *et al.* [Eq. (2.28)] for a model potential that is uniform throughout the first layer. However for the actual atomistic potential, Eq. (2.30) is less accurate because of the variations in order shown in Fig. 2.11. Falk *et al.*[31] note that the rapid decay of the potential corrugation with height leads to a quantitative discrepancy from their theory by a "constant prefactor of 10 or less, depending on the liquid". Appendix A shows that the prefactor may depend on the solid as well as the liquid. We also show that the initial fluctuation-dissipation argument that leads to Eq. (2.30) breaks down for atomistic interactions.

2.4 Summary and Conclusions

We have used molecular dynamics simulations of flows in planar and cylindrical geometries to study the variation of the slip length with surface curvature for a range of geometries and surface interactions. Curvature at nanometer scales can increase or decrease L_s by an order of magnitude, depending on the direction of flow and surface geometry. The results explain why little change in L_s was seen in one previous study[32] while another found large changes.[30,31]

The slip length scales inversely with the viscous drag β between the first fluid layer and the solid wall, $L_s = \mu/\beta$. As in previous studies of flat surfaces,[22,26,27,30,31,35,155,158–160] the drag is directly related to lateral density modulations induced in the fluid by the wall potential. The magnitude of this epitaxial order increases with the strength of the corrugations in the wall potential and also with the susceptibility of the fluid to respond to the potential. This susceptibility is greatest when the separation between minima in the potential is comparable to the spacing between fluid atoms in the first layer.

Curvature changes the effective separation a_{eff} between minima because the fluid atoms lie at a different radius than the solid substrate. As shown in Fig. 2.6, positive curvature increases the spacing because fluid atoms are at a larger radius, while negative curvature decreases the spacing. The fractional change in the spacing between potential minima is $\sim \kappa d_1$ where d_1 is the height of the first fluid layer above the solid.

A natural measure of the ratio between the spacing of minima and the spacing between fluid atoms is $a_{eff}\bar{n}_1^{1/2}$ where $\bar{n}_1$ is the areal density of fluid atoms in the first layer. Independent measures of the susceptibility (see Appendix A) show that the fluid is most able to lock into the potential corrugation when $a_{eff}\bar{n}_1^{1/2} \approx 0.8$ and the susceptibility drops as a_{eff} increases or decreases. Fig. 2.9(b) shows that the slip length is smallest (β is largest) at slightly larger a_{eff} and changes much more rapidly with decreases in a_{eff} than increases in a_{eff}. This asymmetry reflects

changes in the strength of the periodic corrugation from the substrate. Increasing the spacing between solid atoms allows fluid atoms to penetrate more deeply into the spaces between them and greatly increases the lateral variation in potential energy. Decreasing the spacing between solid atoms makes the potential more nearly constant. As $a_{eff}\bar{n}_1^{1/2}$ decreases below 0.8, the decrease in corrugation and susceptibility both reduce β leading to a rapid rise in L_s. As $a_{eff}\bar{n}_1^{1/2}$ increases above 0.8, the increase in corrugation partially offsets the drop in susceptibility and L_s rises slowly.

Curvature does not affect the spacing along the cylinder axis. This explains why there is almost no change in L_s for axial flow and large changes for radial flow when the nearest-neighbor atoms of a square surface lattice are aligned along the axis. However, when the next-nearest neighbors are along the cylinder axis, L_s changes more for axial flow than radial flow. This change in behavior can be understood by considering how the density modulations produced by the substrate are affected by flow. The largest modulations are at the smallest reciprocal lattice vectors of the substrate $\vec{G}$. Flow only affects modulations with a component of $\vec{G}$ along the flow velocity $\vec{v}$. When the nearest-neighbor direction is along the axis there is a reciprocal lattice vector along the axis and another perpendicular. Curvature only affects the perpendicular vector and thus does not affect axial flow. When the next-nearest neighbor direction is along the axis, the reciprocal lattice vectors have both axial and radial components. Curvature rotates the reciprocal lattice vectors towards the axial direction so that axial slip lengths change most [Eq. (2.24)].

Falk *et al.* considered axial flow over nanotubes with hexagonal symmetry.[30,31] In this case the reciprocal lattice vectors are not parallel to the nearest-neighbor spacing. Thus they found large changes for axial flow when the nearest-neighbor direction was along the axis. For this lattice there should be almost no change in axial flow if the nearest-neighbor direction is along the radial direction. Nanotubes can be grown with this orientation.

All the observed changes in slip length can be understood in terms of a simple model for friction between the first fluid layer and the substrate.[33,34] In this model the viscous drag is directly related to $|\hat{G}\cdot\hat{v}|^2$ times the strength of the density modulations produced by the substrate as measured by the in-layer structure factor $S_1(\vec{G})/N_1$. The changes in structure factor are inverse to the changes in L_s noted above (Fig. 2.9 and 2.10(a)). It is largest when $a_{eff}\bar{n}_1^{1/2}$ is near 0.9 and drops off more rapidly at small a_{eff} because the corrugation becomes weaker as the surface is more closely packed.

The only remaining factor in the theory is the inverse phonon lifetime t_{ph} which describes the rate of energy dissipation out of the density modulations. Numerical data for all surface densities, orientations and interactions collapse onto a universal curve when t_{ph} is plotted against $a_{eff}\bar{n}_1^{1/2}$ (Fig. 2.10(b)). The phonon lifetime is largest for $a_{eff}\bar{n}_1^{1/2} \approx 0.8$ where the fluid can most easily lock into epitaxy with the substrate. When the spacing between fluid atoms is larger or smaller, this locking is difficult and the lifetime decreases. The lifetime is further suppressed by the fact that the density modulations are not uniform across the first layer when the spacing

between fluid atoms deviates from a_{eff} (Fig. 2.11).

We compared our results to a model proposed by Falk *et al.* that is also based on the friction between the substrate and first fluid layer.[30,31] The results are equivalent to the theory of Smith *et al.*[33,34] when the potential producing the density modulations is uniform across the two layers (Appendix A). This quantitative agreement breaks down for the more realistic potentials used in the main text because the density modulations vary across the first layer. As noted by Falk *et al.*, the exponential decrease in density modulation with height causes quantitative discrepancies between L_s and Eq. (2.30) by up to an order of magnitude.

Although this study used simple models for both fluid and solid surfaces, the observed trends with curvature should be quite general and the theoretical approach[33,34] can be extended to more complex cases. Potentially important applications are transport of fluids inside and outside carbon nanotubes[30,31,167–171] and other other nanotubes and nanowires. Moreover, many experimental surfaces are rough down to nanometer scales. In this case the effect of topography can not be determined by applying a constant slip length along the surface. There will be intrinsic variations in the local slip boundary condition due to curvature. Including these may explain deviations between past simulations and continuum theories that assume constant L_s[28,29,35,38] and allow construction of a more accurate mesoscopic flow boundary condition.

2.5 Appendix A

In this appendix we describe simulations that were used to calculate L_s using the models in Refs. [30, 31, 33, 34]. These two dimensional models implicitly assume that the periodic potential from the substrate and the response of the fluid are independent of height within the first layer. In the following we associate the first layer with all atoms in the density peak nearest to the wall. The end of the layer is taken to be the position of the first minimum after the peak in plots like Fig. 2.3 or Fig. 2.11. All atoms in the first layer feel the same lateral potential from the wall.

The wall-fluid interaction along the z direction is modeled by a Lennard-Jones 9/3 potential:

$$V(z) = 4\epsilon_{wf}\left[\frac{2}{15}\left(\frac{\sigma}{z}\right)^9 - \left(\frac{\sigma}{z}\right)^3\right] - V_c, \text{ for } r < r_c, \tag{2.31}$$

where $\epsilon_{wf} = 0.1\epsilon$ and the potential is zero for $r > r_c$. To model the lateral corrugation of the wall potential, a lateral force was applied only to fluid atoms in the first layer:

$$\vec{F}(x, y) = -\nabla V_1(x, y) \quad , \tag{2.32}$$

$$V_1(x, y) = 2U_1[\cos(Gx)\sin(\omega t) + \cos(Gy)] \quad , \tag{2.33}$$

where $G = 2\pi/a$ and the strength of the potential corrugation $U_1 = 0.1\epsilon$. We compare to simulations with flow along the x direction and the corrugation along this direction varies sinusoidally in time with frequency ω.

The slip length in Eq. (2.6) is $L_s = \mu/\beta$. To determine β from the theory of

Smith *et al.* we need to calculate the phonon lifetime from Eq. (2.29). In the limit of small ω, the imaginary part of $\alpha(G,\omega)$ is proportional to ω and the magnitude becomes equal to the real part. In this limit we can use Eq. (2.25) to write $\omega|\alpha(G,0)|/\mathrm{Im}[\alpha(G,\omega)] = \omega\mathrm{Re}[n_1(G,\omega)]/\mathrm{Im}[n_1(G,\omega)]$, where $n_1(G,\omega)$ is the areal density modulation in the first layer due to the time dependent corrugation in Eq. (2.33). We evaluated this ratio for progressively lower frequencies to determine the limiting value for each system. The ratio typically converged for $\omega\tau < 0.001$. Then $|\alpha(G,0)|$ was determined from the ratio $|n(G,0)|/U_1$ evaluated in steady state ($\omega = 0$) and t_{ph} was calculated from Eq. (2.29).

For the ideal wall potential of Eq. (2.33), we can also quantitatively compare Eq. (2.28) with the model proposed by Falk *et al.*[30,31] The periodic force in Eq. (2.30) is $f_1(\vec{G}) = (\vec{G}\cdot\Delta\hat{u})U(\vec{G})$. Thus the only additional quantity to be evaluated is the force decorrelation time

$$t_F = \frac{\int_0^\infty dt < F_x(0)F_x(t) >}{< F_x(0)F_x(0) >}, \tag{2.34}$$

where F_x is the total force between the fluid and the substrate along the x axis. Note that equating the expressions for β from the two theories gives a relation between t_F and t_{ph}:

$$\frac{t_F}{k_BT}\frac{|\vec{G}|^2\bar{n}_1^2}{|\alpha(\vec{G},0)|^2}S_{1,eq}(\vec{G}) = \frac{1}{t_{ph}(\vec{G},\vec{G}\cdot\Delta\vec{u})}. \tag{2.35}$$

Falk *et al.* note that there is a long tail in the integrand for the force decorrelation time due to hydrodynamic effects. They argue this should not be included in t_F.

Following their procedure, we evaluated t_F by taking the plateau value of the integral of Eq. (2.34). An alternative Green-Kubo relation that avoids long tails has been developed by Huang and Szlufarska.[172]

Calculated results for the slip length from both theories are compared to values determined from flow simulations in Fig. 2.12. All results are equivalent within the statistical errors and show the trends with the ratio of wall atom to fluid atom spacing, $a\bar{n}_1^{1/2}$, that were identified in the main text. The slip length is shortest when the wall spacing and fluid spacing are similar so that the fluid can more readily lock in phase with the substrate. The slip length increases with the mismatch in lengths.

Fig. 2.12 shows that both two-dimensional theories for L_s are accurate for all wall densities when the physical system is effectively two-dimensional. However, as noted in the main text, atomic surfaces produce a lateral corrugation in potential that can change substantially within the first layer. The theory of Smith *et al.* remains quantitatively accurate when the wall and fluid have similar spacings, but predicts too large a phonon lifetime for larger and smaller a. One can view this as a reduction in the lifetime of density modulations that are not coherent across the layer.

We found significant quantitative differences between L_s and the theory of Falk *et al.* for atomistic surfaces with all spacings. When one evaluates f_1 at the density peak, as they suggest, their model gives values of L_s that are up to an order of magnitude too large. Given the variation in modulation with height one may wonder whether other definitions could improve the quantitative agreement, but we also found

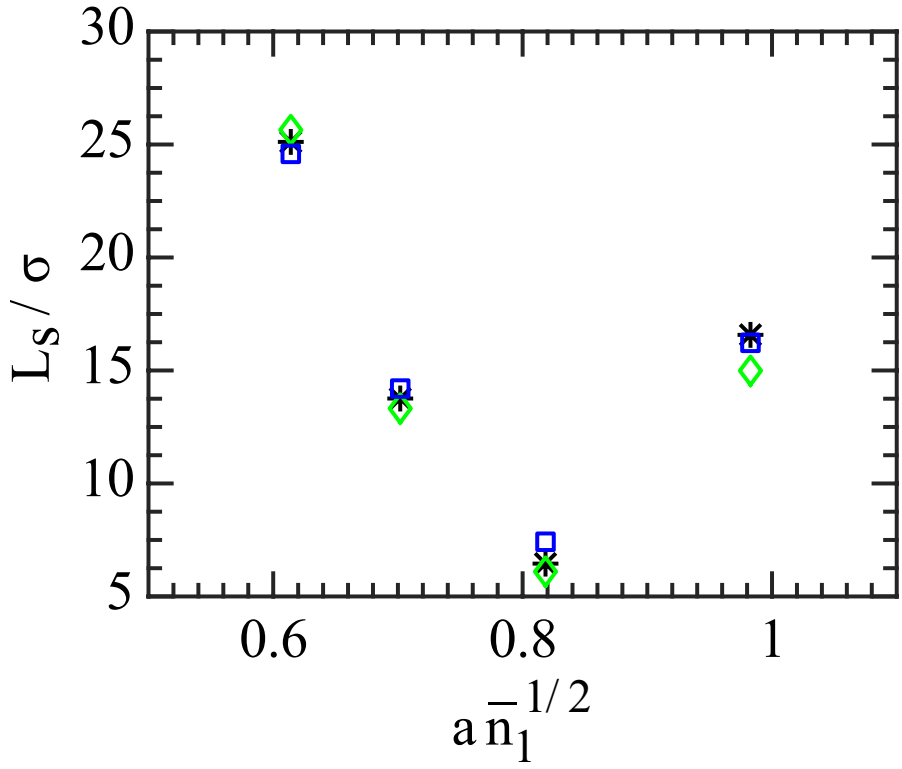

Figure 2.12: The variation of slip length as a function of the relative wall spacing $a\bar{n}_1^{1/2}$ for the ideal wall potential of Eq. (2.32). Asterisks show the slip length determined directly from the Couette profile, diamonds are from the theory of Smith *et al.* [Eq. (2.28)], and squares are from the theory of Falk *et al.* [Eq. (2.30)]. Symbol sizes are comparable to statistical errorbars.

a breakdown in the fluctuation-dissipation relation used to derive their expressions. Their starting point is

$$\beta^F = \int_0^\infty dt < F_x(0)F_x(t) > /Ak_BT \tag{2.36}$$

where the left-hand side represents the dissipation, the right-hand side is the fluctuation and the superscript F indicates that this is the prediction of their model. Fig. 2.13 shows the ratio of β^F to the directly measured value of $\beta = \mu/L_s$. The ratio decreases linearly with a and Eq. (2.36) is wrong by up to a factor of 2. Of course this does not represent a failure of the fluctuation-dissipation approach, but rather an assumption about how the dissipation is related to flow. Converting β^F to a slip length requires assuming that the first layer is moving coherently and this approximation is invalid because of the rapid change in corrugation potential with height.

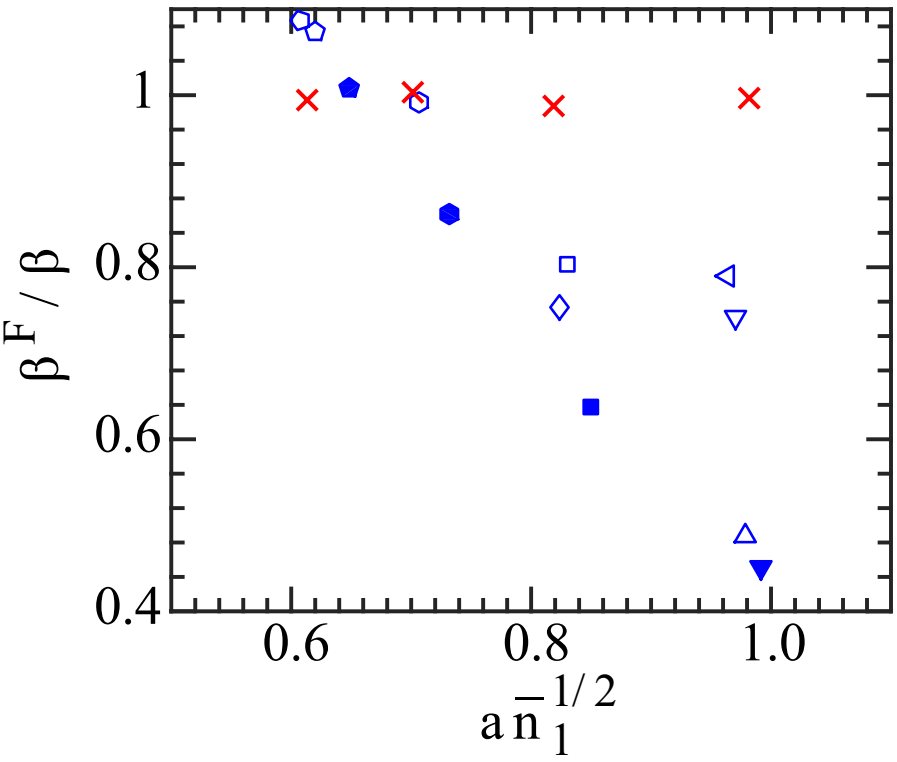

Figure 2.13: Ratio of the drag coefficient predicted by Eq. (2.36) to the measured drag coefficient $\beta = \mu/L_s$ as a function of the relative wall spacing $a\bar{n}_1^{1/2}$. Red crosses show results for the ideal wall potential of Eq. (2.32). Blue symbols show results for flow along the (110) direction of flat atomic walls with lattice spacing $a = 1.2\sigma$ (triangles), 1.09σ (circles), 1.00σ (squares), 0.86σ (hexagons) and 0.75σ (pentagons). The symbol type indicates the wall-fluid interaction from Table 2.1: A (open), B (closed), C (right-side left triangle and pentagon) and D (diamond and right-side up triangle).

2.6 Appendix B

This appendix presents tables of values of slip length and normalized structure factor measured from simulations for different system geometries and surface types.

a/σ	Wall Type	Orientation	L_s/σ		$\tilde{S}_1(\vec{G}_{main})/N_1 \times 100$
			Langevin	DPD	
1.20	A	(110)	1.42	1.45	7.72
		(100)	1.43	1.42	
1.20	B	(110)	0.56	–	13.85
1.20	C	(110)	2.32	–	4.21
1.20	D	(110)	3.91	4.03	2.26
1.09	A	(110)	1.71	1.73	7.46
1.09	B	(110)	0.66	–	15.49
1.00	A	(110)	2.53	2.56	5.40
		(100)	2.45	2.58	
1.00	B	(110)	1.09	–	11.78
1.00	D	(110)	8.70	–	1.66
0.86	A	(110)	8.79	8.91	0.93
0.86	B	(110)	3.77	–	2.30
0.75	A	(110)	22.62	23.17	0.17
		(100)	21.77	22.29	
0.75	B	(110)	10.96	11.21	0.41
0.75	C	(110)	31.26	–	0.11

Table 2.2: Results for planar surfaces with wall interactions in Table 2.1 of main text. L_s is measured from planar Couette flows along the (110) or (100) directions with Langevin or DPD thermostats. Statistical errors are below 2%. $\tilde{S}_1(\vec{G}_{1,0})/N_1$ is measured for equilibrium systems with the Langevin thermostat and simulations with the DPD thermostat gave the same results. The statistical errors are below 5%.

a/σ	Wall Type	Wall Radii	L_s/σ				$\tilde{S}_1/N_1 \times 100$			
			Angular		Axial		$\vec{G}_{1,0}$		$\vec{G}_{0,1}$	
		$(R_{wi}, R_{wo})/\sigma$	i	o	i	o	i	o	i	o
1.20	A	(3.85, 23.00)	1.84	1.31	1.52	1.47	2.67	9.38	6.38	7.78
		(7.67, 26.83)	1.68	1.31	–	–	4.38	9.09	6.99	7.72
1.20	B	(3.85, 23.00)	1.01	0.43	–	–	3.74	17.76	9.80	14.17
		(7.67, 26.83)	0.83	0.50	–	–	6.94	16.97	11.62	14.17
1.20	C	(3.85, 23.00)	3.02	2.32	–	–	1.24	5.40	3.49	4.25
		(7.67, 26.83)	2.71	2.11	–	–	2.18	5.20	3.79	4.28
1.20	D	(3.85, 23.00)	4.85	3.51	4.29	3.85	0.62	3.12	1.96	2.34
		(7.67, 26.83)	4.33	3.54	–	–	1.01	2.96	2.09	2.38
1.09	A	(3.85, 23.00)	2.31	1.70	1.78	1.71	2.35	7.95	6.94	7.23
		(7.67, 26.83)	2.04	1.74	–	–	4.01	7.89	7.16	7.19
1.09	B	(3.85, 23.00)	1.32	0.82	–	–	4.07	16.44	14.19	14.61
		(7.67, 26.83)	0.97	0.71	–	–	8.03	16.48	15.53	14.68
1.00	A	(3.84, 23.00)	2.78	3.07	2.70	2.50	2.46	4.33	5.18	5.45
		(7.67, 26.83)	2.27	2.80	–	–	4.48	4.52	5.07	5.37
1.00	B	(3.84, 23.00)	1.44	1.50	–	–	4.68	9.42	12.36	12.43
		(7.67, 26.83)	1.02	1.31	–	–	9.44	9.67	12.21	12.44
1.00	D	(3.84, 23.00)	7.68	10.08	–	–	0.68	1.19	1.47	1.64
		(7.67, 26.83)	6.85	9.18	–	–	1.34	1.29	1.60	1.64
0.86	A	(3.84, 23.00)	3.40	9.72	9.32	8.46	3.40	0.60	0.76	0.93
		(7.67, 26.83)	4.45	9.41	–	–	2.77	0.63	0.87	0.91
0.86	B	(3.84, 23.00)	1.05	4.83	–	–	10.25	1.43	1.70	2.38
		(7.67, 26.83)	1.32	4.68	–	–	9.08	1.50	1.91	2.40
0.75	A	(3.84, 23.00)	7.91	22.63	23.10	21.27	1.42	0.13	0.15	0.17
		(7.67, 26.83)	14.39	21.99	–	–	0.45	0.13	0.16	0.17
0.75	B	(3.84, 23.00)	1.92	11.00	12.10	10.24	6.13	0.32	0.33	0.42
		(7.67, 26.83)	5.62	10.97	–	–	1.38	0.33	0.38	0.42
0.75	C	(3.84, 23.00)	12.69	31.17	–	–	0.91	0.09	0.10	0.11
		(7.67, 26.83)	21.05	31.41	–	–	0.30	0.09	0.11	0.11

Table 2.3: Results for cylindrical surfaces with axis along the nearest-neighbor (110) direction and the indicated inner (i) and outer (o) radii. Wall type is given in Table 2.1 of main text. L_s is measured from angular flows with inner wall speed $U_w = 0.2\sigma/\tau$ and axial flows with inner wall speed $U_w = 0.6\sigma/\tau$. Statistical errors are below 2%. $\tilde{S}_1/N_1$ is measured in equilibrium systems at $\vec{G}_{1,0}$ and $\vec{G}_{0,1}$, the smallest reciprocal lattice vectors in the angular and axial direction, respectively. Statistical errors are below 5%.

a/σ	Wall Type	Wall Radii	L_s/σ				$\tilde{S}_1(\vec{G}_{main})/N_1$ $\times 100$	
			Angular		Axial			
		$(R_{wi}, R_{wo})/\sigma$	i	o	i	o	i	o
1.20	A	$(4.09, 21.69)$	2.00	1.38	1.56	1.43	0.47	0.56
1.00	A	$(4.09, 21.69)$	2.50	2.51	1.87	2.80	1.19	0.61
0.75	A	$(4.08, 21.68)$	19.27	20.87	13.80	23.27	2.74	1.10
		$(8.14, 25.75)$	20.42	21.23	17.20	22.87	2.20	2.82

Table 2.4: Results for cylindrical surfaces with axis along the next-nearest-neighbor (100) direction and the indicated inner (i) and outer (o) radii. Wall type is given in Table 2.1 of main text. L_s is measured from angular flows with inner wall speed $U_w = 0.2\sigma/\tau$ and axial flows with inner wall speed $U_w = 0.6\sigma/\tau$. Statistical errors are below 2%. $\tilde{S}_1/N_1$ is measured in equilibrium systems and statistical errors are below 5%. $\vec{G}_{main}$ is one of the four smallest reciprocal lattice vectors which are equivalent by symmetry.

Chapter 3

Effective Slip Boundary Conditions for Sinusoidally Corrugated Surfaces

3.1 Introduction

Progress in the design and fabrication of micro-and nanofluidic devices has raised the importance of precisely modeling the transport properties of fluids near solid surfaces. Conventional continuum hydrodynamics treats interfacial effects as boundary conditions applied to mathematically sharp interfaces. As the system size shrinks to micro- or nanoscales, the classical no-slip boundary condition for macroscopic hydrodynamics may be violated, and fluid flow can be substantially modified by fluid slip at the solid surface.[1,6,7,133,134]

Navier proposed a widely used slip boundary condition for flat and homogeneous surfaces,[21] which postulates that the slip velocity is proportional to the shear rate of the fluid at the surface. The slip length (also referred to as intrinsic slip length) is introduced as the proportionality coefficient, and is used to characterize the degree of slip. Previous molecular dynamics studies[22–27,155,173] have reported that, at small

shear rates, the slip length is determined by the properties of the fluid (e.g., viscosity, temperature, fluid structure) and the atomic-scale properties of the interface (e.g., wall-fluid interaction strength, atomic structure of the surface).

In most real systems, the solid surfaces are rough at small scales. To describe the bulk fluid flow away from the surface, it is appropriate to define an effective Navier slip boundary condition to account for the mean effects of the variations in height and local wall-fluid coupling along the real surface.[29,35–38,40,174] The effective slip length measures the distance from the location of the mean height of the surface to the virtual plane where the extrapolated velocity from the bulk flow profile coincides with that of the solid wall. A larger (more positive) effective slip length indicates a smaller effective drag coefficient between the fluid and wall.

Because of the potential applications, especially in drag reduction and flow control, the effects of surface roughness have been extensively studied by means of experiments, simulations and theory. Usually, wall roughness decreases the degree of effective slip.[18,35,37,38,41–46] However, it is well known that highly hydrophobic rough surfaces may trap gas bubbles in the valleys and form a Cassie state, which can dramatically enhance the effective slip.[47–58,174,175] In contrast to the conventional point of view, it has also been reported that roughness may generate very large effective slip even in the Wenzel state, where there is no gas trapped in valleys.[59,60] If the corrugations on the surface are anisotropic, then the effective slip length becomes anisotropic too.[39,57,61–67]

CHAPTER 3. EFFECTIVE SLIP BOUNDARY CONDITIONS FOR SINUSOIDALLY CORRUGATED SURFACES

The above work clearly shows surface roughness can significantly affect the effective wall-fluid coupling. However the mechanisms involved are not yet fully understood, due to the complex interplay of the various atomic and continuum effects associated with the wide range of roughness length scales.

In this study, we use molecular dynamics (MD) simulations to investigate the anisotropic slip of Newtonian monatomic fluids over surfaces with one-dimensional sinusoidal roughness in the Wenzel state. Different types of corrugated surfaces are compared: smoothly bent surfaces where atoms of a crystalline solid are displaced to follow a sine wave, and stepped surfaces that are cut from a crystalline solid. The wavelength is always more than an order of magnitude larger than the atomic diameter, so that effects from atomic discreteness can be separated from those of the large scale corrugations. The wall density and the wall-fluid interaction are varied.

The effective slip length is calculated as a function of the corrugation amplitude for flows along two principal orientations: transverse and longitudinal to the corrugation. MD results for low density (sparse) bent surfaces quantitatively agree with continuum hydrodynamic predictions with a constant local boundary condition. The effective slip length decreases monotonically with increasing corrugation amplitude and the reduction is larger for transverse flow than longitudinal flow. Atomic effects become important for close-packed (dense) bent surfaces. Curvature at the crests of dense rough surfaces produces large variations in the local slip length (Chapter 2 and Ref. [176]). The resulting changes in total effective slip length are captured by

supplementing continuum simulations with local slip boundary conditions obtained for the corresponding curvature and atomic spacing.

Results for stepped surfaces are qualitatively different than continuum predictions. Steps introduce an extra drag for transverse flow that has no analog in continuum theory and has pronounced effects when there is significant slip on flat surfaces. In particular, the analytic scaling at small amplitudes changes from quadratic to linear in the roughness amplitude. This shows that the transverse drag is proportional to the density of step edges. The slip length for longitudinal flow also scales with the density of step edges, but tends to increase with roughness rather than decreasing.

The rest of the chapter is organized as follows. In Sec. 3.2, we describe the details of molecular dynamics and continuum simulations, and how key quantities such as slip length and fluid structure are defined and measured from the simulations. In Sec. 3.3, results for the effective slip length are presented, and the effect of wall roughness is discussed. The summary and conclusions are given in Sec. 3.4.

3.2 Simulation Methods and Analytical Models

3.2.1 Molecular Dynamics Simulations

Standard molecular dynamics is used to simulate simple fluid flows over rigid solid walls. The simulations are performed with the open source package LAMMPS from Sandia National Laboratories.[136] A truncated Lennard-Jones (LJ) potential is used

to model the interactions between fluid atoms:

$$V_{LJ}(r) = 4\epsilon\left[\left(\frac{\sigma}{r}\right)^{12} - \left(\frac{\sigma}{r}\right)^{6}\right] - V_c, \text{ for } r < r_c \tag{3.1}$$

where r is the distance between the two atoms, and ϵ and σ define the characteristic energy and length scales of the fluid, respectively. To save computational cost, V_{LJ} is truncated at a distance $r_c = 2.2\sigma$, and V_c is chosen so that $V_{LJ}(r_c) = 0$. Wall (w) and fluid (f) atoms also interact through a truncated LJ potential with parameters ϵ_{wf}, σ_{wf} and the same cutoff distance $r_{c,wf} = 2.2\sigma$.

The equations of motion are integrated using the velocity-Verlet algorithm with a time step $\Delta t = 0.005\tau$, where $\tau = \sigma\sqrt{m/\epsilon}$ is the characteristic time scale and m is the mass of a fluid atom. Fluid temperature is maintained at $T = 1.1\epsilon/k_B$ by imposing a Langevin thermostat on all fluid atoms in a direction perpendicular to the bulk flow and flow gradient. For example, for flows along the x (y) direction and walls separated in the z direction, the Langevin thermostat is applied in the y (x) direction (Figure 3.1).[22,137] The thermostatted equation of motion in the y direction is given by

$$m\ddot{y} = f_{LJ} - m\Gamma\dot{y} + F(t) \tag{3.2}$$

where f_{LJ} is the total LJ force from all other particles. The damping rate Γ controls the heat flux between the system and the heat bath and $F(t)$ is a random force sampled from a Gaussian distribution with zero mean and variance $2m\Gamma k_B T/\Delta t$. We use a damping rate $\Gamma = 0.5\tau^{-1}$, which effectively eliminates viscous heating without

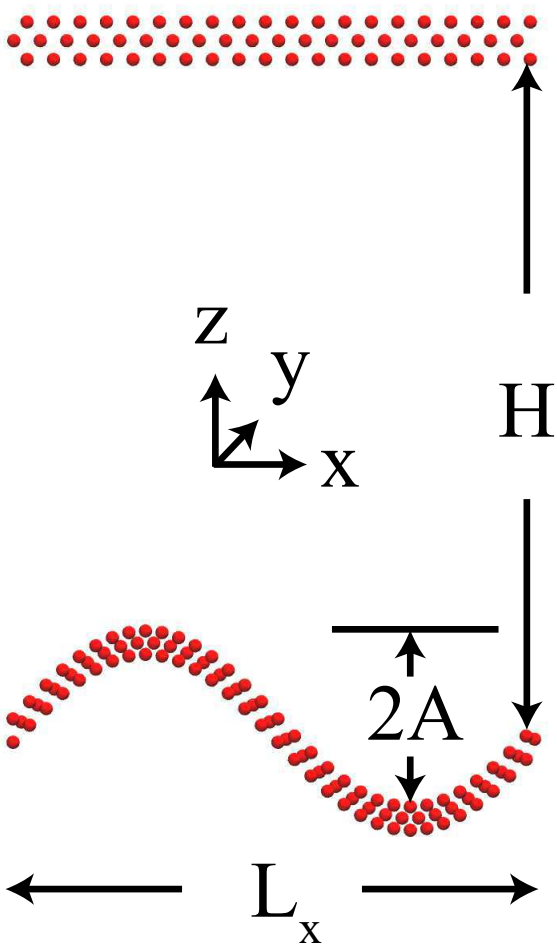

Figure 3.1: Geometry of the MD simulation. Fluid is confined between rigid walls. The bottom wall has a sinusoidal corrugation, $z(x) = A\ \sin(2\pi x/\lambda_x)$, with mean height zero. The surface of the flat top wall is placed at $z = H$, and a no-slip boundary condition is enforced there by choosing a strong wall-fluid interaction. Flow is generated by moving the top wall along either the x or y axis.

causing any substantial disturbances to the atomic motions. In this regime of low damping rate, the thermostat has negligible impact on the effective slip boundary condition on flat surfaces.[22,138,139] We confirmed this remains true even for y direction flows, where weak secondary momentum transfer can occur along the thermostatted x direction. In particular, varying Γ by a factor of 2 or switching to an isotropic momentum-conserving dissipative particle dynamics (DPD) thermostat[140–142] with a damping rate $0.5\tau^{-1}$ had negligible impact on the effective slip length ($< 3\%$).

The density of the bulk fluid is fixed at $\rho = 0.81\sigma^{-3}$. For the low shear rate regime studied here ($< 0.04\tau^{-1}$), the bulk fluid is Newtonian with shear viscosity $\mu \sim 2.13\epsilon\tau\sigma^{-3}$. We verified that the slip length is insensitive to shear rate in this regime.[22,23,27,37,139]

As illustrated in (Figure 3.1), fluid is confined in a channel between two solid walls. Periodic boundary conditions are imposed along x and y directions with the spatial periods denoted by L_x and L_y, respectively. With the bottom wall kept stationary, Couette-type shear flow is generated by moving the top wall along either the x or y direction at a speed $U_w = 1\sigma\tau^{-1}$, so that the flow boundary conditions are measured separately for the two directions. As described below, the interactions between the fluid and top wall are chosen so that there is no slip.

Wall atoms are fixed rigidly to lattice sites. If not stated elsewhere, each flat wall consists of three (001) layers of an FCC crystal with nearest-neighbor spacing a_0 [Figures 3.1 and 3.2(a)]. The x axis is aligned with the [110] vector of the FCC lattice

(nearest-neighbor direction). The nominal position of the wall surface is defined by the height of wall atoms in the layer closest to the fluid. The top wall is flat and the surface is placed at height $z = H$. If the bottom wall is flat, its surface is located at $z = 0\sigma$.

Three different methods are used to create sinusoidal bottom walls, resulting in three types of atomic scale structures, as depicted in Figure 3.2:

- A Type I wall [Figure 3.2(b)] is constructed by displacing the solid atoms of a flat wall along the z direction by a distance $\Delta z(x) = A \sin(2\pi x/\lambda_x)$.[35] The parameters A and λ_x denote the amplitude and wavelength of the corrugation, respectively. As shown in Figure 3.2(b), the displacement deforms the lattice structure of the wall. The lateral spacing between the nearest-neighbor atoms along the surface layer increases with the absolute value of the local slope.

- A Type II wall [Figure 3.2(c)] is also made by curving a flat wall along the x direction so that the atoms of the surface layer adjacent to the fluid follow the curve $z(x) = A \sin(2\pi x/\lambda_x)$, but the lateral spacing between neighbors is kept constant. The atomic arrangement along the y direction remains unchanged. Additional rows of atoms along the x direction are included in each layer, to ensure that the surface layer has a locally square structure with nearest-neighbor spacing a_0 as in the original flat surface.[37,176] The number of rows must be an integer and the period L_x is increased to 48.17σ to allow us to sample more amplitudes in the range of interest.

- A Type III wall [Figure 3.2(d)] is carved out from an FCC crystal with the same atomic arrangement as the flat wall. All atoms above the sinusoidal wave $z(x) = A\sin(2\pi x/\lambda_x)$ are removed.[177] Special care is taken to choose the height of lattice planes so that the heights of surface steps are symmetric about the x-y plane ($z = 0$).

The Type I and II surfaces are referred to as bent surfaces, while the Type III surfaces are called stepped surfaces. At zero amplitude, $A = 0\sigma$, the FCC (001) flat surface is recovered for all three types. If not stated elsewhere, $H = 30\sigma$, $L_x = L_y = 24.08\sigma$, and $\lambda_x = 24.08\sigma$. Varying λ_x by a factor of two produces similar trends in the effective slip length.

The lateral separation of the nearest-neighbor atoms in the surface layer is an important parameter of the wall, because it determines the characteristic length of the atomic-scale roughness in the wall potential felt by fluid atoms. It regulates not only the degree of local slip, but also how the slip varies in response to wall curvature.[22,176] In this study, we investigate effective slip boundary conditions for both sparse ($a_0 = 1.2\sigma$) and close-packed ($a_0 = 0.75\sigma$) walls, where the lateral spacings at the original flat surfaces are respectively larger and smaller than the characteristic spacing of the fluid atoms. Our previous studies of curved surfaces showed that these wall spacings provide interesting limiting cases of high and low density.[176] The different sets of wall-fluid interaction parameters studied are listed in Table 3.1. If not mentioned otherwise, $\sigma_{wf} = 1\sigma$. When ϵ_{wf} is decreased or σ_{wf} is increased, the wall-fluid

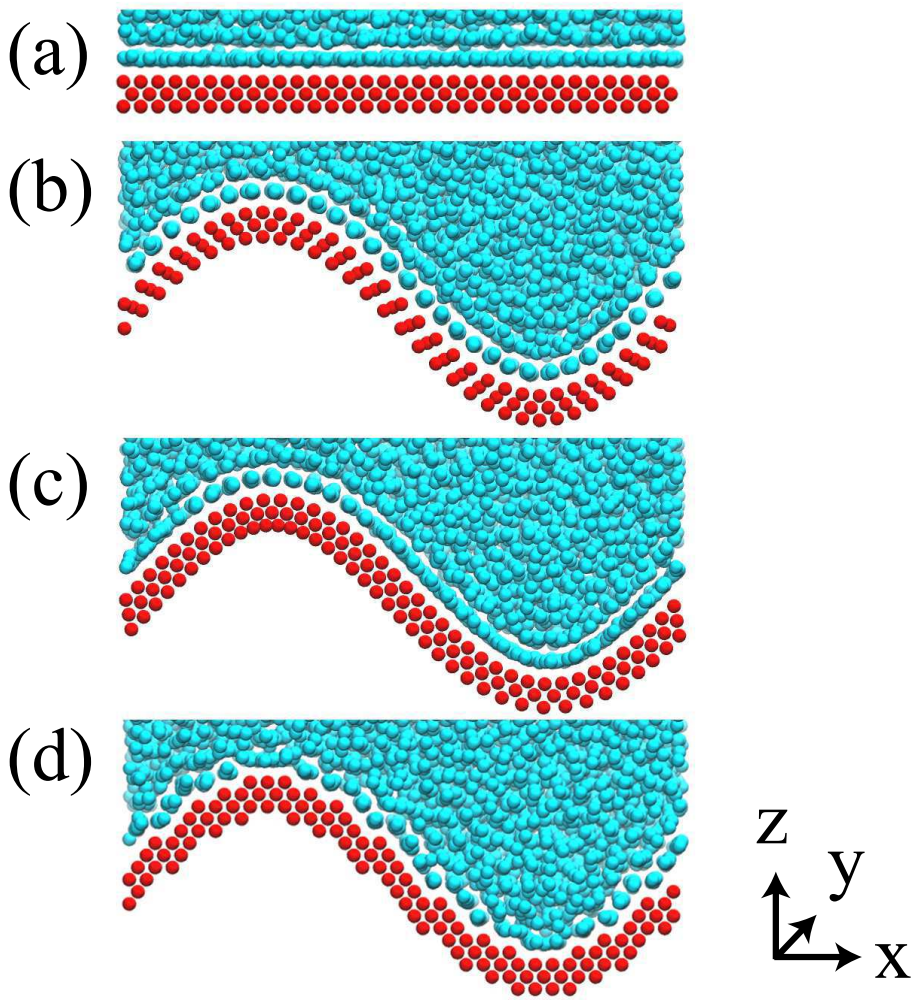

Figure 3.2: Snapshots of the fluid atoms near (a) a flat surface and near three corrugated surfaces of different types: (b) Type I, (c) Type II , and (d) Type III . The fluid and solid atoms are colored in cyan (light) and red (dark), respectively. The wall parameters are $a_0 = 0.75\sigma$, $\epsilon_{wf} = 1.8\epsilon$ and $\sigma_{wf} = 1\sigma$, and the corrugation amplitude A is around 4σ. The systems are at equilibrium.

coupling is weakened and slip is enhanced. The top wall is kept at $a_0 = 1.2\sigma$. No-slip boundary conditions are always enforced at top surfaces by using large values of ϵ_{wf}.

3.2.2 Fluid Structure near Wall

In general, two types of structure are induced in a fluid in contact with a solid surface: density layering perpendicular to the surface and epitaxial ordering within the layers. Examples of the layering effect near flat walls are presented in Figure 3.3 for the various wall parameters listed in Table 3.1. The fluid density profiles oscillate near solid walls, and gradually relax to the uniform bulk value far away from the walls. Several layers can be identified with peaks in the profiles that are separated by density minima.[22,25,95,148–157,176] The position and strength of the first peak is determined mainly by the wall/fluid interaction and the relative spacing of fluid atoms and the minima in the wall potential. However, the strength of the layering effect does not necessarily correlate with the degree of fluid slippage at the solid surface.[22,26,27,30,31,35,155,158–160]

Previous studies have shown that the flow boundary condition for a simple fluid is instead correlated with the amount of epitaxial order within the first fluid layer induced by the atomic-scale roughness in the wall potential.[22,26,27,30,31,35,155,158–160,176] To describe the in-layer structure at a flat surface, the 2D static structure factor, $S_1(\vec{q})$, is calculated as a function of wave vector $\vec{q}$ for the first layer of fluid atoms:

$$S_1(\vec{q}) = S_1(q_x, q_y) = |\sum_j \exp[i(q_x x_j + q_y y_j)]|^2 / N_1, \tag{3.3}$$

Index	a_0/σ	ϵ_{wf}/ϵ	σ_{wf}/σ	$L_{s,0}/\sigma$	
				(001)	(111)
A	1.20	0.4	1	0.56	1.54
B	1.20	1.8	1	-1.11	-0.29
C	1.20	0.00024	2.00	7.35	13.18
D	0.75	0.4	1	10.96	22.66
E	0.75	1.8	1	0.73	8.42

Table 3.1: Parameters of the five groups of solid bottom walls presented in this chapter, i.e., the lattice constant of flat wall a_0, interaction energy ϵ_{wf}, and interaction length σ_{wf}, and intrinsic slip length $L_{s,0}$ at (001) and (111) surfaces along the [110] direction.

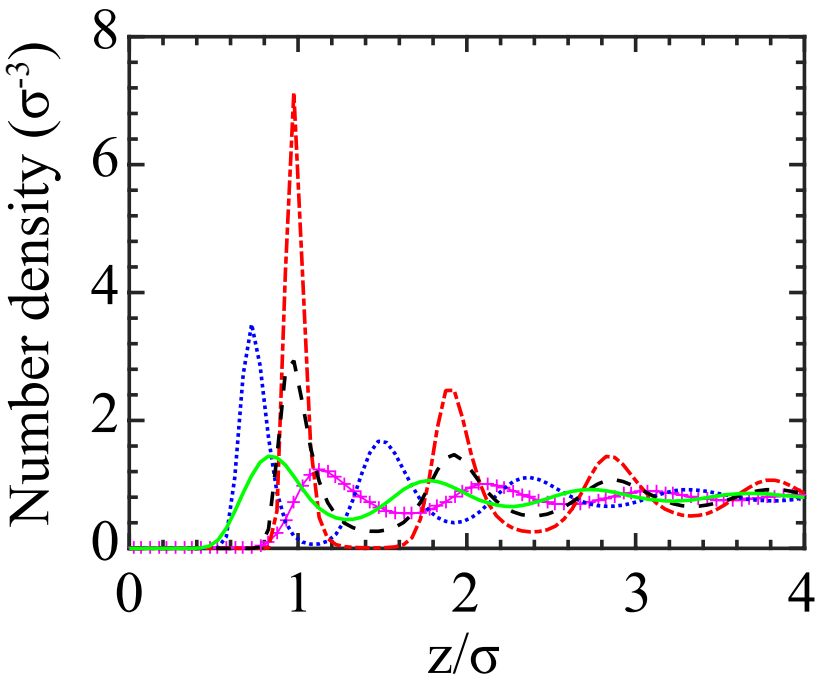

Figure 3.3: Fluid density as a function of distance from wall surface for flat surfaces with the parameters tabulated in Table 3.1: A (solid green line), B (dotted blue line), C (solid magenta line with crosses), D (dashed black line), and E (dash-dot red line). The hydrodynamic boundary condition is defined relative to the height of the first density peak, $d_{1,0}$ for each case.

where x_j and y_j are the 2D coordinates of atom j and N_1 is the number of fluid atoms in the first layer. The allowed wave vectors are determined by the periods of the system in the x-y plane, $\vec{q} = (2\pi h/L_x, 2\pi k/L_y)$ where h and k are integers. The periodic potential of the wall induces Bragg peaks at the corresponding reciprocal lattice vectors $\vec{G}_{m,n}$ of the wall. For the FCC (001) surface, $\vec{G}_{m,n} = (2\pi m/a_0, 2\pi n/a_0)$. More generally, if the nearest-neighbor spacings along x and y (denoted by a_x and a_y, respectively) are different from each other, $\vec{G}_{m,n} = (2\pi m/a_x, 2\pi n/a_y)$.

The structure factors for flat walls (shown in Figure 3.7) are obtained in the equilibrium state. Structure factors are typically evaluated every 0.05τ and temporally averaged over up to 500τ.

3.2.3 Determining Intrinsic and Effective Slip Lengths

For a Newtonian fluid flow past an impenetrable solid surface, Navier's slip model assumes that the drag per unit area on the fluid from the solid surface is proportional to the relative velocity Δu_t of the two, which is also referred to as the slip velocity. This drag force is balanced by the viscous shear stress Π_{nt} of the fluid at the surface, where n represents the normal direction to the surface (pointed into the fluid), and t denotes the direction of the slip velocity that is tangential to the surface. The drag coefficient is typically written as μ/L_s,

$$\frac{\mu}{L_s}\Delta u_t = \Pi_{nt}, \tag{3.4}$$

where μ is the Newtonian viscosity, and the intrinsic slip length, L_s, quantifies the degree of slip.

For a flat surface, the viscous stress is related to the strain rate by Newton's law:

$$\Pi_{nt} = \mu \frac{\partial u_t}{\partial n}. \tag{3.5}$$

Combining Eqs. (3.4) and (3.5), one arrives at the conventional Navier slip boundary condition,

$$\Delta u_t = L_s \frac{\partial u_t}{\partial n}. \tag{3.6}$$

Here the slip length L_s corresponds to the distance below the surface where the relative velocity of the fluid extrapolates to zero. For flow along a curved surface, an extra term associated with the surface curvature emerges naturally in the strain rate, and thus Eq. 3.6 needs to be modified.[28,29]

For planar Couette flow between two flat surfaces, the incompressible Newtonian Navier-Stokes equations reduce to $\mu \partial^2 u_x / \partial z^2 = \partial \Pi_{xz} / \partial z = 0$. Solving this equation, one arrives at a linear velocity profile,

$$u_x = A_1 z + A_2. \tag{3.7}$$

The two constants, A_1 and A_2, are determined by the boundary conditions at the wall-fluid interfaces.

Mean velocity profiles from two different flat surfaces are presented in Figure 3.4, and manifest very different behaviors at the stationary bottom surface. For the close-

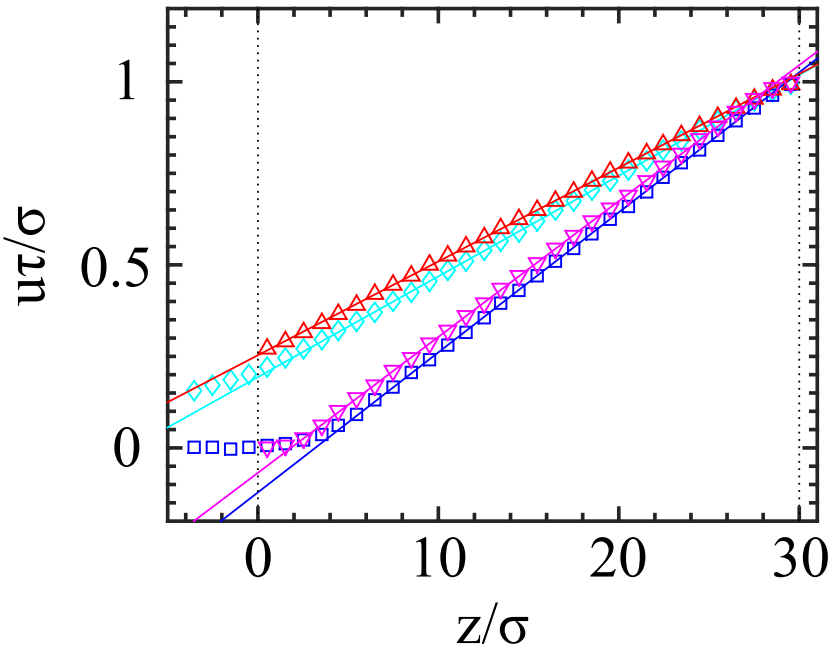

Figure 3.4: Velocity profiles for four cases: Flat surfaces at $a_0 = 1.20\sigma$ and $\epsilon_{wf} = 1.8\epsilon$ (downward magenta triangles) and $a_0 = 0.75\sigma$ and $\epsilon_{wf} = 0.4\epsilon$ (red upward triangles), and sinusoidal surfaces with $A = 4\sigma$, $a_0 = 0.75\sigma$ and $\epsilon_{wf} = 0.4\epsilon$ in the transverse (blue squares) and longitudinal (cyan diamonds) directions. Solid colored lines show fits to Eq. (3.7) and dotted vertical black lines show the positions $z = 0$ and H.

packed surface with $a_0 = 0.75\sigma$ and $\epsilon_{wf} = 0.4\epsilon$, the remarkable velocity difference at the wall signifies a substantial slip. For the sparse surface with $a_0 = 1.20\sigma$ and $\epsilon_{wf} = 1.8\epsilon$, the fluid velocity vanishes inside the fluid, indicating that the fluid atoms in contact with the surface are locked to the wall.[22] This corresponds to a stick boundary condition. In the bulk region several atomic diameters away from wall, both of the profiles can be well fitted by the linear velocity profile [Eq. (3.7)].

Evaluating the slip length from the fitted linear velocity profile [Eq. (3.7)] requires a definition for the position of the hydrodynamic boundary. We choose the height of the density peak associated with the first fluid layer (Figure 3.3), $d_{1,0}$, as the hydrodynamic boundary.[176] The intrinsic slip length at the bottom surface is then obtained from the fit coefficients as

$$L_{s,0} = d_{1,0} + A_2/A_1. \tag{3.8}$$

The subscript 0 denotes that $L_{s,0}$ is measured at the flat surface. Because of the fourfold symmetry of the FCC (001) surface, the slip boundary condition is equivalent along both x and y. In past studies of intrinsic slip boundary conditions, other locations have also been adopted for the hydrodynamic boundary, e.g., the wall surface,[26,161] the middle between the wall surface and the first fluid density peak,[22,30–32] half atomic diameter from wall,[27,178] *etc.*. These common choices for the reference plane differ by less than the layer spacing, resulting in a corresponding small ambiguity in the intrinsic slip length determined by Eq. (3.8).

Figure 3.4 also illustrates two mean velocity profiles over a sinusoidal Type I surface with $A = 4\sigma$. For transverse flow (along x), the mean velocity vanishes below a height of about 4σ, indicating that fluid is trapped in the region between the crests of the sinusoidal surface and moves with the solid. This corresponds to an effective stick boundary condition. For longitudinal (y-direction) flow, the resistance from the sinusoidal corrugation is weaker. The flow is noticeable below the tops of the crests and even below $z = 0\sigma$, corresponding to an effective slip boundary condition. In the bulk region a few atomic diameters above the top of the bottom surface, both of the two flow profiles are nicely fitted by the linear solution for flat surfaces, i.e., Eq. (3.7).

The effective slip lengths, $L_{eff,x}$ and $L_{eff,y}$, are determined using Eq. (3.8) and fits to the linear regions of flow profiles. Consistent with the intrinsic boundary conditions for flat surfaces, the horizontal plane $z = d_{1,0}$ is defined as the effective hydrodynamic boundary. Therefore, $L_{eff,x} = L_{eff,y} = L_{s,0}$ at flat surfaces where the wave amplitude becomes zero.

In the continuum limit, the effective flow boundary condition at an arbitrary direction relative to the sinusoid can be determined by combining the transverse and longitudinal results.[1,38,179] In general the drag coefficient at the wall can be described as a tensor. Choosing the x and y directions to be transverse and longitudinal to the sinusoidal modulation ensures that the off-diagonal matrix elements of the drag tensor vanish in our geometry. The solutions for motion of the top wall in different direc-

tions can be obtained by a simple superposition of the results for the transverse and longitudinal components of the top wall velocity with the corresponding slip length. The anisotropy in slip length will cause the direction of flow to rotate towards the direction with the largest slip length as the distance to the bottom surface decreases.

In simulations, the velocity profiles are averaged within horizontal bins of thickness $\Delta z = 1\sigma$ for a time period of 500τ at steady state. The resulting flow profile is fit to Eq. (3.7) over the region more than 4σ from the top of the surfaces. We verified that changing this condition by $\pm\sigma$ does not produce any noticeable changes. The slip length is then obtained from the fitted coefficients, and further averaged over 20 consecutive time intervals.

In this study, the Reynolds number, given by $Re = \rho H U_w/\mu$, is always around or below 10.[23,35,162] We checked that in this low Re regime, increasing the height H of the top wall (doubling in the MD simulations or increasing by a factor up to 10 in the continuum simulations) does not affect the measured effective slip length.

3.2.4 Continuum Simulations

To isolate the effects from atomic wall structure, continuum simulations are also performed for the same fluid flows, using the software COMSOL Multiphysics 5.1. The effective slip lengths are calculated from the steady-state solutions of the incompressible Newtonian Navier-Stokes (NS) equations,

$$\rho\vec{u}\cdot\nabla\vec{u} = -\nabla p + \mu\nabla^2\vec{u}, \tag{3.9}$$

$$\nabla\cdot\vec{u} = 0. \tag{3.10}$$

As for atomic simulations, the effective slip length is evaluated from the linearly fitted bulk flow profiles and Eq. (3.8). The reference hydrodynamic plane is $z = 0$.

Flows along the x direction are described by the two-dimensional NS equations in the $x - z$ plane.[35–37] A periodic boundary condition is imposed along the x direction with a period of λ_x. The top wall is at $z = H$, moving at a speed U_w along x with a no-slip boundary condition. The stationary substrate is given by $z(x) = A\,\sin(2\pi x/\lambda_x)$.

For the flows along the y direction, the NS equations are solved in the three-dimensional domain that is created by extruding the two-dimensional domain in the y direction. A periodic boundary condition is imposed along the y direction with a period of 5σ. The top wall is moving at the speed U_w along y.

Unless otherwise specified, the stress-based slip boundary condition [Eq. 3.4] is applied on the bottom surface, with a constant local intrinsic slip length determined from the corresponding MD simulation for the flat wall. For the cases of stick boundary conditions ($L_{s,0} < 0$), the bottom surface is shifted upward to $z(x) = A\,\sin(2\pi x/\lambda_x) + |L_{s,0}|$, and a no-slip boundary condition is applied on the shifted surface.

3.2.5 Analytical Models

Panzer *et al.*[28,29] analytically investigated the influence of weak sinusoidal corrugations on the effective slip length in the regime of Stokes flow. The key control parameter is the normalized amplitude KA, where $K = 2\pi/\lambda_x$ is the wave number. KA equals maximum slope of the sinusoidal surface. Assuming the local intrinsic boundary condition to be the same as at a flat surface, they derived an approximation for the transverse slip length $L_{eff,x}$:

$$L_{eff,x} = \frac{L_{s,0}\omega_\infty(KA) - [KA^2\omega_0(KA)]/(1+2KL_{s,0})}{1+K^3A^2L_{s,0}}, \tag{3.11}$$

where

$$\omega_o(KA) = \frac{1-(KA)^2/4+19(KA)^4/64}{1+(KA)^2-(KA)^4/2}, \tag{3.12}$$

and

$$\omega_\infty(KA) = \frac{1-5(KA)^2/4+61(KA)^4/64}{1+(KA)^2-(KA)^4/2}, \tag{3.13}$$

up to terms of order $(KA)^6$.

In the same limit, Kamrin *et al.*[38] also derived second order asymptotic solutions for the effective slip lengths along both the transverse and longitudinal directions. If a small constant slip length $L_{s,0}$ is applied along the surface, the approximate expressions are given by:

$$L_{eff,x} \approx L_{s,0} - KA^2, \tag{3.14}$$

$$L_{eff,y} \approx L_{s,0} - \frac{1}{2}KA^2, \tag{3.15}$$

As the amplitude increases, $L_{eff,x}$ decreases twice as fast as $L_{eff,y}$. The quadratic decay in the transverse direction has also been derived in Refs. [180–182].

3.3 Results and Discussion

3.3.1 Bent Surfaces

Figure 3.5 shows the variation with normalized roughness amplitude KA of the effective slip length for flow over bent surfaces in the transverse (x) and longitudinal (y) directions. Some general trends are seen for all cases. For flows transverse to the sinusoidal corrugations, increasing the amplitude significantly reduces $L_{eff,x}$. As $L_{s,0}$ increases, $L_{eff,x}$ drops more rapidly with increasing KA. For KA near unity, $L_{eff,x}$ tends to decrease linearly at a similar rate for all cases, which is consistent with previous continuum studies (both numerical and analytical).[44,45,180,181,183,184] [1] The slip length in the longitudinal direction, $L_{eff,y}$ also decreases monotonically for most cases, but more slowly than $L_{eff,x}$.

Despite these common general trends there are important differences in the behavior of dense and sparse walls. Results for sparse walls are relatively independent of wall Type (I or II) and agree with continuum theory with a constant local slip length. In contrast, there is strong variation for dense walls that can only be understood by introducing a slip length that varies with the local curvature.

For the sparse surfaces ($a_0 = 1.20\sigma$), the three groups of LJ interaction parameters

[1] In this limit, a weak vortex may form in the valley if the local slip is small,[36,185] but the emergence of the vortex has little impact on the pattern of behavior of the effective slip length with varying KA in the low Reynolds number limit studied here.[185]

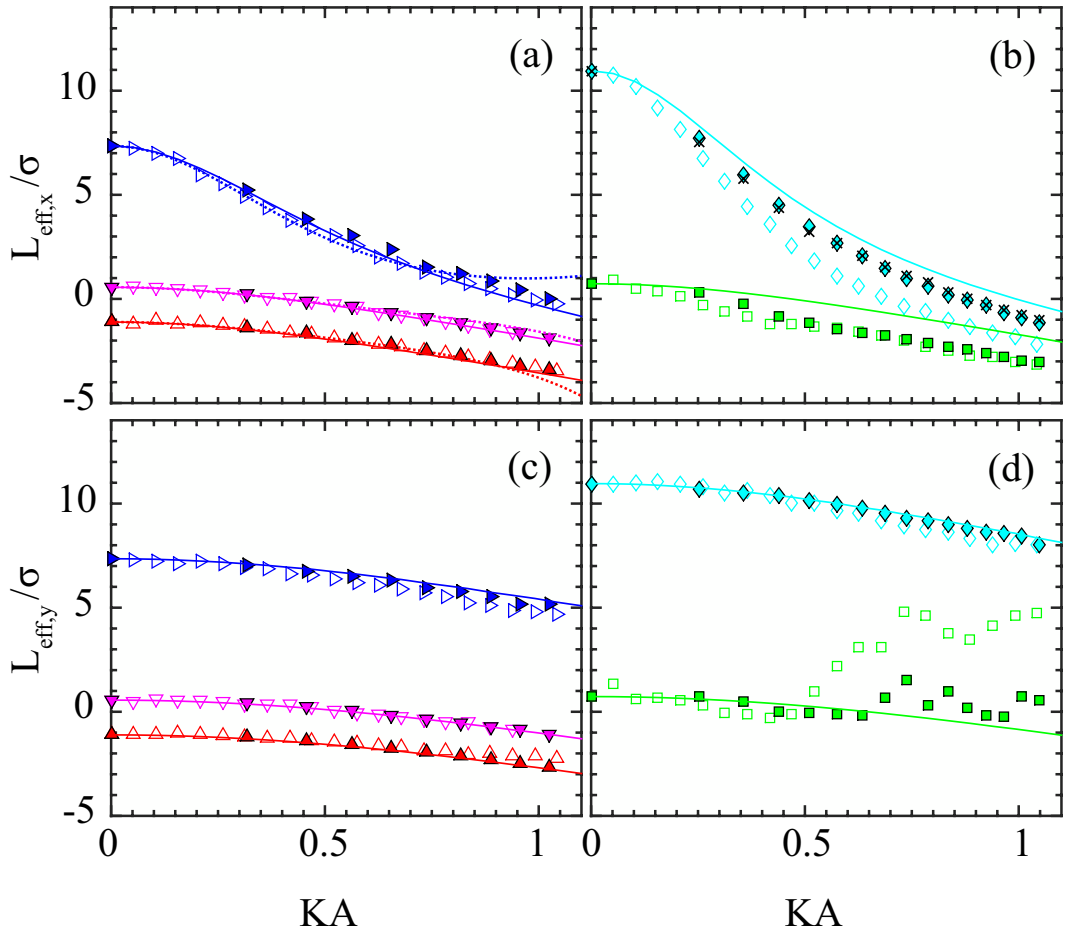

Figure 3.5: The top panels show the effective transverse slip length $L_{eff,x}$ as a function of normalized roughness amplitude KA for Type I (open symbols) and II (closed symbols) surfaces with (a) $a_0 = 1.2\sigma$ [triangles] and (b) $a_0 = 0.75\sigma$ [squares and diamonds]. Results for the different wall parameters in Table 3.1 are indicated by symbol color and orientation: A (downward magenta triangles), B (upward red triangles), C (right-pointed blue triangles), D (cyan diamonds), and E (green squares). The dotted colored lines show the analytical prediction of Eq. (3.11). The solid colored lines represent the results from continuum simulations with the same local boundary condition as for the corresponding flat surface. The black crosses in (b) show the results from the continuum simulations with a density-corrected locally varying slip length. The bottom panels show similar results for the longitudinal slip length $L_{eff,y}$ with (c) $a_0 = 1.2\sigma$ and (d) $a_0 = 0.75\sigma$.

(Table 3.1) yield three typical, but very different intrinsic boundary conditions at flat surfaces. Slip is pronounced for $\epsilon_{wf} = 0.00024\epsilon$ and $\sigma_{wf} = 2\sigma$, where $L_{s,0} = 7.33\sigma$. For a stronger wall-fluid LJ interaction, $\epsilon_{wf} = 0.4\epsilon$, $L_{s,0}$ drops to 0.56σ. The fitted velocity profile goes to zero in the region between the wall surface and the first fluid layer, indicating that there is little slip. When the interaction strength ϵ_{wf} is increased to 1.8ϵ, the first layer of fluid atoms becomes crystallized and locks into the wall potential minima. The locked first layer then further traps fluid atoms in the second layer through the fluid LJ interactions.[22] As a result, a negative slip length $L_{s,0} = -1.11\sigma$ is generated, corresponding to a stick boundary condition (also demonstrated in Figure 3.4).

Adding atomic roughness to these sparse surfaces produces very similar decreases in the slip length for Type I and II surfaces. For both transverse and longitudinal flows, these changes are nicely reproduced by numerical NS solutions that assume the local slip length remains equal to that on a flat surface. Moreover, the simpler analytical models described in Sec. 3.2.5 capture the trends in L_s. Indeed, the prediction of Panzer *et al.*[28,29] agrees with all simulations for $KA \lesssim 0.5$ and for almost the entire range of data for $\epsilon_{wf} = 0.4\epsilon$. Although not shown, Kamrin *et al.*'s predictions agree with the results at $\epsilon_{wf} = 0.4\epsilon$ and 1.8ϵ up to $KA \sim 0.4$, for both MD and continuum simulations.

In contrast, the results for close-packed surfaces ($a_0 = 0.75\sigma$) are different for walls of Type I and II and neither is consistent with continuum solutions with a constant

local slip boundary condition. For $\epsilon_{wf} = 0.4\epsilon$ (blue diamonds), a large slip length, $L_{s,0} = 10.96\sigma$, is measured for the flat surface. With increasing KA, Type II surfaces have systematically larger $L_{eff,x}$ than Type I. The numerical NS solutions yield even higher $L_{eff,x}$, particularly at large KA. Priezjev *et al.*[35] found a similar discrepancy in the same regime of high surface density and weak wall-fluid interactions.

Flat surfaces with $\epsilon_{wf} = 1.8\epsilon$ have a nearly no-slip boundary condition ($L_{s,0} \sim 0.7\sigma$) that is very similar to that for sparse surfaces with $\epsilon_{wf} = 0.4\epsilon$. Thus the continuum NS solutions for rough surfaces in Figure 3.5 are nearly the same. However roughness causes a much more rapid decrease in transverse slip length for dense surfaces. By $KA = 1$, both Type I and II dense surfaces have very negative values of $L_{eff,x}$ that are close to the results for sparse surfaces with $\epsilon_{wf} = 1.8\epsilon$. The deviations in longitudinal slip are even more dramatic. $L_{eff,y}$ first drops rapidly and then rises and oscillates. Note that for Type I surfaces $L_{eff,y}$ reaches up to $\sim 5\sigma$ which exceeds the amplitude of the corrugation.

The results for dense surfaces illustrate the kind of behavior that can occur whenever the curvature on rough surfaces changes the local slip boundary condition. The results for cylindrical surfaces in Chapter 2 (Ref. [176]) explain the nature of the changes and why they are stronger for sparse surfaces than dense surfaces in Figure 3.5. As noted above, the viscous coupling between fluid and solid is strongest when the wall potential produces strong density modulations in the first fluid layer. The fluid modulations are largest when the spacing between fluid atoms is comparable

to the spacing between minima in the potential from wall atoms. Any mismatch produces a more rapid drop in coupling for dense surfaces than sparse surfaces. The reason is that fluid atoms can fit more easily between atoms on sparse walls, so the magnitude of the corrugation in wall potential is larger.[176]

For Type II surfaces the spacing between wall atoms is fixed, but the spacing between potential minima changes with curvature because fluid atoms are at a different radius. For positive curvature the separation increases while for negative curvature the separation decreases. These changes are visible in the snapshots shown in Figures 3.2(b) and (c). The spacing between fluid atoms is larger near crests and smaller near troughs. Figure 3.6 shows the resulting variation in L_s with curvature for the sparse and dense surfaces with the largest slip lengths in Figure 3.5. The dense results are from Chapter 2 (Ref. [176]) and the sparse results were obtained in the same way using simulations of flow between concentric cylinders of constant curvature. The largest curvature, $0.26\sigma^{-1}$ is close to the curvature at the crest of sinusoidal surfaces with $KA \sim 1$. Note that L_s changes by an order of magnitude for the dense walls, but is relatively constant for sparse walls.

To show that these curvature effects can quantitatively account for changes in transverse slip over Type II surfaces we repeated the continuum NS calculations with varying local slip lengths. In all regions of positive curvature we used the linear fit to data shown in Figure 3.6. In convex regions of negative curvature we used the slip length for flat surfaces. While local slip is expected to be enhanced in these regions,[176]

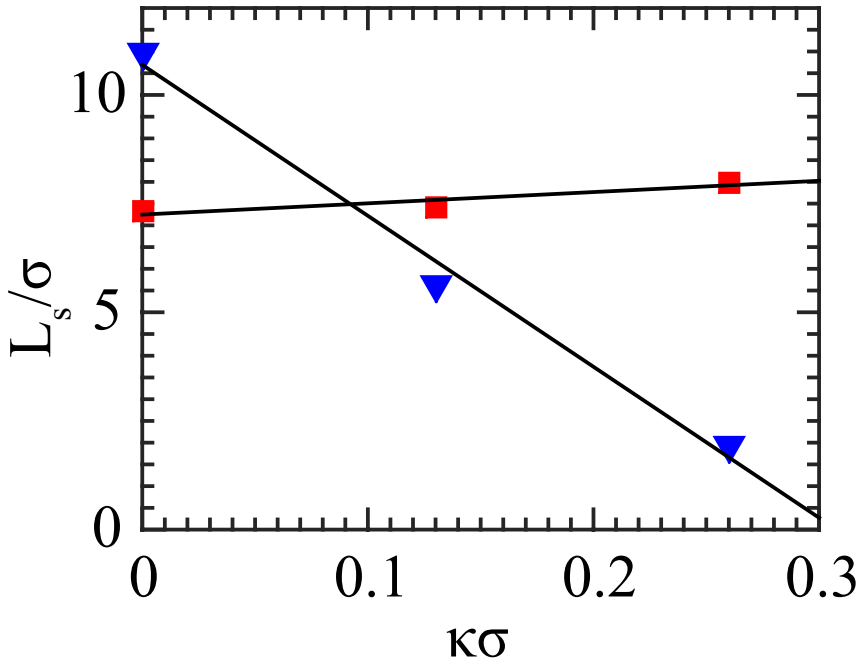

Figure 3.6: Results of cylindrical-geometry MD simulations for the behavior of the intrinsic slip length L_s with increasing curvature κ from 0 to $0.26/\sigma$. Results for two sets of wall parameters in Table 3.1 are indicated by symbol type: C (red squares) and D (blue triangles). The former data is reported in Appendix B of Chapter 2, while the latter were obtained in the same way using simulations of flow between concentric cylinders of constant curvature. The relation between L_s and κ is approximated by a linear fit, which is shown by the solid black lines.

flow is already strongly suppressed and changes in L_s have little effect. Moreover, calculation of L_s for large negative curvatures is impractical since it would involve Couette flow between two cylinders where the outer has a radius of only 3 atoms.

Solutions of the NS continuum equations for sparse surfaces with curvature corrected local slip lengths were nearly identical to those for a fixed length and are not shown in Figure 3.5(a). Variations in local slip do affect the continuum solution for dense walls and the crosses in Figure 3.5(b) track the atomistic results for Type II walls. Slip is even smaller for Type I walls because the atomic spacing in the transverse direction grows with the local slope. This further reduces the local slip length and thus the average effective slip length of the surface. Priezjev et al. also noted that this increase in spacing reduced the slip length and incorporated it in continuum simulations with a modified slip boundary condition that was uniform rather than a function of local slope and curvature.[35]

Curvature does not change the effective spacing between wall atoms along the longitudinal y direction. For the case considered here, the nearest-neighbor spacing and the reciprocal lattice vector $\vec{G}$ characterizing the density modulations are both along y. As a result there is little change in the local L_s for longitudinal flows at small KA. This explains why Type I and II walls have similar effective slip lengths that are both consistent with the NS solutions for constant local slip. If the lattice is rotated 45 degrees, the reciprocal lattice vectors have components along both transverse and longitudinal directions. Ref. [176] found that curvature then affected longitudinal

flow more than transverse flow. We do not present results for this case because the changes in local slip length are in between the ones showed in Figure 3.5.

For large KA the longitudinal slip length for strongly interacting sparse walls shows a sudden transition to new behavior. This reflects a transition in the structure of the first layer due to the strong change in local geometry produced by roughness. The strong change in the degree of epitaxial order is visible in Figure 3.6. The large wall-fluid interaction strongly attracts fluid atoms to the surface, leading to a pronounced layering (Figure 3.3). However, little lateral order can be seen within the first layer above the flat surface [Figure 3.2(a)]. This is because the small spacing of the wall potential minima makes it difficult for the fluid atoms to lock into epitaxial order.[22] The positive curvature near crests in Figures 3.2(b) and (c) leads to a larger spacing between minima in the potential from wall atoms and atoms in the first fluid layer align into lines going into the page. For Type I surfaces the spacing is also increased on sloped regions and there is a corresponding increase in alignment that is not seen on Type II surfaces.

The in-plane structure factor provides a more comprehensive and quantitative description of the changes in lateral order, but it can only be calculated for a large area with constant wall structure. To mimic the structure at the crest of the sinusoidal surface profile we create a flat surface with a rectangular structure. In one direction the nearest neighbor spacing is the constant longitudinal spacing $a_0 = 0.75\sigma$. The spacing in the other direction is increased to the value, 0.93σ, near a crest with

$KA = 0.75$. Similar results were obtained for cylindrical surfaces with the same spacings, so we expect the results to be representative of the local structure at wave crests.

Figure 3.7(a) shows the structure factor S_1 for the reference flat surface with a square lattice structure. Normalizing by N_1 gives a quantity that reaches unity for a perfect crystal at zero temperature. Only positive q_x and q_y are shown since the surface is symmetric about both axes. Two Bragg peaks are found at the shortest reciprocal vectors, $\vec{G}_{1,0}$ and $\vec{G}_{0,1}$. The heights are small (0.03) because the minima are too closely spaced for fluid atoms to lock into. The two higher peaks with magnitudes around 0.25 are associated with high-order commensurate phases that are a better match with the fluid spacing.[22] The first fluid layer has an intermediate viscous coupling to the wall, corresponding to a slip length close to zero.

Figure 3.7(b) presents $S_1(\vec{q})/N_1$ on a surface with wall atom spacing increased to 0.93σ along the x direction, reducing the symmetry from four-fold to two-fold. Because this increased spacing is close to the mean spacing between fluid atoms, there is strong epitaxial order reflected in large peaks at the first and second Bragg vectors. Indeed the height (0.82) of the first peak at $\vec{G}_{1,0}$ is above the value for bulk solids at the liquid/solid transition (~ 0.6). In contrast there are no visible peaks along q_y at $\vec{G}_{0,1}$ because the lattice spacing remains small. Instead there is a peak at a high-order commensurate structure with 16 fluid atoms per 21 wall atoms. This highly anisotropic structure leads to anisotropic slip boundary conditions. The

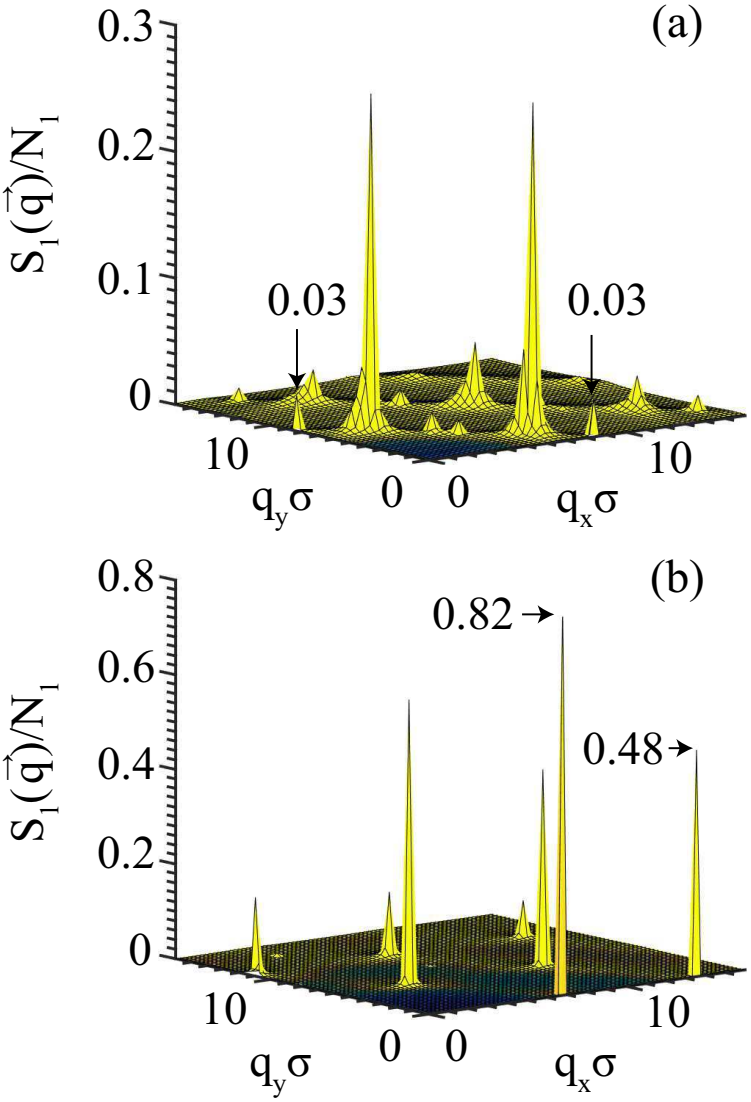

Figure 3.7: In-plane order as characterized by normalized structure factor $S_1(\vec{q})/N_1$ on flat surfaces where $a_0 = 0.75\sigma$ and $\epsilon_{wf} = 1.8\epsilon$. Panel (a) shows the results for the FCC (001) surface. In Panel (b), the surface is uniformly stretched along x, so that the lateral spacing along x is increased from 0.75σ to 0.93σ.

first fluid layer is locked to the lattice in the x direction and even the second layer feels a strong viscous drag. In contrast, the first layer slides even more easily in the y direction than for the square lattice. The slip length increases by an order of magnitude to about 5σ.

These changes in fluid structure explain the results for strongly interacting dense surfaces in Figures 3.5(b) and (d). The stretched spacing at the crest gives a strong reduction in local transverse slip length. The strong pinning of atoms at the crest inhibits sliding of the entire first layer. This lowers $L_{eff,x}$ relative to the continuum NS solution for $KA > 0.5$ and it approaches the solution for strongly interacting sparse surfaces that have a local stick boundary condition. The opposite effect occurs in the longitudinal direction. The sharp increase in the local longitudinal slip length at the crest leads to a rapid rise in Figure 3.5(d). The effect is largest for the Type I surfaces where the stretched spacing extends beyond the crest into regions where the surface slope is high. The high-order commensurate phases are sensitive to the exact degree of stretching, leading to fluctuations in the magnitude of the increase as KA rises.

3.3.2 Stepped Surfaces

Figure 3.8 presents the effective slip length on the stepped surfaces as a function of KA, for the x and y directions. The stepped surfaces are generated using sine waves with A increasing from 0 to 4σ in increments of 0.2σ. All atoms on lattice sites below the sine wave are removed. Because atoms lie at discrete positions, the total

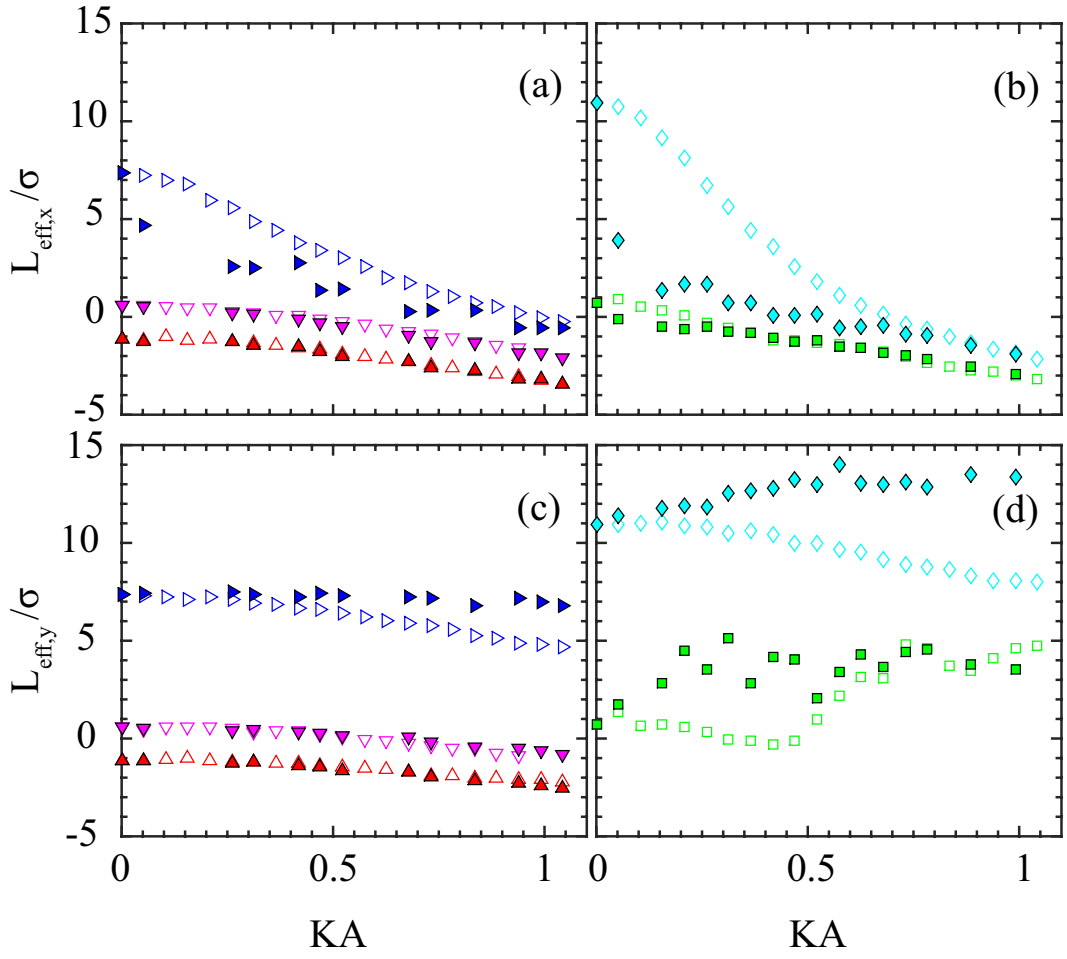

Figure 3.8: Panels (a) and (b) show the effective transverse slip length, $L_{eff,x}$, over the bent Type I (open symbols) and stepped Type III (closed symbols) surfaces with (a) $a_0 = 1.2\sigma$ and (b) 0.75σ as a function of the normalized amplitude KA. The various wall parameters from Table 3.1 are indicated by symbol color and orientation: A (downward magenta triangles), B (upward red triangles), C (right-pointed blue triangles), D (cyan diamonds), and E (green squares). Panels (c) and (d) show the effective longitudinal slip length, $L_{eff,y}$, for the surfaces in (a) and (b), respectively.

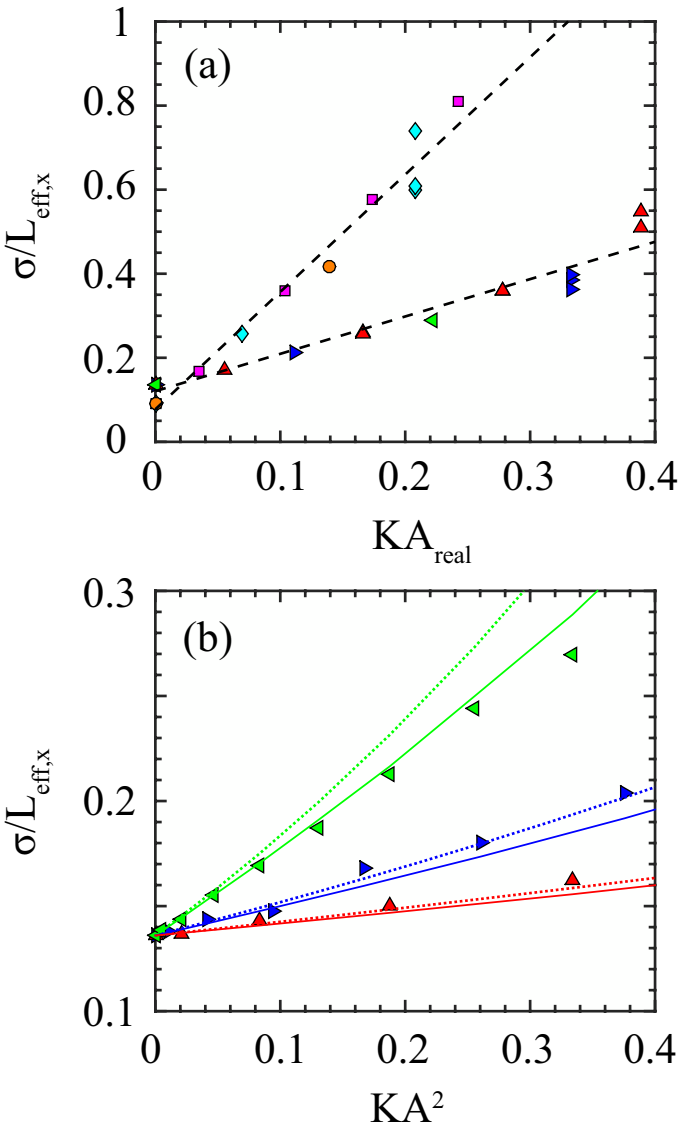

Figure 3.9: Panel (a) shows $\sigma/L_{eff,x}$ as a function of KA_{real}, where A_{real} is the total roughness amplitude of stepped surfaces, for three wavelengths: $\lambda_x = 12.04\sigma$ (left-pointed green triangles and orange circles), 24.08σ (right-pointed blue triangles and cyan diamonds) and 48.17σ (upward red triangles and magenta squares). Symbol type indicates the wall parameters from Table 3.1: C(triangles) and D (squares, diamonds and circles). Black dashed lines are linear fits to the data for each set of wall parameters. Panel (b) shows $\sigma/L_{eff,x}$ as a function of KA^2 for the sparse surface with Set D wall parameters from Table 3.1. The dotted colored lines show the analytical prediction of Eq. (3.11). The solid colored lines represent the results from continuum simulations with the same local boundary condition as for the corresponding flat surface.

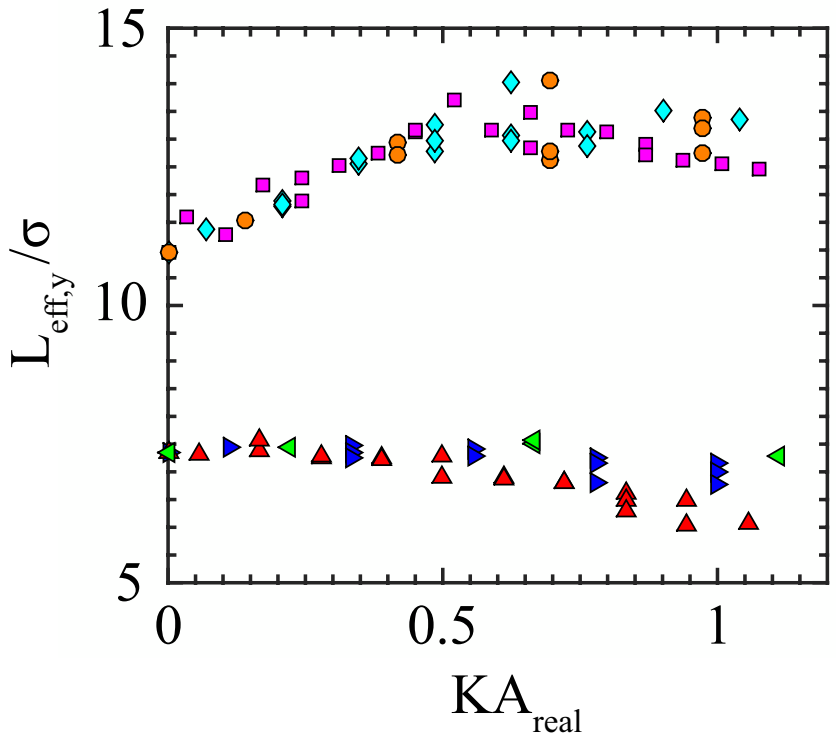

Figure 3.10: Effective longitudinal slip length $\sigma/L_{eff,y}$ as a function of KA_{real} for three wavelengths: $\lambda_x = 12.04\sigma$ (left-pointed green triangles and orange circles), 24.08σ (right-pointed blue triangles and cyan diamonds) and 48.17σ (upward red triangles and magenta squares). Symbol type indicates the wall parameters from Table 3.1: C(triangles) and D (squares, diamonds and circles). Black dashed lines are linear fits to the data for each set of wall parameters.

height variation has only a few discrete values and different amplitude sine waves can generate the same surface. In Figure 3.8 we use the smallest A that produces a given atomic configuration, and each point in Figure 3.8 corresponds to a different configuration. Results for the Type I bent surfaces are also presented for reference.

Surface steps have the most profound affect on flow in the transverse direction. The step edges trap fluid atoms in the adjacent layer, generating an additional drag force that dramatically reduces the local slip. As a result, $L_{eff,x}$ drops significantly for slippery surfaces with $L_{s,0} \gg \sigma$ [right-pointed triangles in Figure 3.8(a) and diamonds in (b)]. This effect is less noticeable for cases with nearly no slip or stick boundary conditions where the drag is already high when the surface is flat [downward and upward triangles in Figure 3.8(a) and squares in (b)].

For slippery surfaces, $L_{eff,x}$ decreases in a step-wise manner. Each step corresponds to an increase in the total height change along the surface. To facilitate comparison with bent surfaces, we define an amplitude $A_{real} = \Delta h/2$, where Δh is the height difference between the highest and lowest surface wall atoms. For the (001) surfaces considered here, $\Delta h = ma_0/\sqrt{2}$, where m is an integer and $a_0/\sqrt{2}$ is the spacing between lattice planes perpendicular to the surface. For $KA_{real} < 1$, the surface height changes in steps of $a_0/\sqrt{2}$, and if $\Delta h = ma_0/\sqrt{2}$ there are m steps up and m steps down per period. The discrete changes in $L_{eff,x}$ in Figures 3.8(a) and (b) correspond to changes in m, indicating that drag scales with the density of step edges.

Figure 3.9 shows a quantitative test of the contribution of step edges. For large slip lengths, the effective damping is inversely proportional to L_{eff}. Flat regions provide a background damping proportional to $\sigma/L_{s,0}$. The number of atomic steps per unit length is $2m/\lambda_x \propto KA_{real}$. Figure 3.9(a) shows that the drag rises linearly with KA_{real} with results for different λ_x collapsing onto a universal curve. Similar results were found for (111) surfaces and other wall interactions. Note that the slopes are different for sparse and dense surfaces, indicating that each step on a sparse surface produces less drag. We find that a number of factors may affect the drag from step edges. For Figure 3.9(a), the main factor is that the larger $\sigma_{wf} = 2\sigma$ for sparse surfaces rounds out the potential from the step edge. For the same interaction parameters, lowering the ratio of step height to the height of the first fluid layer reduces the drag. In all cases studied, the drag scaled linearly with KA_{real}.

This linear scaling is inconsistent with the analytical results for continuous surfaces [Eq. (3.11)]. There the damping rises as KA^2 as roughness rises from zero. Figure 3.9(b) verifies this scaling for Type I surfaces. Note that the detailed analytical theory [Eq. (3.11)] provides a good quantitative fit at small KA^2. The simpler approximation [Eq. (3.14)] predicts the correct linear dependence on KA^2, but not the change in slope with wavelength. The change in slope comes from terms in $KL_{s,0}$ in [Eq. (3.11)]. Our simulation results verify the analytic form of these terms for bent surfaces. Deviations from the asymptotic behavior become evident at smaller KA^2 as the wavelength decreases because curvature begins to affect the local slip boundary

condition.

Step edges have the opposite effect on longitudinal flow, tending to increase the slip length compared to bent surfaces. As shown in Figures 3.8(c) and (d), the effect is particularly pronounced for surfaces where the damping on flat surfaces is low, i.e. $L_{s,0}$ is high. For the two most slippery surfaces the slip length can be enhanced by $\sim 50\%$ at large KA.

We found that step-edges lowered the drag for longitudinal flow by changing the structure of the first fluid layer. Fluid atoms near step edges are ordered into parallel lines. This alignment propagates away from the edges, increasing density modulations in the transverse direction. In contrast, there is less order in the longitudinal direction. As noted above and in earlier work,[22,33,34,164,165,176] the slip length scales inversely with the degree of epitaxial order at Bragg vectors along the flow direction. Measurements of $S_1(\vec{G}_{0,1})/N_1$ show that the wall-induced Bragg peak along the longitudinal direction is decreased by step edges. For example, for $e_{wf} = 0.4\sigma$ and $a_0 = 0.75\sigma$ (diamonds) the peak in the first fluid layer above the lowest step may be reduced by 40%. There is a corresponding large increase in slip length for stepped surfaces relatively to bent surfaces. For the less slippery sparse case (squares) the reduction in Bragg peak is more dramatic because step edges hasten the transition to the ordered structure shown in Figure 3.7.

Figure 3.10 shows the longitudinal slip length for different wavelengths in systems with large intrinsic slip lengths, $L_{s,0}$. As for transverse slip, results for all wave-

lengths collapse when plotted against KA_{real}, indicating that slip only depends on the number of edges per unit length. Each edge induces local transverse order and lowers longitudinal order, leading to a rise in $L_{eff,y}$. Continuum theory predicts a very different scaling, with changes in slip varying as KA^2.

A new effect was observed at very large KA_{real}. Adjacent step edges form close-packed (111) planes. The intrinsic slip length on these planes is larger as noted previously by Soong *et al.*.[186] This decrease reflects the smaller spacing between minima in the wall potential, which reduces the degree of epitaxial locking in the adjacent fluid layer.[22,164,165,176]

3.4 Summary and Conclusions

We have used molecular dynamics simulations to study the effective slip boundary condition for simple fluid flow over rough surfaces in the Wenzel state. The wall roughness was modeled by a one-dimensional sine wave with wavelength much larger than the atomic diameter. The uncovered atomic effects may also apply to other types of rough surfaces, e.g., surfaces with small bumps.[40] The behavior of the effective slip length was examined by increasing the normalized corrugation amplitude up to $KA \sim 1$, for both the transverse and longitudinal directions. Different atomic configurations were investigated for strong and weak wall-fluid interactions, and high and low wall densities.

Increasing the roughness amplitude always reduces the transverse slip length,

$L_{eff,x}$. In most cases, it also decreases the longitudinal slip length, $L_{eff,y}$, but at a slower rate. However, in some cases $L_{eff,y}$ shows a remarkable increase above $L_{s,0}$. That is in stark contrast to continuum predictions. The resulting effective boundary condition is highly anisotropic.

The results for bent surfaces can be understood by supplementing continuum theory with an appropriate local boundary condition that depends on curvature and atomic spacing.[35,176] For sparse bent surfaces, curvature has little effect on the local slip boundary condition (Figure 3.6). For these surfaces the numerical solutions of the Navier-Stokes conditions with the flat surface slip length, $L_{s,0}$, provide a good description of the slip length at roughness amplitudes up to $KA = 1$. Simpler analytic approximations [Eq. (3.11)] remain accurate to $KA \sim 0.5$. The largest deviations are associated with changes in the spacing between surface atoms, which are present on Type I surfaces and eliminated for Type II surfaces.

Larger deviations from simple continuum theory are seen for dense bent surfaces. Previous work[176] and Figure 3.6 show that the local slip length on these surfaces is strongly dependent on curvature. For the chosen atomic orientation the curvature dependence is strong for transverse flow and negligible for longitudinal flow. As a result, the effect on the total transverse slip length is larger in Figure 3.5. Including the curvature dependent slip length in solutions of the Navier-Stokes equation captures the variation of the total effective slip length for Type II surfaces. For Type I surfaces the increase in atomic spacing on sloped surfaces produces an even greater

suppression of slip.

The most dramatic deviation from continuum theory for bent surfaces occurs for flow over strongly interacting Type I surfaces. The increase in atomic spacing along the transverse direction leads to anisotropic reconstruction of the first fluid layer. The layer becomes more strongly locked in the transverse direction leading to a lower slip length. However the order in the longitudinal direction decreases and there is a dramatic change from a stick boundary condition to a slip length that is larger than the amplitude of the roughness.

Steps lead to a qualitative change in the scaling of slip with surface roughness. There is a new contribution to drag from step edges that is independent of the slip on flat surfaces. Results for transverse flow at different wavelengths collapse when plotted against KA_{real} which is proportional to the density of step edges. This confirms that each edge adds an independent contribution to slip reduction. In contrast, results for bent surfaces show the scaling predicted by continuum theory, with drag rising as KA^2.

While steps suppress transverse slip, they enhance longitudinal slip. This was found to reflect alignment of fluid at step edges that suppressed longitudinal order. This contribution to changes in slip length also collapses when plotted against the step density at low KA_{real}. Different crystalline facets with higher or lower $L_{s,0}$ may form on rougher surfaces and lead to more complex behavior. For example, (111) facets (Figure 3.2) with a larger slip length formed on the roughest surfaces in Figure

3.8. Note that changes in the direction of the step edge along the surface will mix the effect of transverse and longitudinal regions. Since the drag enhancement due to transverse regions is larger, the net effect is likely to be a reduction in slip length.

We hope that the behavior revealed here will cast light on the behavior of realistic surfaces and facilitate the design of surfaces for various applications, e.g., drag reduction, flow control, and water harvesting. Real surfaces are likely to have more complex roughness with a range of wavelengths and orientations. Our results suggest that the resulting changes in slip will depend strongly on the atomic structure. The bent surfaces described here may represent vary long wavelength corrugations or rough amorphous surfaces. Such surfaces could be modeled with continuum theory using an appropriate local boundary condition determined for small surfaces of fixed curvature. The stepped surfaces studied here may be more representative of crystals. The results suggest that slip over such surfaces can be expressed in terms of the local slip length of faceted regions and an additional drag due to the density of step edges transverse to flow. This additional term is very sensitive to details of the atomic structure of the fluid and step edge, as well as the distribution of step edge angles.

Chapter 4

Multi-Scale Simulation Method for Electroosmotic Flows

4.1 Introduction

Electroosmotic transport in micro-and nano-channels has important applications in biological and engineering systems.[68–76] It allows convenient flow control and its efficiency scales more favorably with system size than the conventional pressure driven flow at micro-and nanoscales.

Generally speaking, a solid surface spontaneously becomes charged when in contact with an electrolytic solution, because of the differences in electrochemical properties between the two phases.[77,78] The released counterions are attracted to the surface, forming a region with excess charge that is referred to as the electrical double layer (EDL). Under an external electrical field in the direction along the surface, the fluid is dragged by the moving ions in the EDL, and thus an electroosmotic flow is generated.

The classical continuum approach, the Poisson-Boltzmann (PB) equation com-

bined with the Navier-Stokes (NS) equations, has been widely applied to predict electroosmotic transport.[77,79–88] However, discrete atomic effects become significant at the wall-fluid interface, and thus the continuum approximations break down.[89–94,187] For example, the ion distribution can be influenced by the strong electrostatic interactions and the finite size of the discrete ions and solvent molecules, and the transport properties of the fluid molecules can also be affected by their ordered structure near the surface. The influence on flow can be profound, because the electroosmotic driving force is mainly from the region very close to the surface where the charge concentration is highest.

Molecular dynamics is widely used to investigate processes at the atomistic level.[96,156,188,189] However, because of the high computational cost, the dimensions and the time scale of simulations are very limited. This limits their application to electroosmotic flow because the width of double layers and channels is typically much larger than atomic scales and typical flow rates are slow. In this chapter we address this challenge by developing an efficient hybrid multi-scale method for simulating electroosmotic flows at nanoscales.

In the last two decades, a variety of multi-scale hybrid schemes have been developed to simulate fluid dynamics problems. One important characteristic of these hybrid methods is that they aim to take advantage of both the efficiency of the continuum description and the accuracy of the molecular simulation by dynamically coupling them with each other. In general, there are two categories of methods

under the hybrid framework: domain-decomposition-based methods[97–117] and Euler-Lagrangian-decomposition-based methods.[118–132,190,191] The domain-decomposition-based methods are designed to accurately resolve the important atomistic details in a small region of the system, which is embedded into or coupled with a coarse-grained continuum fluid description. The Euler-Lagrangian methods are usually designed to simulate solute-solvent systems: the solute is modeled with the Lagrangian particle approach while the solvent is coarse-grained and simulated as a continuum fluid on a Eulerian mesh.

Our simulation method combines both types of hybrid scheme. In particular, the entire simulation domain is decomposed into the near-wall and bulk subdomains. Molecular dynamics is used in the near-wall subdomain where atomistic details are important, while the continuum incompressible fluctuating hydrodynamic equations are solved in the bulk region. The two descriptions are coupled in an overlap region. A discrete description of ions is retained in the continuum bulk region because of the low density of ions and the long-range of electrostatic interactions. A stochastic Euler-Lagrangian method (SELM) is used to simulate the dynamics of ions suspended in the implicit continuum solvent. The stochastic Euler-Lagrangian and molecular dynamics systems freely exchange charge in the middle of the overlap region. This hybrid approach is tested against full molecular dynamics simulations for different geometries and types of flows. In all cases, our method reproduces fully atomistic results.

The outline of this chapter is as follows. Section 4.2 describes the details of the different numerical models and how they are coupled in the hybrid scheme. In Section 4.3, the scheme is demonstrated through a number of benchmark simulations for various geometries and types of flows. A brief summary and concluding remarks are presented in Section 4.4.

4.2 Simulation Methods

4.2.1 Overview of the Hybrid Scheme

Figure 4.1 illustrates a typical geometry of our multi-scale hybrid simulations. A fluid flows through a channel bounded by two parallel solid walls. Following the idea of domain decomposition,[97,98,192] the whole system is decomposed into two particle (atomistic) subdomains near the top and bottom walls and a continuum subdomain covering the central bulk region. The simulations are periodic along the x and z directions with period L_x and L_z.

Molecular dynamics simulations are performed in the subdomains near walls to resolve the important atomic details at the wall-fluid interface. In the bulk subdomain, the fluid particles are coarsegrained to a continuum isothermal Newtonian fluid. Hydrodynamic thermal fluctuations naturally arise from this coarsegraining procedure.[193–196] At micro-and nanoscales, the thermal fluctuations may become important, especially in the transport and mixing of species.[196–200] To match with the molecular transport of the ions, we model the continuum fluid by the incompress-

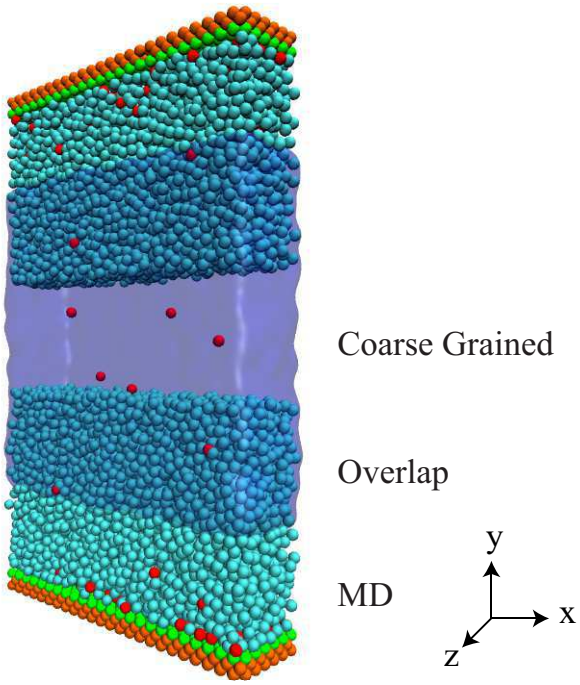

Figure 4.1: Sketch of a typical hybrid simulation system. The coarsegrained description is used in the middle region and molecular dynamics simulations are performed in both the upper and lower regions. Overlap regions are introduced to couple the different descriptions.

ible Navier-Stokes fluctuating hydrodynamic equations.[193–196, 201–207] In the examples considered in this study, we coarsegrain over the period in the z direction so the equations are two-dimensional, but this simplification is not necessary.

Following the hybrid method developed in Refs. [98–101], an overlap region is introduced at the interface between the MD and the continuum subdomains for the two descriptions to relax and couple with each other (Figures 4.1 and 4.2). The continuum hydrodynamics solver acquires boundary conditions from molecular dynamics at the lower edge of the overlap region (marked as $P \to C$), while at the other end of the overlap region (marked as $C \to P$) the MD simulation is constrained to follow the continuum solution.

For the charged systems in this study, a few ions exist in the bulk region far away from the walls and have a noticeable effect on the flow profile (see Section 4.3.5). Moreover, they may affect the distribution and dynamics of the ions near wall through the long-range electrostatic interaction and thus further influence the flow. The mean separation between these bulk ions ($\gtrsim 10$ atomic diameters) is comparable to the size of the overlap region. In order to replace them by a continuous average charge density the system would need to be coarse-grained to much larger volumes containing dozens or hundreds of ions. This would require atomistic simulations of much larger regions than is computationally practical. We therefore retain a discrete description of ions in the bulk subdomain. These ions are modeled as charged particles suspended in the underlying continuum fluid. A type of stochastic Eulerian-

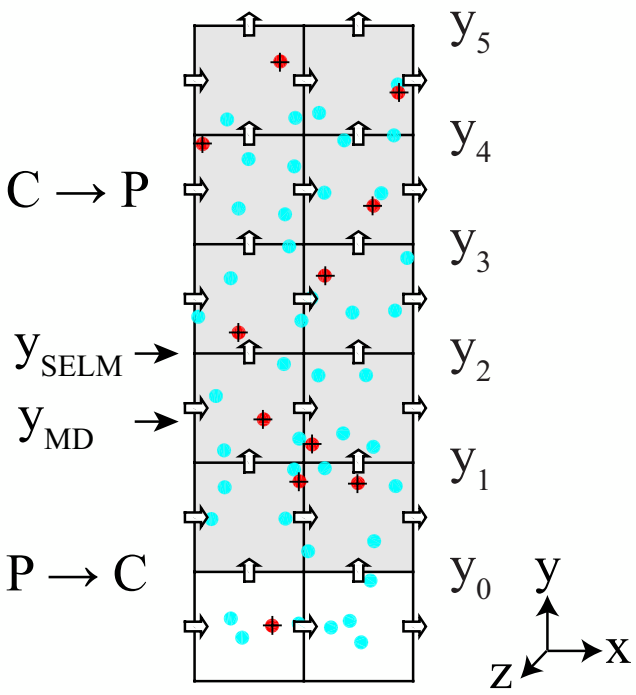

Figure 4.2: Detailed demonstration of the overlap region in the hybrid simulations. The molecular dynamics simulation is performed in the region below y_5, and the continuum fluid dynamics is simulated on the staggered mesh in the shaded region above y_0. Thus the overlap region spans over a width of 5 continuum cells in the y direction. The MD simulation is constrained by the continuum solutions in the $C \rightarrow P$ region. Correspondingly, the continuum fluid simulation acquires boundary conditions from MD results in the $P \rightarrow C$ region. The charges in the bulk continuum region is simulated by a stochastic Euler Lagrangian method. y_{SELM} and y_{MD} mark the transition zone where the SELM and MD simulations exchange charges.

Lagrangian method[124,132,190,205,207] is applied to simulate the dynamical processes of these discrete charges which is coupled with the fluctuating continuum background flow. The stochastic Eulerian-Lagrangian and molecular dynamics descriptions exchange charges in the middle of the overlap region. Special schemes are designed to ensure that the transitions of the charges between the two descriptions are smoothly performed with negligible artificial disturbance of the charge transport.

4.2.2 Particle Model 1: Molecular Dynamics

We use molecular dynamics to simulate fluid flow near the solid walls in the hybrid scheme. The same approach is also used in the full MD benchmark simulations, where MD simulation is conducted throughout the entire system.

The MD subdomain contains a rigid atomic solid wall and a fluid that consists of simple spherical particles with (ion) and without (solvent) charge (Figure 4.1). The van der Waals interactions between fluid particles are modeled by a truncated Lennard-Jones (LJ) potential:

$$\Psi_{LJ}(r) = 4\epsilon[(\frac{\sigma}{r})^{12} - (\frac{\sigma}{r})^{6} - (\frac{\sigma}{r_c})^{12} + (\frac{\sigma}{r_c})^{6}],\ for\ r < r_c \tag{4.1}$$

where r is the distance between the two particles, and ϵ and σ define the characteristic energy and length scales of the fluid, respectively. Ψ_{LJ} is truncated at a distance $r_c = 2.2\sigma$ to save computational cost, and shifted so that $\Psi_{LJ}(r_c) = 0$. The van der Waals interactions between wall (w) and fluid (f) particles are also modeled by a truncated LJ potential with parameters $\epsilon_{wf} = 0.6\epsilon$, $\sigma_{wf} = 1\sigma$ and $r_{c,wf} = 2.2\sigma$.

Each fluid particle has a mass m. Fluid temperature is maintained at $T = 1.1\epsilon/k_B$ by imposing a Langevin thermostat in the flow-irrelevant z direction.[97,137] If not mentioned otherwise, the equations of motion for a fluid particle are:

$$m\ddot{x} = -\partial\Psi(\boldsymbol{r})/\partial x, \tag{4.2}$$

$$m\ddot{y} = -\partial\Psi(\boldsymbol{r})/\partial y, \tag{4.3}$$

$$m\ddot{z} = -\partial\Psi(\boldsymbol{r})/\partial z - \Gamma_{thm}u_z + \sqrt{2\Gamma_{thm}k_BT}R(t). \tag{4.4}$$

Here $\Psi(\boldsymbol{r})$, $\boldsymbol{r} = (x, y, z)$ and $\boldsymbol{u} = (u_x, u_y, u_z)$ represent the total potential energy, and the position and velocity of the particle, respectively. The last two terms in Eq. (4.4) arise from the thermostat, where the damping rate Γ_{thm} controls the heat flux between the system and the heat bath and $R(t)$ is a random force sampled from a Gaussian distribution with zero mean and unit variance. We use a damping rate $\Gamma_{thm} = 1m\tau^{-1}$, where $\tau = \sigma\sqrt{m/\epsilon}$ is the characteristic time scale of the Lennard-Jones potential. This provides effective temperature control without substantially disturbing the motion of the particles.[22,23,35,97–100,102] The bulk density of fluid is fixed at $\rho = 0.81m\sigma^{-3}$, and the bulk shear viscosity at this state is $\mu = 2.14\epsilon\tau\sigma^{-3}$.[97,101]

The planar wall consists of three (001) layers of a FCC crystal and the x axis is aligned with the [100] vector of the FCC lattice. The nominal position of the wall surfaces is defined to coincide with the center of the wall atoms in the layer closest to the fluid. The wall atoms are fixed at their equilibrium positions, and the distance

between nearest neighbor atoms is $a = 1.00\sigma$.

For an ionic solution, each ion is modeled as a fluid particle that has a unit charge e (where $e = 1.6^{-19}C$ is the electron charge). All solid atoms in the surface layer of the wall (closest to the fluid) are assigned a small uniform countercharge to ensure that the whole system is electrically neutral. The electrostatic interaction between charges q_i and q_j is given by Coulomb's law,

$$\Psi_C(r) = \frac{q_i q_j}{4\pi\epsilon_0\epsilon_r r}, \tag{4.5}$$

where ϵ_0 is the vacuum permittivity and ϵ_r is the dielectric constant. The relative strength of electrostatic interactions can be characterized by the Bjerrum length $\lambda_B = e^2/4\pi\epsilon_0\epsilon_r k_B T$, the separation at which Coulomb interactions equal the thermal energy. Increasing ϵ_r reduces both the strength of the Coulomb interactions and the Bjerrum length. If not mentioned elsewhere, we set $\lambda_B = 2.55\sigma$. When the mean distance between the charges is much larger than λ_B, correlations between particles are unimportant and the Poisson-Boltzman equations are accurate. This situation is referred to as the low concentration (or dilute) limit in this study.

The long-range Coulomb interactions between charges are calculated by a multi-grid particle-particle particle-mesh (PPPM) algorithm.[208] The Coulomb forces on a charge exerted by the other charges within a given cutoff distance, $r_{c,C}$, are calculated pair by pair with Eq. (4.5). This cutoff distance should be differentiated with the cutoff distance of the LJ potential, and it is set to be $r_{c,C} = 8\sigma$ in our simulations giv-

ing a good balance between accuracy and computational efficiency. The interactions beyond this cutoff distance are calculated by solving a global Poisson equation for the potential field. The Poisson equation is solved by an efficient multigrid method on a three-dimensional uniform mesh with periodic boundary conditions.[208] This mesh covers the whole simulation domain. The cell size is taken around σ to ensure accuracy, which is determined by the characteristic inter-charge distance at the wall. To deal with the non-periodic boundary conditions in the y dimension, the mesh is extended in the y direction to create an empty space of the same size as the simulation channel. Then a periodic boundary condition is imposed but the effect of the periodic images is removed by applying an additional electric field in the y direction.[209] This is taken to be minus the total dipole moment of the whole system divided by the total volume of the meshed space. We refer to Ref. [208] for further details of the multigrid PPPM method.

It is important to note that, due to the long range nature of the Coulomb potential, each charge interacts with all the other charges throughout the whole system. The subroutine to calculate the electrostatic potential involves looping over all the charges throughout the whole simulation domain, with both MD and SELM descriptions (see Section 4.2.3). In a simulation, this subroutine is performed over all the charges for both of the descriptions every MD time step after their positions are updated.

The equations of motion are integrated using the velocity-Verlet algorithm with a time step $\Delta t_{MD} = 0.005\tau$. The integration procedure from time t to $t + \Delta t_{MD}$ can

be described as follows:

1. Update the particle position from t to $t + \Delta t_{MD}$,

$$\boldsymbol{r}(t + \Delta t_{MD}) = \boldsymbol{r}(t) + \boldsymbol{u}(t + \frac{\Delta t_{MD}}{2})\Delta t_{MD}; \tag{4.6}$$

2. Update the force on the particle, $\boldsymbol{f}$, to the new time step $t + \Delta t_{MD}$;

3. Propagate the particle velocity from $t + \Delta t_{MD}/2$ to $t + \Delta t_{MD}$,

$$\boldsymbol{u}(t + \Delta t_{MD}) = \boldsymbol{u}(t + \frac{\Delta t_{MD}}{2}) + \frac{\Delta t_{MD}}{2m}\boldsymbol{f}(t + \Delta t_{MD}); \tag{4.7}$$

4. Propagate the velocity of the particle for half a time step more to $t + \frac{3\Delta t_{MD}}{2}$,

$$\boldsymbol{u}(t + \frac{3\Delta t_{MD}}{2}) = \boldsymbol{u}(t + \Delta t_{MD}) + \frac{\Delta t_{MD}}{2m}\boldsymbol{f}(t + \Delta t_{MD}). \tag{4.8}$$

4.2.3 Particle Model 2: Particles of Stochastic Eulerian Lagrangian Simulations

In the bulk region, the discrete ions are modeled as Lagrangian points with a unit charge embedded in the implicit fluid which is described by the equations of continuum Navier-Stokes fluctuating hydrodynamics [see Eqs. (4.21) and (4.22)].

The classical Langevin equation is a simple but widely applicable approach to describe the diffusive dynamics of small Lagrangian objects suspended in an implicit viscous fluid at or near equilibrium.[210–212] It phenomenologically models the total force on an object from the solvent by a summation of a Stokes-type dissipative

friction term and a stochastic noise term:

$$\boldsymbol{f}_f = -\Gamma \boldsymbol{u} + \sqrt{2\Gamma k_B T}\boldsymbol{R}(t). \tag{4.9}$$

The first term on the right-hand side models the effective drag from the viscous fluid, where Γ is the friction coefficient and $\boldsymbol{u}$ is velocity of the object. The second term mimics the random collisions associated with the thermal motions of the solvent molecules where $\boldsymbol{R}(t)$ is taken to be a Gaussian process with zero mean and δ-correlations, i.e.,

$$< R_i(t)R_j(t') >= \delta_{ij}\delta(t-t'), \tag{4.10}$$

where i and j denote Cartesian components, δ_{ij} is the Kronecker delta, and $\delta(t-t')$ is the Dirac delta function. With the amplitude $\sqrt{2\Gamma k_B T}$, the stochastic force term balances the energy dissipated by the friction term so that the fluctuation dissipation theorem for the system is satisfied. Comparing to full MD simulations, the computational cost is reduced significantly, since the degrees of freedom of the whole solvent are eliminated and only the trajectories of the small number of objects are tracked. Eq. (4.9) is also widely used in MD simulations as an efficient and effective thermostat method [as implemented in Eq. (4.4)] by choosing a sufficiently weak friction coefficient to avoid substantial perturbations to the particle trajectories.[22,137,164,213]

Eq. (4.9) does not include the hydrodynamics of the background fluid. Thus, it does not apply to systems with nonzero background fluid flow, and fails to capture the long time tail of the velocity autocorrelation function in suspensions which can

affect the modeling of diffusion.

Hydrodynamic effects can be incorporated by a simple modification to Eq. (4.9). As proposed by Ahlrichs and Dünweg,[124,190] the friction force on a particle exerted by the fluid is assumed to be proportional to the particle's relative velocity with respect to the local fluid, so that

$$\boldsymbol{f}_f = -\Gamma_{bare}[\boldsymbol{u} - \boldsymbol{U}_{ref}(\boldsymbol{r})] + \sqrt{2\Gamma_{bare}k_BT}\boldsymbol{R}(t), \tag{4.11}$$

where $\boldsymbol{U}_{ref}(\boldsymbol{r})$ is the local reference velocity interpolated from the spatially discretized flow field of the continuum fluid to the position of the particle $\boldsymbol{r}$. Γ_{bare} is referred to as the bare friction coefficient. Based on linear response theory, Eq. (4.11) produces an effective relaxation process for the particle velocity to relax to the local fluid velocity, where the relaxation time scale is controlled by the particle mass and the bare friction coefficient $\sim m/\Gamma_{bare}$. Meanwhile, a two-way particle-fluid coupling can be achieved by passing the force on the particle back to the local continuum fluid.

A hybrid approach of this type coupling molecular dynamics of moving particles with fluctuating Lattice-Boltzmann equations (so called hybrid MD/LB method) was introduced in Refs. [124, 190]. It has been applied to simulate polymers in dilute solutions,[118,119,124–127,190,214] charged colloidal systems[128–131,191] and electro-osmotic flows.[132] Recently the same coupling strategy was applied to couple MD simulations of particles with equations of Navier-Stokes fluctuating hydrodynamics to simulate polymers and macromolecules suspended in implicit solvents.[120,121,206,207,215]

In this study we adopt the same methodology to couple the discrete ions with the implicit background fluid which is described by the Navier-Stokes fluctuating hydrodynamics [see Eqs. (4.21) and (4.22)]. We want to note that although there are subtle differences in the implementation details, e.g., evaluating the reference flow velocity, transferring force back to the continuum fluid, particle interaction potentials and the governing equations for the implicit fluid, etc., all the above mentioned schemes follow the same principle methodology: using the stochastic Langevin-type equation, i.e., Eq. (4.11), to couple the Lagrangian molecular dynamics of moving particles locally with a continuum thermally fluctuating fluid flow field which is solved on Eulerian mesh grids. Following the terminology in Ref. [206], we refer to this general category of schemes as Stochastic Eulerian Lagrangian Methods (SELM).

In our simulations, the local reference velocity of the background flow field, $\boldsymbol{U}_{ref}(\boldsymbol{r})$, is interpolated from the solutions of the continuum hydrodynamic equations which are discretized on the underlying staggered grid (as illustrated in Figure 4.2). Since our continuum hydrodynamic equations [Eqs. (4.21) and (4.22)] are two-dimensional, the z-direction velocity $U_{ref,z}$ is taken to be zero.

We use Peskin's interpolation scheme which is widely used in the Immersed Boundary Method (IBM).[123,202,203,214,216,217] For example, the interpolation operation for the x component of velocity $U_{x,ref}(\boldsymbol{r})$ can be written as

$$U_{x,ref}(\boldsymbol{r}) = \sum_{\boldsymbol{r}_{grid}} \Phi_h(\boldsymbol{r} - \boldsymbol{r}_{grid}) U_x(\boldsymbol{r} - \boldsymbol{r}_{grid}), \tag{4.12}$$

where h represents the mesh size and $U_x(\boldsymbol{r}-\boldsymbol{r}_{grid})$ denotes the discretized continuum solution defined at position $\boldsymbol{r}_{grid}$. The weighting function $\Phi_h(\boldsymbol{r})$ can be further written as a product of 1-dimensional kernel functions for each space dimension:

$$\Phi_h(x,y) = \phi(\frac{x}{h})\phi(\frac{y}{h}), \tag{4.13}$$

where the 1-dimensional kernel function $\phi(x)$ is given by

$$\phi(x) = \begin{cases} \frac{1}{3}(1+\sqrt{-3x^2+1}) & |x| < 0.5 \\ \frac{1}{6}(5-3|x|-\sqrt{-3(1-|x|)^2+1}) & 0.5 \le |x| \le 1.5 \\ 0 & otherwise. \end{cases} \tag{4.14}$$

The kernel is constructed to fulfill the following requirements:

1. $\phi(x)$ is continuous for all real numbers;

2. $\phi(x) = 0$ for $|x| \ge 1.5$;

3. $\sum\limits_i \phi(x-i) = 1$ for $\forall x$;

4. $\sum\limits_i (x-i)\phi(x-i) = 0$ for $\forall x$;

5. $\sum\limits_i \phi^2(x-i) = 1/2$ for $\forall x$,

where $\sum\limits_i$ denotes a summation over the all integers i. However, the requirement 2 ensures that 1-dimensional interpolating operation along a single space dimension only involves 3 nearest mesh-defined points. Thus for the two-dimensional mesh in our simulations, each particle interacts with the $3\times 3 = 9$ nearest mesh-defined points.

An additional important property of the kernel function $\phi(x)$ is that its first order derivative is also continuous throughout the entire domain of x. This guarantees that the interpolated reference velocity varies smoothly with a continuous spatial derivative as the particle moves through the underlying mesh grid.

Another possible choice for $\phi(x)$ is the simple 2-point linear interpolation function.[118–121,124–132,190,191,218] However, this function does not have a continuous derivative and thus deteriorates the smoothness of the interpolated reference velocity. It was shown by Dünweg and Ladd[217] that the linear interpolation scheme may lead to a variation in the local effective mobility of the Lagrangian particle as it moves through the underlying grid.

The resulting equations of motion of the ions in the continuum bulk subdomain are given by

$$m\ddot{\boldsymbol{r}} = -\nabla\Psi(\boldsymbol{r}) - \Gamma_{bare}[\boldsymbol{u} - \boldsymbol{U}_{ref}(\boldsymbol{r})] + \sqrt{2\Gamma_{bare}k_BT}\boldsymbol{R}(t). \tag{4.15}$$

In general, $\Psi(\boldsymbol{r})$ represents the total potential, arising from both the pairwise interactions and external force fields. It can be calculated by employing the same techniques that are developed for MD simulations. In the case of our simulations, because the ions are modeled as point charges, $\Psi(\boldsymbol{r})$ solely equals the total electrostatic potential energy of the charge, in which the contribution from the long range Coulomb interactions is calculated by the same multigrid PPPM method as in the MD simulations (see Section 4.2.2).

The input value of Γ_{bare} is determined from equilibrium simulations of bulk fluid systems, where Γ_{bare} is tuned to match the diffusion coefficient of the SELM particles to that of the full MD simulations,[124,190,206,207,217] so that the long time scale dynamics is consistent between the two descriptions (see Section 4.2.3). Generally speaking, for a dilute system with periodic boundary conditions, the diffusion coefficient of the SELM particles can be written in the form

$$D = \frac{k_B T}{\Gamma_{bare}} + f_\Phi, \tag{4.16}$$

where f_Φ is a general function that includes the effects from the interpolation scheme for the reference velocity, the geometrical properties of the underlying Eulerian mesh cells, properties of the fluid and the size of the system.[124,190,206,217]

We track the time evolution of the trajectories for all the SELM charges by numerically integrating Eq. (4.15) with the Brünger-Brooks-Karplus (BBK) method.[219] The integration procedure from time t by a time step Δt to $t + \Delta t$ is as follows:

1. Update the particle position from t to $t + \Delta t$,

$$\boldsymbol{r}(t + \Delta t) = \boldsymbol{r}(t) + \boldsymbol{u}(t + \frac{\Delta t}{2})\Delta t; \tag{4.17}$$

2. Update the potential force, reference velocity, and the random force to $t + \Delta t$;

3. Propagate the particle velocity from $t + \Delta t/2$ to $t + \Delta t$,

$$\begin{aligned}\boldsymbol{u}(t+\Delta t) = \frac{1}{(1+\frac{\Gamma_{bare}\Delta t}{2})}\{\boldsymbol{u}(t+\frac{\Delta t}{2}) \\ + \frac{\Delta t}{2m}[-\nabla\Psi(\boldsymbol{r}(t+\Delta t)) + \Gamma_{bare}\boldsymbol{U}_{ref}(\boldsymbol{r}(t+\Delta t)) + \boldsymbol{f}_R(t+\Delta t)]\}.\end{aligned} \tag{4.18}$$

4. Propagate the velocity of the particle for half a time step more to $t + \frac{3\Delta t}{2}$,

$$\begin{aligned}\boldsymbol{u}(t+\frac{3\Delta t}{2}) = (1-\frac{\Gamma_{bare}\Delta t}{2})\boldsymbol{u}(t+\Delta t) \\ + \frac{\Delta t}{2m}[-\nabla\Psi(\boldsymbol{r}(t+\Delta t)) + \Gamma_{bare}\boldsymbol{U}_{ref}(\boldsymbol{r}(t+\Delta t)) + \boldsymbol{f}_R(t+\Delta t)].\end{aligned} \tag{4.19}$$

Here $\boldsymbol{f}_R(t)$ represents the temporally discretized form of the random force term (the last term in 4.15) with its components being independent Gaussian random numbers with zero mean and variance of $\sqrt{2\Gamma_{bare}k_BT/\Delta t}$. In the limit of $\Gamma_{bare} \to 0$, this integrator reduces to the velocity Verlet scheme [Eqs. (4.6), (4.7) and (4.8)]. With this algorithm, the equations of motion of the SELM charges are integrated concurrently with the molecular dynamics simulations with the same time step Δt_{MD}.

After each time step of integration, the electrostatic force exerted on each SELM charge is spread back to the associated grid position on the Eulerian mesh where U_{ref} is interpolated from. This grid-based spread force field is further averaged over every particle-continuum time-coupling interval Δt_{cp}, and fed into the continuum fluid solver as the additional volumetric force term F_{ad} [see Eq. (4.21)]. As a result, the two-way Lagrangian-Eulerian particle-fluid coupling is achieved. Based on the same interpolation scheme [Eqs. (4.12), (4.13) and (4.14)], the spreading weight function for a particle at r with respect to a grid position $\boldsymbol{r}_{grid}$ is taken to be $\Phi_h(\boldsymbol{r} - \boldsymbol{r}_{grid})/V_h$,

where $V_h = h^2 L_z$ is the effective physical volume of a Eulerian mesh cell (see Section 4.2.4).

In previous studies,[118–121, 124–132, 190, 191, 207, 214, 215, 218] repulsive Lennard-Jones interactions (given by Eq. (4.5) with a short cutoff radius $r_c = 2^{1/6}\sigma$) were added in order to include the finite size of the particles. We verified through simulations that adding repulsive Lennard-Jones potential into $\Psi(\boldsymbol{r})$ produces indistinguishable results. This is because the same-sign charges are dilute and well separated from each other by the repulsive electrostatic forces, so that the average inter-charge distance ($\sim 10\sigma$) is far beyond the range of the Lennard-Jones interactions and makes the particle size effects negligible.

Previous studies also use very small grid size, down to the atomic radius, to resolve the flow between the particles. Thus the saving in the computational cost was limited. That is not necessary in our cases. Because of the large inter-charge distance, we can use a larger grid size h. The atomic details and the small scale flows surrounding a charge are not resolved, but coarsegrained by the linear response coupling model [Eq. (4.11)].

The effective volume V_f of the local fluid coupled with each charge through this interpolation and spreading coupling scheme can be estimated as

$$V_f = L_z h^2 / \sum_{\boldsymbol{r}_{grid}} \Phi_h^2(\boldsymbol{r} - \boldsymbol{r}_{grid}) = 4h^2 L_z. \tag{4.20}$$

We have also tested other choices for the force spreading from the particle to fluid that

were used in previous works, i.e., the whole Langevin type force $-\boldsymbol{f}_f$[120,121,128,207] and solely the friction force term $\Gamma_{bare}(\boldsymbol{u}-\boldsymbol{U}_{ref}(\boldsymbol{r}))$.[124,125,190] The choice of force spreading did not affect the results for either the diffusion of charges or the electroosmotic flows. This is because the momentum relaxation time of the charges (given by $m/\Gamma_{bare} \sim 0.1\tau$) is much shorter than the characteristic hydrodynamic time scales of the local fluid, given by $\rho h^2/\mu \sim 5\tau$. The fluid only feels the mean effective drag force from each charge, while the mean effective drag on the charge from the fluid is balanced by the mean electrostatic force.

It is important to note that, in the hybrid simulations, the charges of both the molecular dynamics and the stochastic Eulerian Lagrangian simulations can exist in the MD-continuum overlap region (see Section 4.2.6). In order to resolve the fluid flow correctly, one should include the driving forces from all the charges within the whole corresponding region. Thus, the electrostatic forces exerted on the MD charges in the overlap region are also passed to the continuum fluid equation Eq. (4.21) with the same spreading scheme. This also applies for the molecular dynamics system. The electrostatic forces on the SELM charges within the overlap region are also transfered to the nearest neutral MD fluid particles to drive the MD system. We find that this force transfer can produce accurate results at hydrodynamic time and length scales, as long as the charges are dilute in the corresponding region such that mean inter-charge distance is longer than both the Bjerrum length and the range of the Lennard-Jones interaction.

4.2.4 Continuum Fluid Model: Incompressible Navier-Stokes Fluctuating Hydrodynamics

In the bulk subdomain, the fluid particles are coarsegrained to a continuum Newtonian fluid. The fluid flow is described by two-dimensional incompressible Navier-Stokes fluctuating hydrodynamics (ICNSFH) at a constant temperature:[201]

$$\rho(\partial t\boldsymbol{U} + \boldsymbol{U}\cdot\nabla\boldsymbol{U}) = -\nabla P + \mu\nabla^2\boldsymbol{U} + \nabla\cdot[(2k_BT\mu)^{1/2}\widetilde{\boldsymbol{W}}] + \boldsymbol{F}_{ad} \tag{4.21}$$

$$\nabla\cdot\boldsymbol{U} = 0, \tag{4.22}$$

where U and P denote the velocity and the non-thermodynamic pressure, respectively. The density ρ, shear viscosity μ and temperature T are constant and set to match the molecular dynamics simulations. $\boldsymbol{F}_{ad}$ represents the additional driving force which arises from the force exerted by the suspended particles (see Section 4.2.3) or an external force field (e.g., gravity force). $(2k_BT\mu)^{1/2}\widetilde{\boldsymbol{W}}$ designates the stochastic momentum flux that is assumed to be a symmetric white noise random tensor field. $\widetilde{\boldsymbol{W}}$ is a symmetric Gaussian random tensor with

$$< \widetilde{W}_{ij} >= 0, \tag{4.23}$$

$$< \widetilde{W}_{ij}(\boldsymbol{r},t)\widetilde{W}_{kl}(\boldsymbol{r}',t') >= (\delta_{ik}\delta_{jl} + \delta_{il}\delta_{jk})\delta(t-t')\delta(\boldsymbol{r}-\boldsymbol{r}'), \tag{4.24}$$

where $<\cdot>$ represents the ensemble average, and i, j, k and l denote Cartesian com-

ponents. This form of the stochastic forcing term fulfills the fluctuation-dissipation relation between the thermal noise and the viscous dissipation.[201,206,220] Thus, it ensures that the thermally induced velocity fluctuations are correctly reproduced.

It is worthwhile to note that for the interpretations of all the stochastic differential equations in this work [i.e., Eqs. (4.4),(4.15) and (4.21)],there is no difference between the Itô and Stratonovich representation,[201,211,221] given that all the stochastic forcing terms are additive.

An issue with Eq. (4.21) is that it is mathematically ill-defined. Because of the stochastic white noise force field, the velocities cannot be interpreted as continuous functions. Thus, the point-wise interpretation of the nonlinear term, $\boldsymbol{U} \cdot \nabla \boldsymbol{U}$, becomes problematic. One way to deal with this problem is to introduce regularization (smoothing) at small scales.[201,206,222–225] This kind of regularization is naturally performed when Eqs. (4.21) and (4.22) are interpreted in the context of the finite volume method. The hydrodynamic equations can be interpreted as coarsegrained from molecular dynamics descriptions where the hydrodynamic quantities are interpreted as the mean molecular properties that are averaged within the underlying mesh cells. In this way, the irregularities in the solutions are removed, as long as the mesh cell is large enough to include a sufficient number of fluid particles.

The equations of the Navier-Stokes fluctuating hydrodynamics are discretized onto a uniform staggered grid (as illustrated in 4.2) using a second-order accurate scheme developed by Balboa *et al.*[201] The grid size is taken to be $h \times h = 3.4\sigma \times 3.4\sigma$.

It is important to note that although equations for the fluid flow [Eqs. (4.21) and (4.22)] are two-dimensional, all the associated quantities are interpreted as the mean molecular quantities averaged within three-dimensional control cells with physical volume $h \times h \times L_z$. This ensures a consistency with the three-dimensional nature of the molecular dynamics simulations. A full three-dimensional implementation of the flow field could be used if needed.

The pressure P is defined at the centers of the cells. The x components of the velocity and the additional force, i.e., U_x and $F_{ad,x}$, are defined at the middle of the vertical (rightward arrows) edges of the cells, while the corresponding y components, i.e., U_y and $F_{ad,y}$, are defined at the middle of the horizontal (upward arrows) edges. The discretized (both spatially and temporally) form of the stochastic momentum flux term becomes

$$(2k_BT\mu)^{1/2}\widetilde{\boldsymbol{W}} \rightarrow (\frac{2k_BT\mu}{V_h\Delta t_{NS}})^{1/2}\boldsymbol{W}, \tag{4.25}$$

where $V_h = h^2L_z$ is the physical volume of the unit control cell and Δt_{NS} is the continuum time step. The two diagonal components, W_{xx} and W_{yy}, are taken to be two uncorrelated Gaussian random numbers with zero mean and variance of 2. The two off-diagonal components are equivalent, i.e., $W_{xy} = W_{yx}$, and their value is assigned a Gaussian random number with a zero mean and a unit variance. For the two-dimensional staggered grid, W_{xx} and W_{yy} are defined at the centers of the cells, and W_{xy} and W_{yx} are defined at the cell corners.

In the context of the staggered discretization, the discretized differential operators

are taken to be as follows:

$$\begin{aligned}&\nabla \cdot \boldsymbol{U} \rightarrow \\ &\mathcal{D}(\boldsymbol{U})_{(i,j)} = \frac{U_{x,(i+\frac{1}{2},j)} - U_{x,(i-\frac{1}{2},j)}}{h} + \frac{U_{y,(i,j+\frac{1}{2})} - U_{y,(i,j-\frac{1}{2})}}{h};\end{aligned} \tag{4.26}$$

$\nabla^2 \boldsymbol{U} \rightarrow$

$$\begin{aligned}&\mathcal{L}(\boldsymbol{U})_{x,(i-\frac{1}{2},j)} = \\ &\frac{U_{x,(i+\frac{1}{2},j)} - 2U_{x,(i-\frac{1}{2},j)} + U_{x,(i-\frac{3}{2},j)}}{h^2} + \frac{U_{x,(i-\frac{1}{2},j+1)} - 2U_{x,(i-\frac{1}{2},j)} + U_{x,(i-\frac{1}{2},j-1)}}{h^2}\end{aligned} \tag{4.27}$$

$$\begin{aligned}&\mathcal{L}(\boldsymbol{U})_{y,(i,j-\frac{1}{2})} = \\ &\frac{U_{y,(i+1,j-\frac{1}{2})} - 2U_{y,(i,j-\frac{1}{2})} + U_{y,(i-1,j-\frac{1}{2})}}{h^2} + \frac{U_{y,(i,j+\frac{1}{2})} - 2U_{y,(i,j-\frac{1}{2})} + U_{y,(i,j-\frac{3}{2})}}{h^2};\end{aligned}$$

$$\begin{aligned}&\nabla P \rightarrow \\ &\mathcal{G}(P)_{x,(i-\frac{1}{2},j)} = \frac{P_{(i,j)} - P_{(i-1,j)}}{h} \\ &\mathcal{G}(P)_{y,(i,j-\frac{1}{2})} = \frac{P_{(i,j)} - P_{(i,j-1)}}{h};\end{aligned} \tag{4.28}$$

$$\begin{aligned}&\nabla \cdot [(2k_B T\mu)^{1/2}\widetilde{\boldsymbol{W}}] \rightarrow \\ &\sqrt{\frac{2k_BT\mu}{V_h \Delta t_{NS}}}\mathcal{D}(\boldsymbol{W})_{x,(i-\frac{1}{2},j)} = \\ &\sqrt{\frac{2k_BT\mu}{V_h \Delta t_{NS}}}[\frac{W_{xx,(i,j)} - W_{xx,(i-1,j)}}{h} + \frac{W_{xy,(i-\frac{1}{2},j+\frac{1}{2})} - W_{xy,(i-\frac{1}{2},j-\frac{1}{2})}}{h}] \\ &\sqrt{\frac{2k_BT\mu}{V_h \Delta t_{NS}}}\mathcal{D}(\boldsymbol{W})_{y,(i,j-\frac{1}{2})} = \\ &\sqrt{\frac{2k_BT\mu}{V_h \Delta t_{NS}}}[\frac{W_{yy,(i,j)} - W_{yy,(i,j-1)}}{h} + \frac{W_{yx,(i+\frac{1}{2},j-\frac{1}{2})} - W_{yx,(i-\frac{1}{2},j-\frac{1}{2})}}{h}];\end{aligned} \tag{4.29}$$

$$\boldsymbol{U}\cdot\nabla\boldsymbol{U}=\nabla\cdot\boldsymbol{U}\boldsymbol{U}\rightarrow$$

$$\begin{aligned}&\mathcal{A}(\boldsymbol{U})_{x,(i-\frac{1}{2},j)}=\\&\frac{(U_{x,(i+\frac{1}{2},j)}+U_{x,(i-\frac{1}{2},j)})^2-(U_{x,(i-\frac{1}{2},j)}+U_{x,(i-\frac{3}{2},j)})^2}{4h}\\&+\frac{(U_{y,(i,j+\frac{1}{2})}+U_{y,(i,j-\frac{1}{2})})^2-(U_{y,(i-1,j+\frac{1}{2})}+U_{y,(i-1,j-\frac{1}{2})})^2}{4h}\end{aligned}\tag{4.30}$$

$$\begin{aligned}&\mathcal{A}(\boldsymbol{U})_{y,(i,j-\frac{1}{2})}=\\&\frac{(U_{y,(i,j+\frac{1}{2})}+U_{y,(i,j-\frac{1}{2})})^2-(U_{y,(i,j-\frac{1}{2})}+U_{y,(i,j-\frac{3}{2})})^2}{4h}\\&+\frac{(U_{x,(i+\frac{1}{2},j)}+U_{x,(i-\frac{1}{2},j)})^2-(U_{x,(i+\frac{1}{2},j-1)}+U_{x,(i-\frac{1}{2},j-1)})^2}{4h},\end{aligned}$$

where the lowercase index (i,j) denotes that the quantity is defined at position $(ih+h/2, jh+h/2)$.

The equations are integrated with a time step $t_{NS}=0.1\tau$. We implement a predictor-corrector method developed by Griffith *et al.*,[201,226] which has been shown to have second order temporal accuracy with respect to reproducing the equilibrium covariances of the fluctuating velocity field.[201] For example, the numerical integration procedure from time step $n\Delta t_{NS}$ to $(n+1)\Delta t_{NS}$ is demonstrated as follows. In the predictor step, the Euler method is used for the advection term and the Crank-Nicolson method is used for the viscous diffusive term,

$$\begin{aligned}&\frac{\hat{\boldsymbol{U}}^{n+1}-\boldsymbol{U}^n}{\Delta t_{NS}}+\mathcal{A}(\boldsymbol{U}^n)=\\&\mathcal{G}\hat{P}^{n+\frac{1}{2}}+\mu\mathcal{L}(\frac{\hat{\boldsymbol{U}}^{n+1}+\boldsymbol{U}^n}{2})+\sqrt{\frac{2k_BT\mu}{V_h\Delta t_{NS}}}\mathcal{D}(\boldsymbol{W}^{n+1})+\boldsymbol{F}_{ad}^{n+1}\end{aligned}\tag{4.31}$$

$$\mathcal{D}(\hat{\boldsymbol{U}}^{n+1})=0.\tag{4.32}$$

The following corrector step also uses the Crank-Nicolson method for the diffusive term. The advection term is evaluated explicitly at the midpoint, and the values of the volumetric force term and the stochastic flux term are kept the same as in the predictor step,

$$\begin{aligned}\frac{\boldsymbol{U}^{n+1}-\boldsymbol{U}^{n}}{\Delta t_{NS}}+\mathcal{A}(\frac{\hat{\boldsymbol{U}}^{n+1}+\boldsymbol{U}^{n}}{2})=\\ -\mathcal{G}P^{n+\frac{1}{2}}+\mu\mathcal{L}(\frac{\boldsymbol{U}^{n+1}+\boldsymbol{U}^{n}}{2})+\sqrt{\frac{2k_BT\mu}{V_h\Delta t_{NS}}}\mathcal{D}(\boldsymbol{W}^{n+1})+\boldsymbol{F}_{ad}^{n+1}\end{aligned} \tag{4.33}$$

$$\mathcal{D}(\boldsymbol{U}^{n+1})=0. \tag{4.34}$$

For both Eqs. (4.31) and (4.32) and Eqs. (4.33) and (4.34), the discretized momentum and continuity equations are solved together as a whole linear system of equations through an iterative Krylov solver, where Kim and Moin's projection method[227] is employed as the preconditioner. Unlike the semi-implicit projection methods, e.g., Refs. [227–229], this solver does not suffer from the commutator error in non-periodic systems which arises from the splitting of the velocity and pressure updates.

4.2.5 Coupling Continuum Fluid Dynamics with Molecular Dynamics

Figure 4.2 illustrates the coupling between the continuum fluid dynamics and the molecular dynamics. The overlap region is introduced to couple the particle-based molecular dynamics description with the continuum description of the bulk fluid flow. The continuum fluid ends at y_0, where it receives boundary conditions from the molecular dynamics simulation. The molecular dynamics description is confined below y_5, and it gets constrained near that region to follow the solutions of

the continuum fluid dynamics. In general, there are two types of strategies to couple molecular dynamics with continuum fluid dynamics: state-based coupling[97–102] and flux-based coupling.[107,108,112,113] The former type aims at matching the state variable (e.g., mean velocity and temperature) of the two descriptions, and the later is designed to match the fluxes of conserved variables (e.g., pressure tensor and energy flux). For more details and comparisons of the different methods, we refer to the reviews[230–232] and the original papers as cited. In this work, we implement a state-based coupling method which is developed based on the original coupling scheme proposed by Nie *et al.*[98]

4.2.5.1 Boundary Conditions for Continuum Fluid Dynamics from Molecular Dynamics

At the bottom of the continuum fluid dynamics subdomain (indicated as y_0 in Figure 4.2), the molecular dynamics simulation supplies mean velocities as the boundary conditions to the Navier-Stokes fluctuating hydrodynamic equations. The velocities of the MD particles are averaged within volumes equal to the continuum unit mesh cell centered at the positions where the continuum velocities are defined. For example, boundary conditions for the x and y components of velocities are evaluated at the rightward arrows at $y_0 - h/2$ and upward arrows at y_0, respectively. The spatially averaged velocities are further averaged temporally over a particle-continuum time-coupling interval Δt_{cp}, and then fed into the Navier-Stokes fluctuating hydrodynamics equations as the boundary conditions.

In a previous series of studies,[98–102] a number of different molecular dynamics simulations were performed in the same MD subdomain and were coupled to a single deterministic Navier-Stokes solution. Those MD simulations served as different realizations associated with the same ensemble. A deterministic Navier-Stokes equation was used, with boundary conditions provided by the ensemble averaged velocities from the molecular dynamics simulations. By this many-to-one MD-continuum coupling, the statistical noise in the results was significantly reduced, since the thermal fluctuations associated with the long-lived hydrodynamic modes in the molecular fluids are effectively reduced by the ensemble averaging.

In this study, we use one-to-one MD-continuum coupling. In each simulation, only one molecular dynamics realization is performed in a given subdomain, and thus there is no ensemble averaging for the MD velocities that are passed to the continuum fluid dynamics. That is because we want to retain the thermal fluctuations of the long-living and long wavelength hydrodynamic modes. Also, the SELM description for the charges can be naturally integrated with the one-to-one coupled MD-continuum system.

4.2.5.2 Boundary Conditions for Molecular Dynamics from Continuum Fluid Dynamics

As illustrated in Figure 4.2, the molecular dynamics subdomain ends at y_5. To prevent the MD fluid particles from leaving the subdomain, in the region between y_4

and y_5, a confinement force is applied to the MD particles in the y direction,[98–102]

$$f_y = -\alpha h \frac{y - y_4}{y_5 - y}, \tag{4.35}$$

where the prefactor is taken to be $\alpha = 1.5\epsilon/\sigma^2$. This force ensures that the fluid density smoothly decays to zero when approaching y_5, without introducing significant oscillations in the density profile.

Mass flux control is also performed cell by cell in this region by inserting or removing fluid particles.[98–102] At each MD-continuum coupling time step, the net vertical mass flux across each cell boundary at y_4 is calculated from the continuum solutions for the next coupling interval Δt_{CP},

$$\Delta Q_{CP} = U_y \Delta t_{CP} \rho h L_z. \tag{4.36}$$

Since only an integer number of particles can be inserted or removed, the change of the fluid particles number is approximated by

$$\Delta N_{CP} = \text{int}[(\Delta Q_{CP} + Q_{res})/m], \tag{4.37}$$

where the function int(x) rounds the input x to its integer part and Q_{res} denotes the residual of the rounding operation from the last coupling time step. If $\Delta N_{CP} > 0$, the ΔN_{CP} particles closest to y_5 are removed at regular time intervals over the following Δt_{CP}. If $\Delta N_{CP} < 0$, ΔN_{CP} particles are inserted into the cell between y_4 and y_5 and evenly over the following Δt_{CP}. The particles are inserted to locations with desirable

potential and potential gradient which are found by the USHER algorithm.[233] The initial velocities of the inserted particles are set to the target continuum velocity $\boldsymbol{U}_{CP}$ of the corresponding cell. $\boldsymbol{U}_{CP}$ is defined at the center of each cell and is given by the average of the continuum velocities which are defined at the corresponding edges of the cell. In order to prevent over-heating caused by the particle insertion, the Langevin thermostat [as described in Eq. (4.11)] is also applied between y_4 and y_5 in the x and y directions to relax the particles towards the local continuum velocity $\boldsymbol{U}_{CP}$.

In order to impose the solutions of the continuum fluid dynamics back to the molecular dynamics simulation, we follow the methods proposed previously by O'Connell and Thompson[97] and Nie *et al.*[98] . A relaxed constrained dynamics method is employed to force local mean velocities of the MD simulation to follow the continuum velocities. In the region between y_3 and y_4, a constraint force is added on the fluid particles along the x and y directions. For example, the constraint force for the particles within a continuum mesh cell indexed by J is given by,

$$\boldsymbol{f}_{CP} = \frac{1}{\xi}(\boldsymbol{U}_{CP,J} - \frac{1}{N_J}\sum_{i=1}^{N_j}\boldsymbol{u}_i - \frac{\Delta t_{MD}}{N_J}\sum_{i=1}^{N_j}\boldsymbol{f}_i), \tag{4.38}$$

where $\sum_{i=1}^{N_j}$ represents a spatial average over all the particle within the cell J, $\boldsymbol{f}_i$ denotes the total force (excluding the constraint force) exerted on particle i, and $\boldsymbol{u}_i$ is the velocity of the particle i.

The parameter ξ controls the strength of the constraint. It gives a relaxation

time scale during which the mean MD velocity gets relaxed to the target continuum velocity. In the previous series of studies,[98–102] a very strong constraint was imposed by setting $\xi = \Delta t_{MD}$. As a result, the mean MD velocity was forced to instantaneously match the target continuum velocity that was extrapolated (or interpolated) to the new MD time step from the latest two continuum time steps. This instantaneous coupling significantly alters the intrinsic time correlation of the molecular dynamics particles and thus can affect the diffusion in the overlap region.

The instantaneous matching constraint can be strictly derived for an incompressible fluid with constant density and it does not include the intrinsic density fluctuations in the molecular dynamics. Under certain circumstance, the density fluctuation can influence the accuracy and stability of such a strong velocity-based constraint while one can get better results by releasing some of the constraints.[99] Also, over constraining the particles with a relaxation time shorter than their intrinsic velocity auto-correlation time, 0.14τ,[97] artificially disturbs the dynamics. This disturbance can propagate into the MD region and get passed back to the continuum solver through the boundary condition for our one-to-one MD-continuum coupling. Although it does not affect the long-time averaged mean flow, this unphysical perturbation lives long enough to alter the diffusivity in the finite overlap region. We avoid these problems by following O'Connell and Thompson and setting $\xi = 0.5\tau$ which is larger than the velocity auto-correlation time of the fluid particles ($\sim 0.14\tau$). This provides a moderate relaxation for the fluid particles and thus alleviates the artifacts associated

with the constraint. Also, it is small enough to capture important hydrodynamic time scales. For the same reason, we implement a large overlap region, so that the MD and SELM simulations exchange charges (see Section 4.2.6) in the middle where the MD system is relaxed.

4.2.6 Exchanging Charges between Molecular Dynamics and Stochastic Euler-Lagrangian Simulations

In the hybrid simulations, charges can move freely between different subdomains with different descriptions. The transition between the molecular dynamics and the stochastic Eulerian Lagrangian descriptions is performed when a charge moves across the middle of the overlap region.

As illustrated in Figure 4.2, if a charged particle of MD description moves up across $y_{SELM} = y_2$, the unit charge it carries is split from the particle and becomes a point charge modeled by the stochastic Eulerian Lagrangian method. The particle loses its originally assigned charge and becomes a neutral fluid particle that only interacts with other MD particles through the Lenard-Jones potential [Eq. (4.1)]. A decorrelation time period of 0.25τ is introduced before the transition, to de-correlate the charge from the particle's velocity.

If a SELM point charge moves into the region below $y_{MD} = y_2 - 2\sigma$, the charge is tagged as "to-be-assigned" and needs to be assigned back to a neutral fluid particle in the MD system. This"to-be-assigned" charge starts to search the neutral MD particles in the neighborhood for one that reaches the "capture zone" given by: $|r_y| < 0.01\sigma$

and $\sqrt{r_x^2 + r_z^2} < 0.5\sigma$, where (r_x, r_y, r_z) denotes the relative position with respect to the charge. Once the "to-be-assigned" charge finds a neutral MD particle within the "capture zone", it starts to follow the motion of the MD particle and the SELM description [Eq. (4.15)] is turned off. The electrostatic force on the point charge is imposed onto the MD particle. The charge's velocity is set to be the MD particle's velocity plus a constant velocity pulling the charge towards the MD particle. The pulling velocity is given by $\boldsymbol{r}_0/t_a$, where $\boldsymbol{r}_0$ is the initial relative position when the charged is captured and $t_a = 1\tau$. After 1τ, when the change reaches the position of the MD particle, it is fully assigned to the MD particle and this charge assignment process is completed.

On average it takes several τ's for the "to-be-assigned" SELM charge to meet a neutral MD particle within such a small "capture zone". If it moves into the region below $y = y_{MD} - 1\sigma$ (which is rare), the "capture zone" is enlarged to $|r_y| < 0.2\sigma$ and $\sqrt{r_x^2 + r_z^2} < 0.5\sigma$, which ensures that the SELM charge gets transformed to be a MD particle before moving too deep into the MD subdomain. On the other hand, if the "to-be-assigned" SELM charge moves back in the region above $y = y_{MD} + 1\sigma$, it is no longer "to-be-assigned", so the tag is removed and the searching process is turned off.

With these schemes, the conservation laws of the mass of the MD system and the total charge of whole system are strictly preserved during the charges' transitions between different descriptions. As long as the flow field of the implicit background

fluid is well matched with the MD background, the MD-to-SELM transition is quite natural. The associated disturbance on the charge's trajectory is negligible at time scales longer than the velocity auto correlation time. As for the SELM-to-MD scheme, the disturbance to the trajectory of the charge is mainly controlled by the size of the "capture zone". The small and thin size of the "capture zone" ensures that the transport and distribution of charges at long (continuum hydrodynamic) time and length scales are not affected. Moreover, because of the low charge concentration in this region, the disturbance in the trajectories is very small compared to the long distances between the charges. Therefore, the transition of a given charge does not affect the dynamics of the other charges in the system.

In this transition region, the MD and continuum systems are allowed to relax by themselves, and local mean MD velocities do not fully match with continuum fluid solutions at short time scales. Due to the small size of the transition region, this mismatch of the background flow noticeably affects the smoothness of the transitions of charges and can lead to a discontinuity ($\sim 5\%$) in the mean profile of the charge concentration. Therefore, we replace the continuum solutions on the grid points below y_3 by the current mean MD velocities to interpolate the reference velocity $\boldsymbol{U}_{ref}$ [Eq. (4.11)] for the SELM charges.

4.2.7 Time Coupling Scheme

To describe the time-coupling scheme, the general procedure of the hybrid simulation over a whole time-coupling interval, from t to $t + \Delta t_{CP}$, is written down as

follows.

1. Update the solutions for continuum fluid flow:

   1.1. The boundary conditions and the volumetric force field $\boldsymbol{F}_{ad}$ supplied by the MD and SELM simulations over the last time-coupling interval, $t - \Delta t_{CP}$ to t, are used to integrate Eqs. (4.21) and (4.22) from $t - \Delta t_{CP}$ to t. This updates the continuum flow field from $\boldsymbol{U}(t - \Delta t_{CP})$ to $\boldsymbol{U}(t)$. The resulting $\boldsymbol{U}(t)$ is then used to extrapolate the background reference flow velocity [$\boldsymbol{U}_{ref}$ in Eq. (4.15)] for the SELM simulations for the following time intervel, i.e., from t to $t + \Delta t_{CP}$;

   1.2. With the same boundary conditions and $\boldsymbol{F}_{ad}$, Eqs. (4.21) and (4.22) are further integrated for another Δt_{CP} to provide a prediction, $\boldsymbol{U}^*(t+\Delta t_{CP})$, for the flow field at the time step $t + \Delta t_{CP}$, where $\boldsymbol{U}^*(t + \Delta t_{CP})$ is used to constrain the MD simulations for the following time interval Δt_{CP}.

   1.3. $\boldsymbol{U}(t)$ and $\boldsymbol{U}^*(t+\Delta t_{CP})$ are passed to the associated particulate simulations.

2. Run particulate (both MD and SELM) simulations, from t to $t + \Delta t_{CP}$. For each time step Δt_{MD}, the simulation procedure can be described as:

   2.1. Update the particles' positions for the MD and SELM simulations;

   2.2. Calculate the forces on the particles for the MD and SELM simulations;

   2.3. Update the particles' velocities for the MD and SELM simulations by Eqs. (4.7) and (4.8) and Eqs. (4.18) and (4.19), respectively;

2.4. Process and analyze statistical quantities;

3. Average the particulate data sampled over the past Δt_{CP} (between t and $t + \Delta t_{CP}$), and feed them to the continuum solver as the boundary conditions and the volumetric force field.

Simulation results with $\Delta t_{CP} = 0.5\tau$ are reported in the following sections. We also verified that simulations with $\Delta t_{CP} = 1\tau$ provide equivalent results.

4.3 Results and Discussion

4.3.1 Incompressible Navier-Stokes Fluctuating Hydrodynamic Solver in Bulk Systems

We first consider an equilibrium bulk fluid system with periodic boundary conditions in all dimensions. The system size is taken to be $L_x \times L_y \times L_z = 34\sigma \times 34\sigma \times 8.5\sigma$. The equations of incompressible Navier-Stokes fluctuating hydrodynamics, Eqs. (4.21) and (4.22), are solved on a 10×10 mesh grid in the x-y plane.

The thermal fluctuations of the velocities in real space are shown in Figure 4.3. As predicted by statistical physics,[193,196,234,235] the cell averaged velocities from the MD simulations fluctuate in each dimension (denoted by i) with a variance that is inversely proportional to the mass of the cell,

$$< U_i^2 >= k_B T/\rho h^2 L_z. \tag{4.39}$$

This is also consistent with the prediction from the continuum hydrodynamic per-

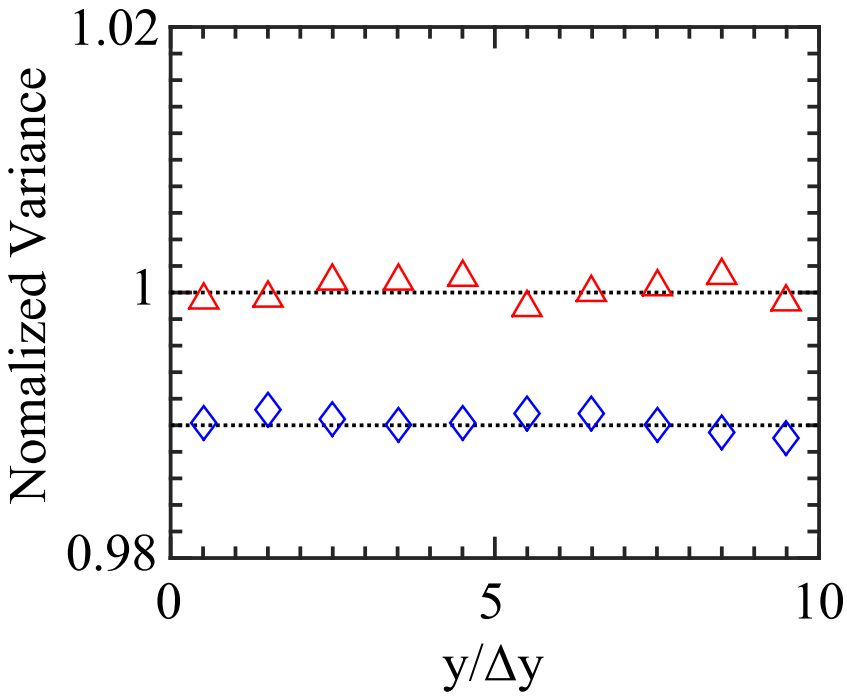

Figure 4.3: Normalized variances of the U_x as a function of y normalized by the cell size h from periodic bulk simulations. Blue diamonds denote the normalized variance, $2\mathrm{var}(U_x)\rho h^2 L_z/k_B T$, for the solution of the incompressible fluctuating hydrodynamics. Red triangles represent the variance of the cell-averaged velocities from the MD simulation, normalized as $\mathrm{var}(U_x)\rho h^2 L_z/k_B T$. The MD velocities are averaged over the unit cells centered at the positions of the continuum velocities. The typical relative error is $\sim 0.2\%$.

spective. The degrees of freedom of the system can be represented by the associated Fourier modes in the spectral space. In equilibrium, each hydrodynamic mode fluctuates and carries an equal portion of the thermal energy,

$$\frac{m}{2} < U(-\boldsymbol{k}, 0)U(\boldsymbol{k}, 0) >= \frac{k_B T}{2}, \tag{4.40}$$

where $U(\boldsymbol{k}, t)$ represents the given Fourier mode of the velocity field at the wave vector $\boldsymbol{k}$ and the time t. By performing the inverse Fourier transform over all the associated modes, Eq. (4.39) is recovered.

For the ICNSFH equations, Eqs. (4.21) and (4.22), the incompressible condition [Eq. (4.22)] constrains all the longitudinal Fourier modes to zero, leading to a $1/d$ reduction in the total degrees of freedom for the velocity field, where d denotes the number of dimensions of the system. As a result, for our two-dimensional equations, the real space fluctuations of the velocity are reduced by a half. As shown in Figure 4.3, the normalized numerical result, $2\rho h^2 L_z < U_x^2 > /k_B T$, is in fact converging to 0.99. This additional reduction comes from the center of mass velocity which is taken to be zero, eliminating one degree of freedom out of the 100 for different grid cells. There is a similar reduction for the MD case but it is much smaller because the number of atoms is much larger than the number of cells.

The transportation and dissipation of the fluctuations within the system can be disclosed by the time auto-correlation functions of the associated Fourier modes. For the equilibrium system with small fluctuations, Eq. (4.21) can be linearized by

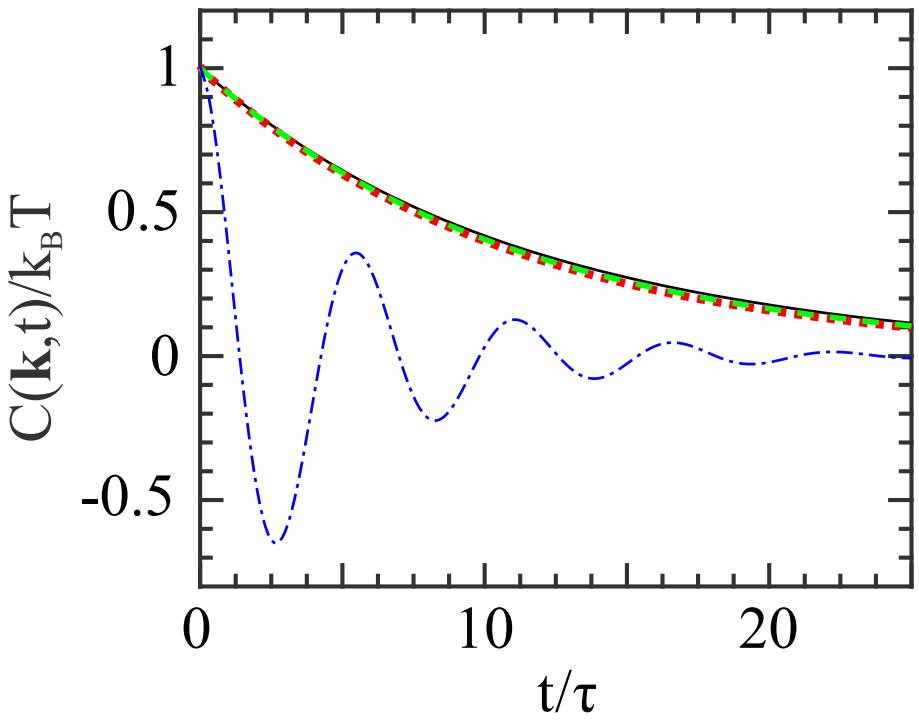

Figure 4.4: Autocorrelation functions of the velocity fields associated with the wave number $\boldsymbol{k} = (2\pi/L_x, 0)$ from the periodic bulk simulations. The transversal auto-correlation function $C_\perp(\boldsymbol{k}, t)$ calculated from the MD simulations, ICNSFH simulations and exponential decay of the analytical prediction Eq. (4.41) are plotted as the red dotted, black solid and green dashed lines, respectively. For comparison, the associated longitudinal auto-correlation function, from the MD simulation is also presented by the blue dash-dotted line. The MD velocities are averaged over the unit cells centered at the positions of the continuum velocities.

neglecting the nonlinear advection term. One can analytically solve the linearized ICNSFH equations for the time auto-correlation function of the transverse velocity modes,[196,225,235,236]

$$C_\perp(\boldsymbol{k},t) =< U_\perp(-\boldsymbol{k},t)U_\perp(\boldsymbol{k},0) >=< U_\perp(-\boldsymbol{k},0)U_\perp(\boldsymbol{k},0) > e^{-\nu k^2 t}. \tag{4.41}$$

Figure 4.4 compares $C_\perp(\boldsymbol{k},t)$ at $\boldsymbol{k} = (2\pi/L_x, 0)$. Good agreement is found among the results from the ICNSFH simulation, the MD simulation, and the analytical solution given by Eq. (4.41).

The implemented numerical scheme for the ICNSFH equations can correctly reproduce the $C_\perp(\boldsymbol{k},t)$ up to the discretization resolution limit $\sim 5h$.[111,201] The modes with shorter wavelengths decay more slowly than in the MD system, but still too fast to affect the important bulk dynamics.[111,201,236] On the other hand, this stagger-grid-based scheme maintains the discrete fluctuation-dissipation balance at every wavenumber.[201,221] Thus, the scheme always reproduces the correct velocity Fourier spectrum $C_\perp(\boldsymbol{k},0)$ that follows the equipartition rule [Eq. (4.40)] for all the resolved modes. Moreover, we have verified that increasing Δt_{NS} up to 0.5τ and decreasing Δt_{NS} down to the MD time step 0.005τ produce indistinguishable results.

For comparison, Figure 4.4 also presents the auto-correlation function associated with the longitudinal Fourier mode

$$C_\parallel(\boldsymbol{k},t) =< U_\parallel(-\boldsymbol{k},t)U_\parallel(\boldsymbol{k},0) > \tag{4.42}$$

at $\boldsymbol{k} = (2\pi/L_x, 0)$. It fluctuates quickly with the short period set by the time for a sound wave to pass across the whole system. The magnitude of the fluctuation also decays faster than the transversal mode. In the low Mach number limit of our applications, sonic effects have a negligible influence on the long time scale bulk hydrodynamics, and do not affect the transport of the charges. With fast sound waves eliminated, the incompressible hydrodynamic equations allow us to use a much larger time step.

4.3.2 Matching Bulk Diffusion in SELM and MD

In SELM simulations, Eq. (4.11) models the particle dynamics and its coupling with the local fluid at short time scales. At long time scales, the particle dynamics is governed by the underlying continuum fluid dynamics modeled by Eqs. (4.21) and (4.22). With the Eulerian mesh and the interpolation scheme given, the only adjustable parameter in Eq. (4.11) is the bare friction coefficient Γ_{bare}.

We determined Γ_{bare} by tuning its value in a series of SELM simulations of neutral test particles in a bulk fluid system with size $34\sigma \times 34\sigma \times 8.5\sigma$, until the measured diffusion coefficient matched the self diffusion coefficient of the neutral fluid particles in the corresponding MD system. Since ions and neutral particles have the same interactions, this strategy is equivalent to matching the diffusion coefficient for the ions as long as they are in the low concentration limit. However, the latter approach has a greater computational cost because of the small number of ions.

For SELM simulations to calibrate Γ_{bare}, the test particles are taken to be neutral

mass points with zero inter-particle interactions. Thus, there is no force spread back to the continuum fluid equations. The diffusion is not affected by the number of test particles in the system. Therefore, one does not need to remain in the dilute limit and can simulate enough test particles to achieve a desirable sampling efficiency.

To measure the diffusion coefficient, the mean square displacement of the particles along each direction i,

$$f_{MSD,i}(t) =< [r_i(t) - r_i(0)]^2 >, \tag{4.43}$$

is calculated from the simulations with an efficient sampling method described in Ref. [96]. Following the Einstein relation,[189] the diffusion coefficient is then determined as the long time limit of the slope of the mean square displacement with respect to time,

$$D_i = \lim_{t\to\infty} \frac{1}{2} f'_{MSD,i}(t), \tag{4.44}$$

where $f'_{MSD,i}$ denotes the slope

$$f'_{MSD,i}(t) = \frac{d}{dt} f_{MSD,i}(t). \tag{4.45}$$

We found the best fit when the bare friction coefficient was $\Gamma_{bare} = 15.93m/\tau$. The resulting time derivative of the mean-squared displacement is compared with MD results in Figure 4.5. The y-direction results are not shown since they are identical to the x direction in this case. Atomistic effects dominate at short time scales. The

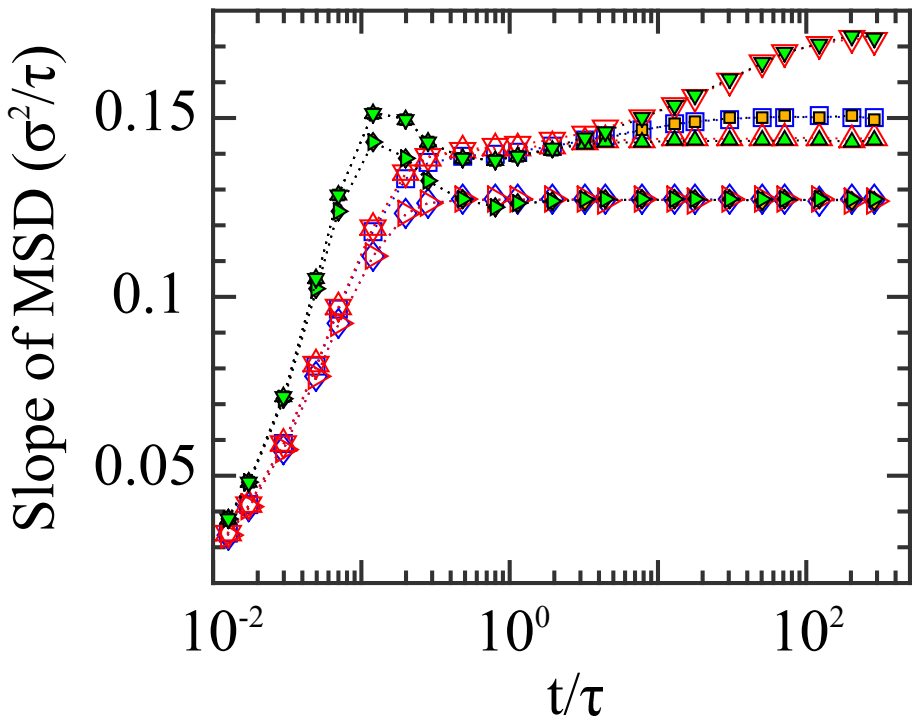

Figure 4.5: Slope of the mean square displacement function [Eq. (4.45)] with respect to time, for systems with $L_x \times L_y \times L_z = 34\sigma \times 34\sigma \times 8.5\sigma$ (squares and diamonds) and $17\sigma \times 68\sigma \times 8.5\sigma$ (triangles). MD and SELM results are plotted as closed and open symbols, respectively. The symbol orientation indicates the direction of displacement: x (squares) and z (diamonds) directions for the $34\sigma \times 34\sigma \times 8.5\sigma$ systems; x (upward), y (downward) and z (rightward) directions for the $17\sigma \times 68\sigma \times 8.5\sigma$ systems.

SELM curve exhibits a quick rise within the short initial time period $\sim 0.1\tau$. This is associated with the inertial relaxation of the particle due to the frictional damping force, $-\Gamma_{bare}(\boldsymbol{u} - \boldsymbol{U}_{ref}(\boldsymbol{r}))$, and the relaxation time scale is set by the particle's mass and the bare friction coefficient, $\sim m/\Gamma_{bare}$. The MD curve shows a quicker rise in the short inertial time followed by a small drop which is due to collisions with neighbors. At longer time scales ($\gtrsim 1\tau$), the hydrodynamic fluctuations become dominant, leading to slow increases in both of the curves. The two curves collapse nicely with each other for time scales longer than around 5τ, and saturate together after around 50τ, which is associated with the lifetime of the lowest transverse hydrodynamic mode (with the longest wavelength L_y). Therefore, the diffusion coefficients can be determined from the plateau values after the saturation, and the SELM simulation accurately reproduces the MD result, $D_x = 0.0753 \pm 0.0002\sigma^2/\tau$.

Note that the diffusion in the z direction shows different behavior for MD simulations (Figure 4.5). This is because of additional damping from the Langevin thermostat. At the short inertial time scale, the MD curve rises to a lower peak than for the x direction. For times greater than 1τ, the curve remains constant, leading to a smaller diffusion coefficient than in the other two directions, $D_z = 0.0635 \pm 0.0002\sigma^2/\tau$. This is because the long time scale hydrodynamic modes of the z-direction velocity are damped to zero by the Langevin thermostat. This is consistent with our model for the continuum fluid dynamics which assumes a two-dimensional flow field for the x and y directions and a zero flow background in the z direction. Correspondingly,

the SELM simulation is implemented differently in the z direction: imposing a zero background reference velocity and a different input value for the friction coefficient, $\Gamma_{bare,z} = 17.30m/\tau$, where the classical Langevin dynamics [Eq. (4.9)] is recovered. As shown in Figure 4.5, this produces a nice agreement with the MD result in the z direction. Note that the difference in diffusion constants along x and z can be reduced by lowering the Langevin thermostat damping constant. Using other thermostats such as DPD produces other artifacts including an increased viscosity.

With the bare friction coefficients determined , we further test the SELM approach for a variety of systems with different sizes. Previous studies[124,131,214,217,237–239] have shown that due to long-range hydrodynamic interactions, the diffusive mass transport can exhibit a significant dependence on the finite system size. This can be well described within the framework of incompressible Stokes flow. In general, a larger system size allows more transverse modes which fluctuate with longer wavelengths and lifetimes, and thus produce a larger diffusion coefficient. For cubic three-dimensional periodic systems, a simple $1/L$ scaling was found as the leading order of the system size effect on the diffusion coefficient, where L denotes the system size.[124,131,214,217,237–239]

Figure 4.5 demonstrates the results from an example where the system size is modified to $17\sigma \times 68\sigma \times 8.5\sigma$. Comparing the MD curves with the $34\sigma \times 34\sigma \times 8.5\sigma$ results, the z-direction result is unaffected, since hydrodynamic effects are eliminated for the z direction. The curves in the x and y directions remain unchanged in the regime $t \lesssim 1\tau$ since the short-time dynamics remains the same. At longer time scales,

$f'_{MSD,x}(t)$ and $f'_{MSD,y}(t)$ are altered substantially and become anisotropic. $f'_{MSD_x}(t)$ is lifted upward in the hydrodynamic regime $t \gtrsim 5\tau$ and the saturation time is postponed. As a result, D_x is increased by around 15 percent. In contrast, the diffusion is suppressed in the y direction, where D_y is reduced by around 5 percent. The observation that growing the system size along one direction increases the degree of diffusion along the other reflects the incompressible nature of the underlying fluctuating hydrodynamic effects. For example, the enhanced diffusion in the x direction is due to the enhanced time correlation of the x-direction velocity in the long time tail which is mainly associated with the long-wavelength transverse modes added by the elongated system length in the y dimension.

With the given bare friction coefficients and the incompressible Navier-Stokes fluctuating hydrodynamic model, the SELM simulation can accurately reproduce the $f'_{MSD}(t)$ curves for the for the whole time range after around 5τ. Γ_{bare} is only associated with the short-time relaxation of the particles. The correctly tuned value should apply to SELM simulations of different systems as long as the underlying short-time dynamics in the associated all-atom MD systems remain the same. Therefore, we take $\Gamma_{bare,x} = \Gamma_{bare,y} = 15.93m/\tau$ and $\Gamma_{bare,z} = 17.30m/\tau$ for all the other simulations in this study.

The time-coupling interval, Δt_C, is another parameter in the SELM model that needs to be justified. We have verified that varying Δt_C from the atomic time step Δt_{MD} up to 2τ (at small Δt_C, Δt_{NS} was also adjusted to match Δt_C) produces neg-

ligible differences in the results. Further increasing Δt_C will increase the diffusion coefficient, since Δt_C is reaching the time scale associated with important hydrodynamic effects.

We have also checked the shear viscosity from the different MD systems. According to the Green-Kubo formula,[96,188] the shear viscosity can be evaluated from the time correlation function of the shear stress T_{xy},

$$\mu = \frac{L_x L_y L_z}{k_B T} \int_0^\infty < T_{xy}(0) T_{xy}(t) > dt. \tag{4.46}$$

T_{xy} can be calculated by

$$T_{xy} = \frac{1}{L_x L_y L_z} [\sum_i m u_{x,i} u_{y,i} + \frac{1}{2} \sum_{i \neq j} (x_i - x_j) F_{y,ij}], \tag{4.47}$$

where $F_{y,ij}$ denotes the y component of the force exerted on particle i from j. In agreement with the previous studies,[23,240] unlike the self diffusion coefficient, the shear viscosity is barely affected by the variation of system size. Therefore, one can safely use $\mu = 2.14\epsilon\tau\sigma^{-3}$ for systems with different geometries.

4.3.3 Dynamical Channel Flow

In this subsection, we begin to demonstrate our hybrid scheme in the channel flow geometry. The fluid is confined between two parallel flat solid walls at $y = 0\sigma$ and $y = L_y = 54.4\sigma$. The spatial periods along x and z directions are $L_x = 34\sigma$ and $L_z = 8.5\sigma$, respectively. The setup of the simulation is symmetric with respect to the x-z plane at the center of channel, i.e., $y = L_y/2 = 27.2$. For the lower half of the

system, the MD simulation is performed in the region below $y = 23.8\sigma$ (corresponding to the y_5 in Figure 4.2). The continuum fluid equations, [Eqs. (4.21) and (4.22)] are solved in the region above $y = 7.8\sigma$ (corresponding to the y_0 in Figure 4.2).

To test our relaxed MD-continuum coupling scheme, we simulate a time varying channel flow for a neutral fluid. Starting with zero mean velocity everywhere at time $t = 0\tau$, the flow is driven by moving the top wall along the x direction with a time varying velocity,

$$u(t) = u_0 + u_0 \sin[2\pi(\frac{t}{t_0} - 0.25)], \tag{4.48}$$

where $t_0 = 100\tau$ is the temporal period, and $u_0 = 1\sigma/\tau$. On the other side, the bottom wall is kept fixed.

In Figure 4.6, we show the time evolution of the mean velocities at $y = 11.9\sigma$, 25.5σ and 42.5σ, which are located at lower overlap, channel center, and the upper overlap regions, respectively. The velocities are averaged over each row of the continuum mesh cells and over a time period of 1τ. 240 simulations are performed for a further average to achieve a desirable signal-noise ratio for the high time resolution. The excellent agreement of the velocity evolution from the hybrid and continuum solutions reveals that our hybrid scheme provides accurate momentum coupling at the MD-continuum interface. Note that the MD and continuum solutions of the hybrid simulations closely match with each other at $y = 11.9\sigma$ and 42.5σ in the middle of overlap region where the two descriptions are allowed to relax by themselves with no constraint between them.

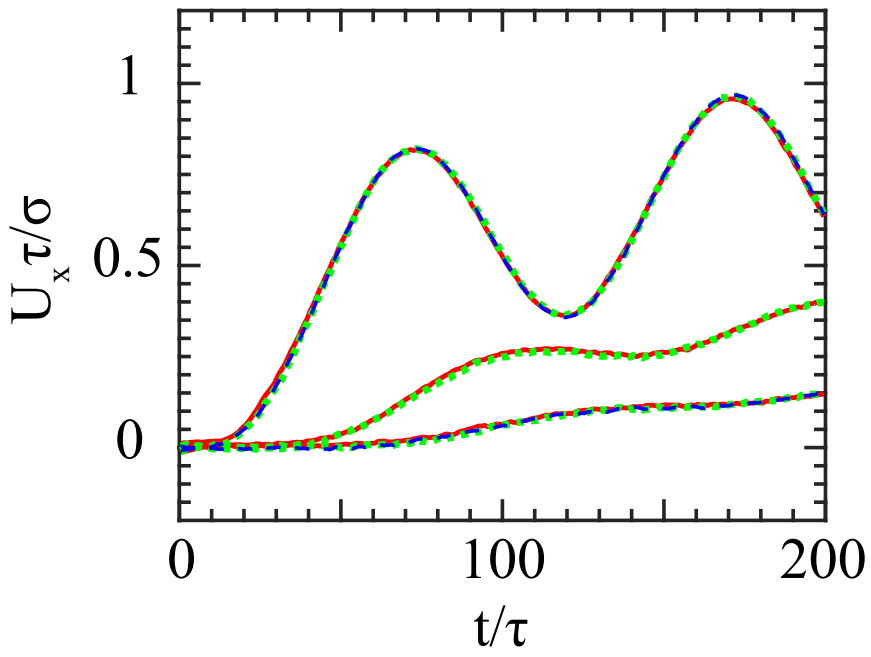

Figure 4.6: The time evolution of x-direction velocities for dynamic channel flow at different heights: $y = 11.9\sigma$, 25.5σ and 42.5σ, as represented by the separated curves from the bottom to the top of the figure. The full MD, hybrid MD and hybrid continuum results are presented by the red solid, blue dashed and green dotted lines, respectively. The results at each height are averaged over the whole row of cells.

4.3.4 Diffusion of Charges Between Between MD and SELM Regions

In this subsection we demonstrate that the coupling scheme allows free diffusion of discrete charges between the different subdomains in a channel. A total of $N_e = 160$ positive test charges are added at random positions in the channel used in the previous section. In the MD subdomain, neutral particles are chosen at random and assigned a positive point charge e. In the continuum domain, ions are introduced at a random position. The probability of being in the different domains is proportional to their volume. The walls are not charged, thus a uniform distribution is expected for test charges not close to wall, which provides a better sampling especially for the SELM description in the bulk (comparing with the cases shown in Figure 4.8 of Section 4.3.5).

Figure 4.7 shows the mean concentration profile as function of y. The system is still in the low concentration regime. To reach an acceptable signal-to-noise ratio, the charge concentration is averaged over a time period of about 20000τ and over 240 independent realizations. Within the statistics (the relative error is around 1 percent), the hybrid scheme accurately reproduces the constant concentration profile across the different subdomains. This manifests that the diffusivity of the test charges is accurately matched across the subdomains with different descriptions. Broken lines indicate the boundaries of the regions where the charges change from the SELM to MD description. Note that the charge densities associated with the SELM (blue dashed lines) and MD (red dotted line) descriptions drop rapidly near their end

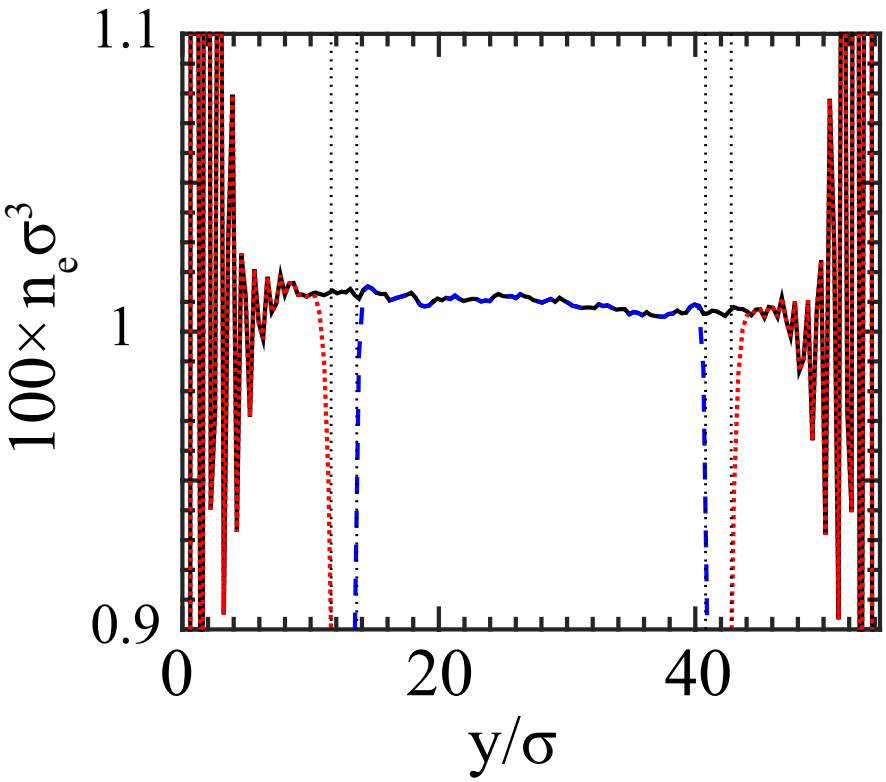

Figure 4.7: Mean concentration profile of the test charges in the channel as a function of y. The red dotted and blue dashed lines represent the portions of the test charges of the MD and the SELM descriptions, respectively. The black solid line indicates the total of the two. The vertical black dotted lines indicate boundaries of the transition region between MD and SELM descriptions of charges, y_{MD} and y_{SELM}. The boundaries of the y-axis indicate the positions of the wall surfaces.

of the exchange region. The MD density is suppressed slightly farther in to the MD region because assigning SELM charges to discrete atoms requires good alignment between their centers (see Section 4.2.6). Note that the total charge density remains constant within the statistical errors and shows no evidence of any change in behavior. This demonstrates that the diffusive transport is uniform across the transition region and that artifacts associated with the change in physical model are negligible. This conclusion was confirmed by other tests using imposed sinusoidal concentration gradients or other initial conditions.

4.3.5 Electroosmotic Flows in Flat Channels

In this subsection, we demonstrate the full hybrid scheme by simulating electroosmotic flows in channels with flat walls. The channel geometry setup is the same as in Sections. 4.3.3 and 4.3.4. At the beginning of the simulations, $N_e = 160$ positively charged particles are created in the fluid by randomly assigning a unit charge e to a neutral fluid particle in the MD subdomain or assigning a unit point charge e with a random position in the continuum fluid subdomain. The solid atoms in the surface layers (closest to the fluid) of the top and bottom walls are uniformly charged with a negative value to ensure that the whole system is electrically neutral. The full long-range Coulomb potential Eq. (4.5) is calculated between all charges using the multigrid PPPM method.[208] The fluid flow is driven by an external electrical field E_x along the x direction. The results presented are evaluated by averaging over 1600τ at steady state and up to 80 independent simulations. For comparison we also show

simulations of Poiseuille-type flow produced by applying a constant gravity force G_x to all molecules (and $F_{ad,x} = G_x\rho$ for Eq. (4.21) in the bulk subdomain).

Figure 4.8 shows the mean profiles of the charge distribution n_e as a function of height y for Bjerrum length $\lambda_B = 2.55\sigma$ and 0.64σ. Figure 4.9 shows a closeup of the region near the wall. As in past studies,[94,187,208,241–244] the ion concentration [Figure 4.9(a)] shows oscillations within 3 to 4 atomic diameters from wall. This is due to the discrete nature of the particles and can be associated with layering of solvent molecules [Figure 4.9(b)] with a period set by the preferred molecular spacing.[22,25,95,148–157] The ion concentration is highest at the peak associated with the first fluid layer and then decays rapidly with distance from the wall. Note that the hybrid method accurately reproduces the full MD results over the entire domain as the density varies by almost 4 orders of magnitude. This large density change is one of the challenges to single scale methods.

Also shown is the continuum prediction from the solution of the Poisson-Boltzmann equation (PBE):

$$n_e(\tilde{y}) = \frac{n_{e,o}}{\cos^2(\tilde{y})}, \tag{4.49}$$

where the concentration at the mid-plane $n_{e,o}$ is fixed by the total number of charges, $\tilde{y} \equiv (y - L_y/2)/\sqrt{2}\lambda_D$, and λ_D is the Debye screening length:

$$\lambda_D = \sqrt{\frac{\epsilon_0\epsilon_r k_B T}{n_{e,o}e^2}} = \frac{1}{\sqrt{4\pi n_{e,o}\lambda_B}} \quad . \tag{4.50}$$

The PBE makes a mean-field approximation that ignores direct correlations between

ions.[245–250] Since the interaction between ions equals the thermal energy k_BT when they are separated by the Bjerrum length, the PBE is accurate when $n_e\lambda_B^3 << 1$.[247,251–256] Modified PB models have been developed to include the electrostatic interaction between charges,[247,248,255] but these improvements still neglect the atomic size of the charges and solvent molecules.

The continuum solution provides a reasonable description of the atomistc results in Figures 4.8 and 4.9(a) for $\lambda_B = 0.64\sigma$ where $n_e\lambda_B^3 < 0.08$. The main difference is that continuum theory does not capture the layering near the wall. The continuum prediction is wrong by a factor of 2 or more for $\lambda_B = 2.55\sigma$ where $n_e\lambda_B^3 > 10$. Based on previous results,[247] deviations from the PBE equations become important for water when the surface charge density is larger than 0.1e/nm^2 and we now show that this may lead to significant errors in continuum predictions for electroosmotic flow.

Figures 4.10,4.11 and 4.12 show that the hybrid method accurately reproduces full MD results for electroosmotic flow and constant force flow (Poiseuille type). Both the mean fluid velocity and the mean velocity of the ions are shown. In all cases the solutions from MD and SELM regions of the hybrid simulation are consistent and continuous through the overlap region. They are also within statistical errors of the full MD simulation. This level of agreement is only obtained because the overlap region smoothly couples the continuum and discrete descriptions of the solvent and the SELM provides an accurate model of ion motion in the bulk subdomain.

The difference between ion velocities and the mean flow profile in the bulk region

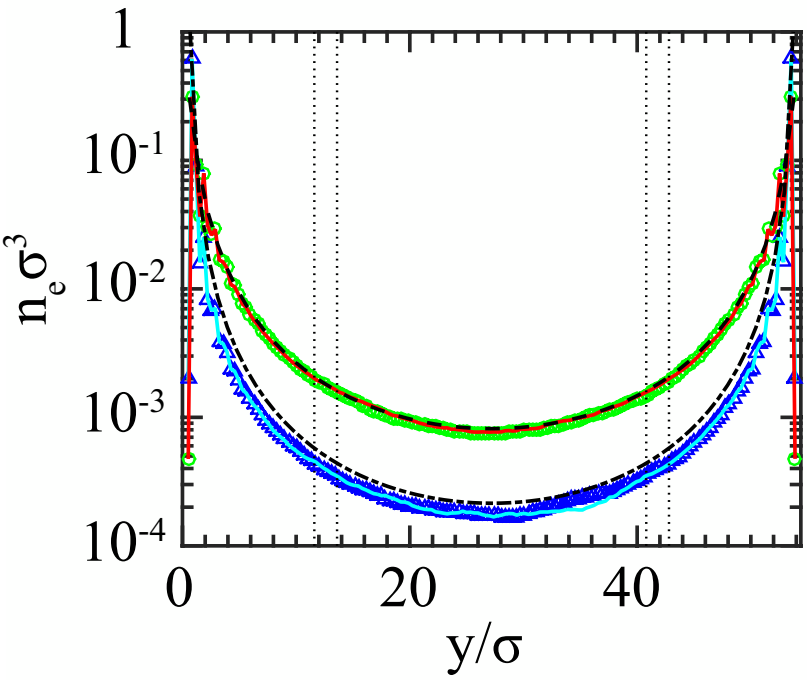

Figure 4.8: Mean concentration profiles of charges n_e as a function of height y in the channel used to study planar electroosmotic flows. The blue triangles, and cyan solid and black dashed dotted lines represent the full MD, hybrid and analytical PB results for $\lambda_B = 2.55\sigma$. The green circles, red solid and black dashed lines represent the full MD, hybrid and PB results for $\lambda_B = 0.64\sigma$. The vertical black dotted lines indicate the positions of y_{MD} and y_{SELM}. The boundaries of the y axis indicate the positions of the wall surfaces.

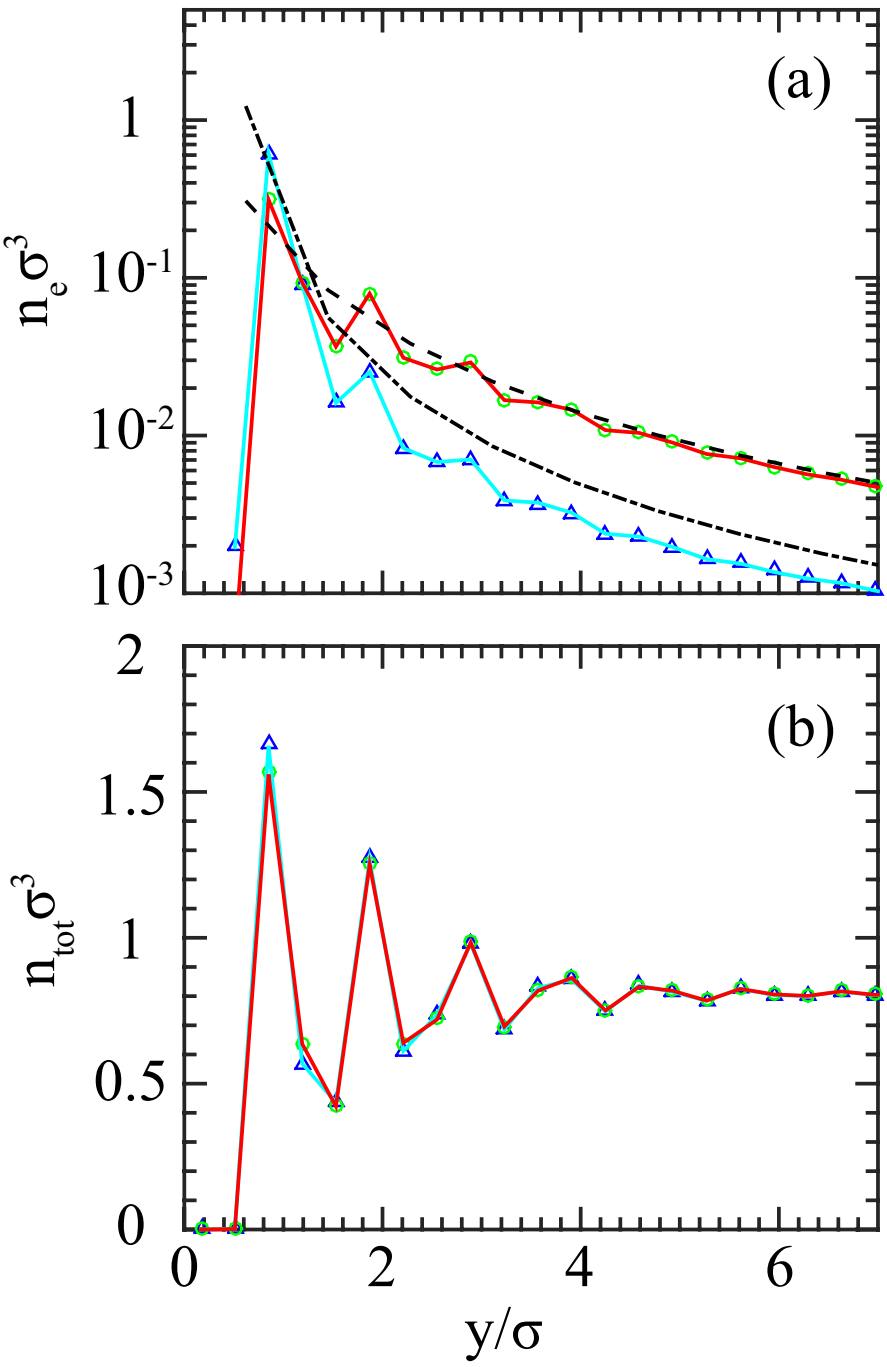

Figure 4.9: Close up views of (a) the mean charge concentration n_e and (b) the total number density n_{tot} as a function of y for the same systems presented in Figure 4.8. The blue triangles, cyan solid and black dashed dotted lines represent the full MD, hybrid and analytical PB results for $\lambda_B = 2.55\sigma$. The green circles, red solid and black dashed lines represent the full MD, hybrid and PB results for $\lambda_B = 0.64\sigma$, respectively.

provides a simple estimation for the effective mobility of the charges. The force from the electric field on each ion is balanced by the drag from the surrounding fluid in steady-state. The measured effective mobility is about 10 percent larger than the value associated with the bare coefficient $1/\Gamma_{bare}$ [Eq. (4.9)], and it grows slowly as y increases from 0 to the channel center. This is consistent with the SELM model. The extra mobility is associated with hydrodynamic effects from the continuum flow field, which influence the ions' dynamics through the reference velocity $\boldsymbol{U}_{ref}$.[124,217] This phenomena is related to the system-size dependent diffusion found in Figure 4.5.

The SELM description assumes the system is sufficiently near equilibrium that linear response theory can be used. Figure 4.12 shows that the description remains accurate even when the relative mean velocity of ions reaches about 20 percent of the thermal speed. Further increasing E_x by a factor of 2 leads to disagreement in the mean velocity profile of the charges in the bulk, mainly due to the failure of the SELM approach. Note that non-linear behavior is already present in the MD region of Figure 4.12 and is only captured because a full atomistic treatment is included. As shown previously,[22,23,94,208] non-Newtonian effects arise when the shear rate exceeds about $0.1/\tau$ and this applies to the first 3 fluid layers in the figure. The high shear rate also leads to significant energy dissipation and temperature rise ($\sim 10\%$) near the wall.

Continuum theories for flow require additional input in the form of boundary conditions at the solid wall. The most common is the Navier slip boundary condi-

tion that assumes the jump in transverse velocity at the fluid-solid interface, ΔU, is proportional to the shear stress.[21,257] In the Newtonian limit, this can be written as

$$L_s \frac{d}{dn} U = \Delta U \tag{4.51}$$

where L_s is the slip length and n denotes the normal direction (pointing into the fluid) of the surface. We determined L_s from separate MD simulations using standard methods.[22,27,161,162,176] Planar shear (Couette) flow was imposed on the charged fluid with $\lambda_B = 2.55\sigma$ in the same geometry used for electroosmotic studies. The resulting mean flow profiles were fit to the linear Couette solution. The fit velocity goes to zero at $y = 0.62\sigma$ while the first fluid layer is centered at about $y = 0.85\sigma$. Fluid layering introduces some ambiguity in where ΔU should be defined. We plot results for $L_s = 0$ and take 0.62σ as the reference plane where Eq. 4.51 is applied. Sensitivity to changes in the reference plane are discussed at the end of this section.

The continuum electroosmotic flow profile is obtained using the force from the electric field on the equilibrium PBE charge density [Eq. (4.49)] and the Navier-Stokes equations with a Navier slip boundary condition. The resulting velocity profile is:

$$U_x(\tilde{y}) = \frac{E_x e}{4\pi\mu\lambda_B}\{\log[\cos^2(\tilde{y}_{bc})] - \log[\cos^2(\tilde{y})] + 2\tilde{L}_s \tan(\tilde{y}_{bc})\}, \tag{4.52}$$

where $\tilde{y}_{bc} = L/2\sqrt{2}\lambda_D$ is the value at the boundary and $\tilde{L}_s = L_s/\sqrt{2}\lambda_D$.

Figure 4.10 contrasts the flow profiles for electroosmotic and gravitational flow. The constant gravitational force was set to $G_x = 0.00035\epsilon/m\sigma$, so that the two profiles

correspond to about the same net mass flow rate. For planar flow the second derivative of the velocity is proportional to the local force. Since the gravitational force is uniform, the flow profile has a simple parabolic form. In contrast, the high density of charge at the walls leads to a correspondingly high curvature for electroosmotic flow. The profile becomes almost pluglike in the central region where the charge density is orders of magnitude smaller. For the case shown, the fluid velocity reaches half of the peak velocity by the first fluid layer at $y = 0.85\sigma$. Any small change in charge density or flow boundary condition has a profound affect on the near-wall velocity rise that propagates across the entire channel. The width of the charge distribution is set by the screening length rather than the channel width, and the extreme sensitivy to charge density near the wall remains even for wide channels.

The continuum solution for gravity driven flow in Figure 4.10 provides an accurate description of the hybrid and full MD solutions. In contrast, the prediction for electroosmotic flow is lower near the wall and significantly higher in the central region. The PB solution overestimates the charge concentration over the whole domain outside the first fluid layer (Figure 4.8). Since the force is proportional to the local curvature in the velocity, spreading the same force over a wider height range produces a larger net change in velocity.

Figure 4.11 shows the velocity profile for $\lambda_B = 0.644\sigma$ where continuum theory gave the correct charge density. There is a correspondingly accurate description of the flow profile. Note that decreasing λ_B leads to a larger screening length. Since the

charge is spread farther from the wall, the force is more spread out and the net flux is increased almost 4-fold compared to Figure 4.10.

The rapid change in velocity near the wall makes the electroosmotic flow profile very sensitive to slip boundary condition. As noted above, the slip boundary condition depends on the plane at which the condition is applied, which is uncertain on the scale of the layer separation ($\sim \sigma$).[134,176] Gravity driven flow is barely affected by such small shifts in the position of the reference plane, but large changes can be produced in electroosmotic flow. For example in the examples above we took the boundary of the fluid to be at the height 0.62σ where the Couette velocity reached zero. Shifting the reference plane to the height of the first fluid layer at 0.85σ implies a small slip length $L_s = 0.23\sigma$. This slight shift in boundary condition increases the peak flow velocity from the continuum solution by 10% for $\lambda_B = 0.64\sigma$ and 25% for $\lambda_B = 2.55\sigma$. This extreme sensitivity is an important motivation for our hybrid approach which uses a complete atomistic treatment at the wall that captures all affects from fluid boundary conditions, layering, and charge distribution.

4.3.6 Electroosmotic Flow in Channels with Sinusoidal Corrugations

In this subsection, we further demonstrate the performance of our hybrid scheme in systems with more complicated geometries. Sinusoidal corrugations are added to the solid walls used in the previous section with all other parameters kept fixed. As illustrated in Figure 4.13 two different methods are used to generate the sinusoidal corrugations in the atomic walls, resulting in two types of surfaces. In both cases the

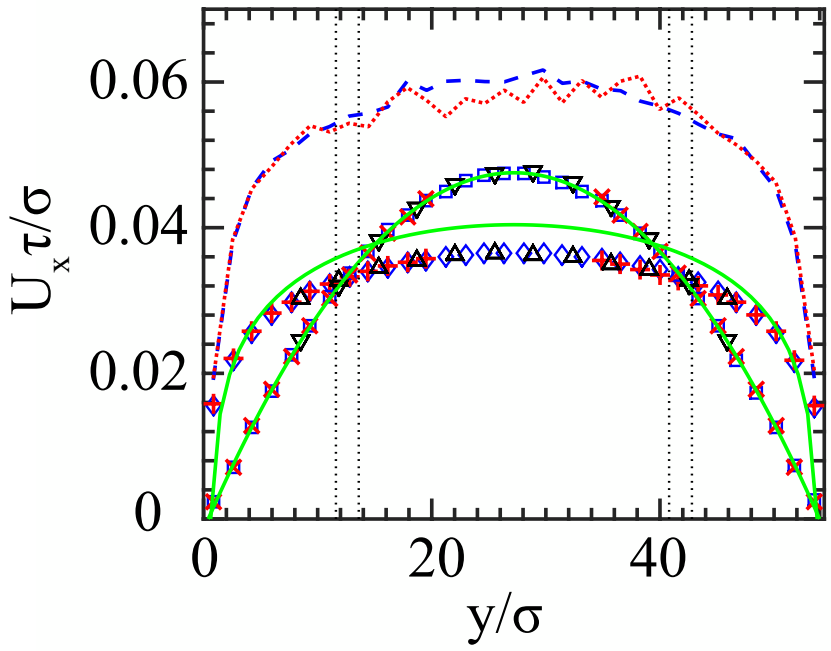

Figure 4.10: Mean flow profiles for electroosmotic flow with $\lambda_B = 2.55\sigma$ and $E_x = 0.32\epsilon/\sigma e$ and gravity force driven flow with $G_x = 0.00035\epsilon/m\sigma$. The blue diamonds, red pluses and black up-pointed triangles represent the full MD, hybrid MD and hybrid continuum results for electroosmotic flow. The blue squares, red crosses and black down-pointed triangles represent the full MD, hybrid MD and hybrid continuum results for gravity driven flow. Each hybrid continuum data point corresponds to the mean velocity over the whole row of cells at each given height. Each of the full MD and hybrid MD data points is averaged over a slab with a thickness equal to half a continuum cell $h/2 = 1.7\sigma$. Note that the data point closest to the wall corresponds approximately to the first fluid layer above the surface. The mean velocities of the charges in electroosmotic flow are also averaged within these small slabs and plotted as blue dashed (full MD) and red dotted (hybrid) curves. The continuum analytical solutions are plotted as green solid curves. The vertical black dotted lines indicate the positions of y_{MD} and y_{SELM}. The boundaries of the y axis indicate the positions of the wall surfaces.

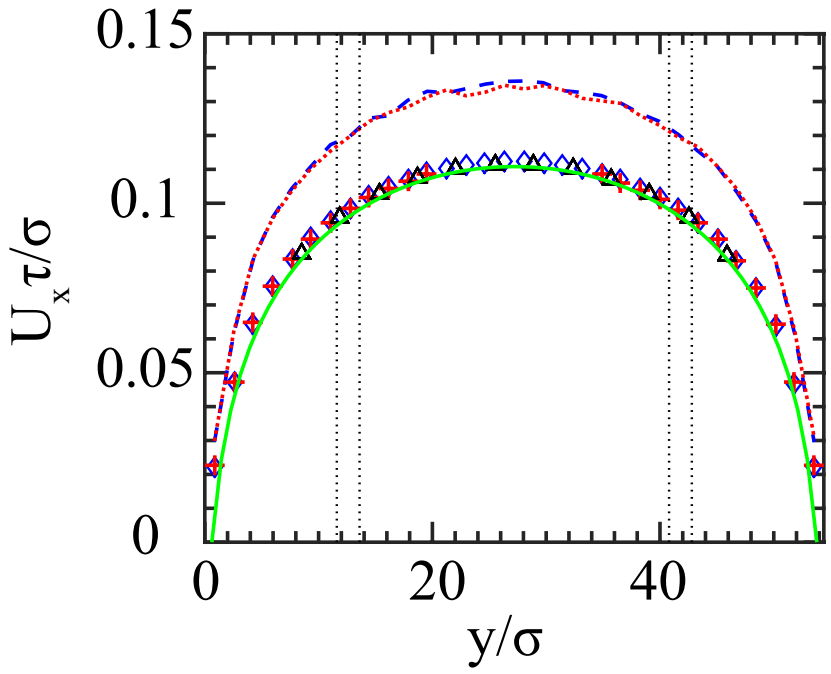

Figure 4.11: Mean flow profiles for electroosmotic flow with $\lambda_B = 0.64\sigma$ and $E_x = 0.32\epsilon/\sigma e$. The blue diamonds, red pluses and black up-pointed triangles represent the full MD, hybrid MD and hybrid continuum results for electroosmotic flow. Each hybrid continuum data point corresponds to the mean velocity over the whole row of cells at each given height. Each of the full MD and hybrid MD data points is averaged over a slab with thickness $h/2 = 1.7\sigma$. Note that the data point closest to the wall corresponds approximately to the first fluid layer. The mean velocities of the charges in electroosmotic flow are also averaged within these small slabs and plotted as blue dashed (full MD) and red dotted (hybrid) curves. The continuum analytical solutions are plotted as green solid curves. The vertical black dotted lines indicate the positions of y_{MD} and y_{SELM}. The boundaries of the y axis indicate the positions of the wall surfaces.

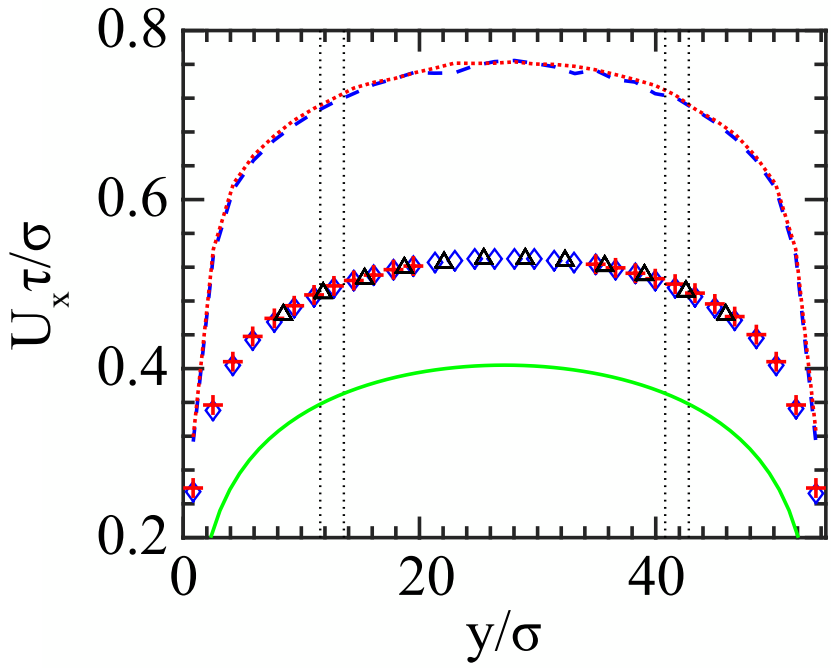

Figure 4.12: Mean flow profiles for electroosmotic flow with $\lambda_B = 2.55\sigma$ and $E_x = 3.2\epsilon/\sigma e$. The blue diamonds, red pluses and black up-pointed triangles represent the full MD, hybrid MD and hybrid continuum results for electroosmotic flow. Each hybrid continuum data point corresponds to the mean velocity over the whole row of cells at each given height. Each of the full MD and hybrid MD data points is averaged over a slab with thickness $h/2 = 1.7\sigma$. Note that the data point closest to the wall corresponds approximately to the first fluid layer. The mean velocities of the charges in electroosmotic flow are also averaged within these small slabs and plotted as blue dashed (full MD) and red dotted (hybrid) curves. The continuum analytical solutions are plotted as green solid curves. The vertical black dotted lines indicate the positions of y_{MD} and y_{SELM}. The boundaries of the y axis indicate the positions of the wall surfaces.

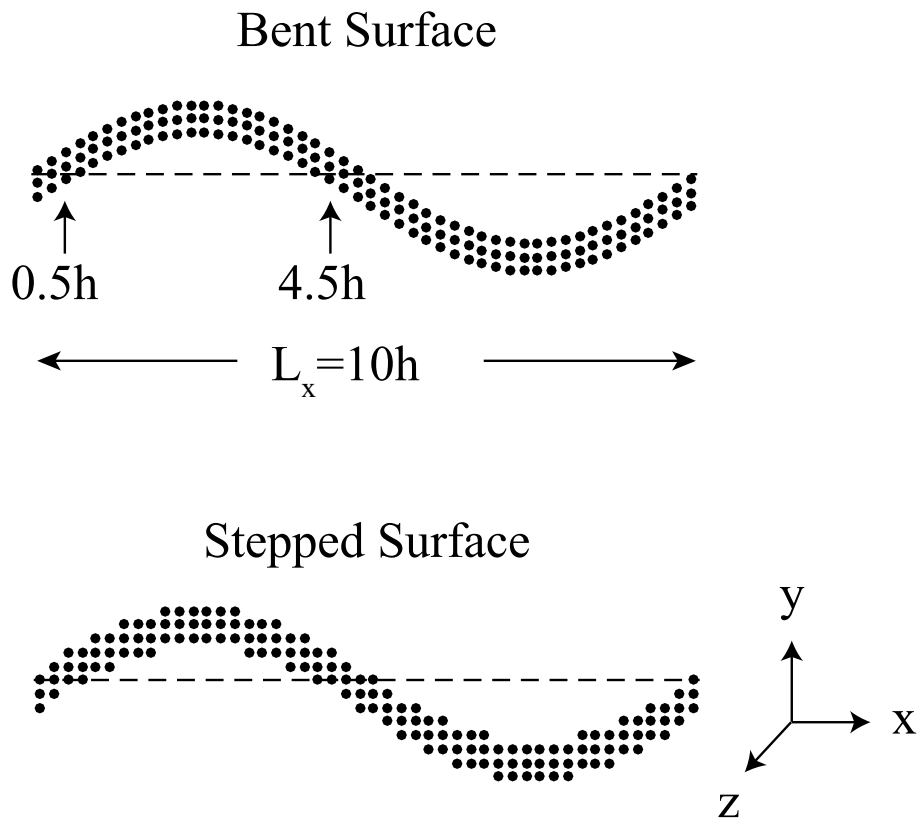

Figure 4.13: Sinusoidal wall surfaces at the channel bottom with two different atomic geometries: (upper) bent surface; (lower) stepped surface. The horizontal dashed lines denote the height $y = 0\sigma$ for reference. Arrows indicate the values of x where the vertical velocity profile is shown in Figure 4.15 and h is the width of the cells used in the continuum domain.

top and bottom walls are mirror images of each other about the plane at the channel center $y = L_y/2$.

Bent surfaces are constructed by displacing the solid atoms of the bottom wall by a height

$$y_s(x) = A_s \sin(\frac{2\pi x}{\lambda_s}). \tag{4.53}$$

where A_s and λ_s are the amplitude and wavelength of the sinusoidal roughness, respectively. The mean height of the outer layer of surface atoms is maintained at $y = 0$.

Stepped surfaces are created by cutting a crystalline surface rather than displacing atoms. Atoms of the original crystal are removed if their initial height is above $y_s(x)$. Special care is taken so that the mean height of the outer surface atoms is at $y = 0$. The stepped surface approximates the sinusoidal profile by a series of discrete steps at sharp edges and may be more representative of rough crystal surfaces.

As for planar electroosmotic flows, $N_e = 160$ ions with unit charge are placed at random positions. Solid atoms at the surfaces are charged uniformly to ensure that the system is electrically neutral. The dielectric constant is set so $\lambda_B = 2.55\sigma$, and the external electric field is $E_x = 0.32\epsilon/e\sigma$. For comparison, the results of the gravity driven flow with $G_x = 0.00035\epsilon/m\sigma$ are also presented.

Figures 4.14 and 4.15 illustrate the velocity profiles for flow over a bent surface with wavelength $\lambda_s = L_x = 34\sigma$ and amplitude $A_s = 5a_y = 3.54\sigma$, where $a_y = 0.71\sigma$ is the distance between the (001) layers of the FCC crystal of the original planar

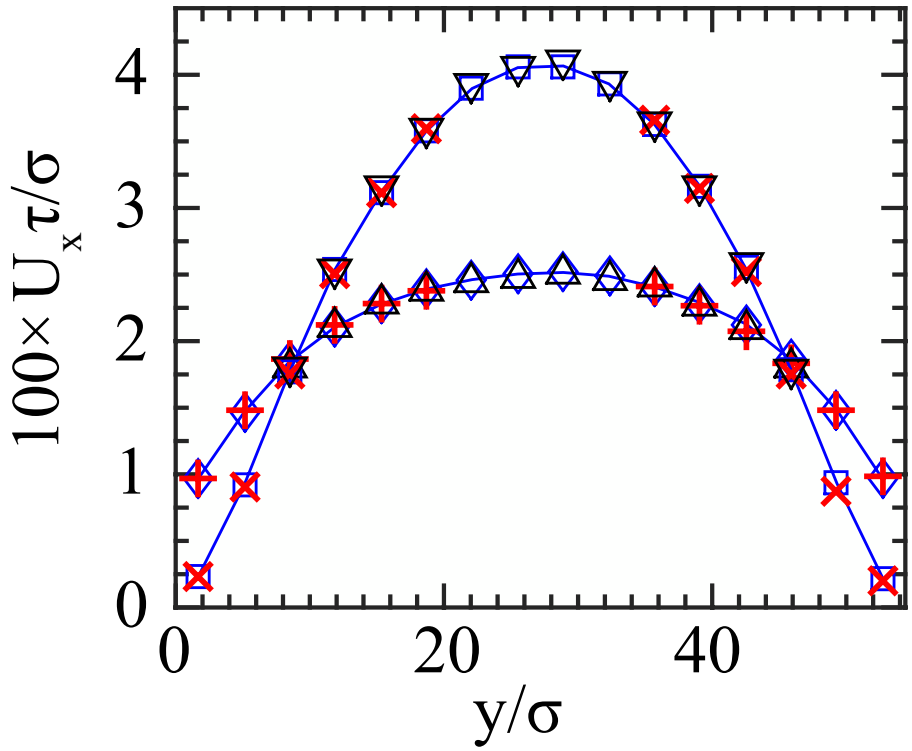

Figure 4.14: Profiles of the horizontal velocity U_x for bent surfaces with $A_s = 3.54\sigma$ and $\lambda_s = 34\sigma$. The flow varies with x and is shown for $x = 0\sigma$. The blue diamonds, red pluses and black up-pointed triangles represent the full MD, hybrid MD and hybrid continuum results for electroosmotic flow with $\lambda_B = 2.55\sigma$ and $E_x = 0.32\epsilon/\sigma e$. The blue squares, red crosses and black down-pointed triangles represent the full MD, hybrid MD and hybrid continuum results for gravity driven flow with $G_x = 0.00035\epsilon/m\sigma$. Each of the full MD and hybrid MD data points is defined according to the continuum grid for U_x and represents the mean velocity within the volume of a continuum cell. The boundaries of the y axis indicate the mean heights of the wall surfaces.

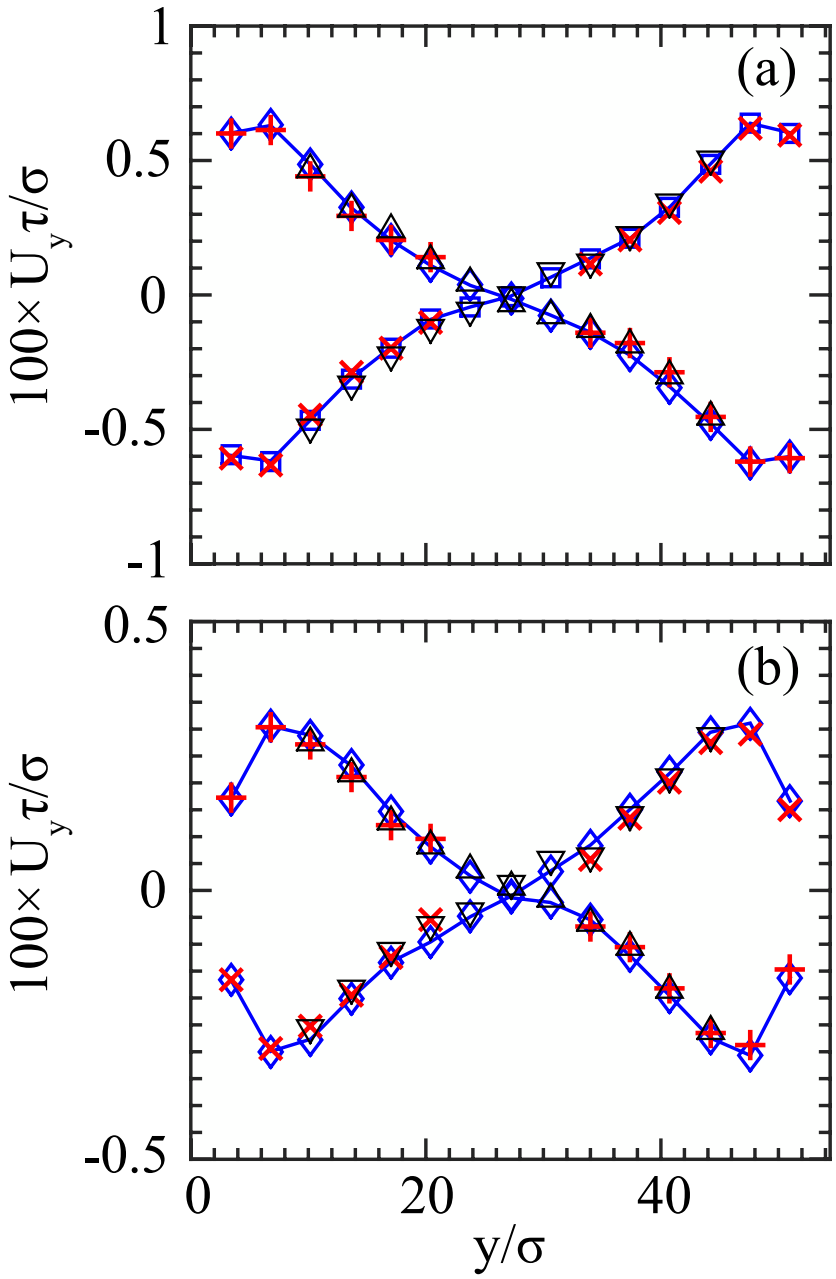

Figure 4.15: Profiles of the vertical velocity U_y for bent surfaces with $A_s = 3.54\sigma$ and $\lambda_s = 34\sigma$ for (a) electroosmotic flow with $\lambda_B = 2.55\sigma$ and $E_x = 0.32\epsilon/\sigma e$ and (b) gravity driven flow with $G_x = 0.00035\epsilon/m\sigma$. The blue diamonds, red pluses and black up-pointed triangles represent the full MD, hybrid MD and hybrid continuum velocities at $x = h/2 = 1.7\sigma$ based on the staggered mesh of the continuum solver. The blue squares, red crosses and black down-pointed triangles represent the full MD, hybrid MD and hybrid continuum results at $x = 4.5h = 15.3\sigma$.

wall. The curved surface leads to two-dimensional flows, thus we can further test the performance of our hybrid scheme under a situation with consistent mean flows across the overlap region. Once again, hybrid results are smooth and continuous through the transition from MD to SELM regimes and show a remarkable agreement with full MD results. Similar accuracy was found in all cases considered.

Figure 4.15 shows vertical velocity profiles for the y-z planes at $x = 0.5h$ and $x = 4.5h$ (as marked in Figure 4.13). The profiles display a nice symmetry about the positions of the wave crest at $x = 2.5h$, showing that the flows are well into the Stokes regime.[258] Curving the surface generates a larger vertical velocity for electroosmotic flow than for gravity driven flow. Since the electroosmotic driving force is concentrated close to the wall rather than being uniformly spread, a larger portion of the fluid is driven to climb over the surface corrugations, leading to a larger energy dissipation. As a result, the surface corrugation produces a greater relative reduction in the net flow rate for the electroosmotic flows,[208] as shown in Figures 4.16 and 4.17.

Figure 4.16 shows the variation of net mass flow rate:

$$Q = \int \rho U_x(y) dy \tag{4.54}$$

for gravity driven and electroosmotic flow over bent and stepped surfaces as a function of the amplitude A_s for wavelength $\lambda_s = L_x$. The electroosmotic flow rate drops by more than 40 percent as the amplitude increases to $A_s = 5a_y = 3.54\sigma$. Stepped sur-

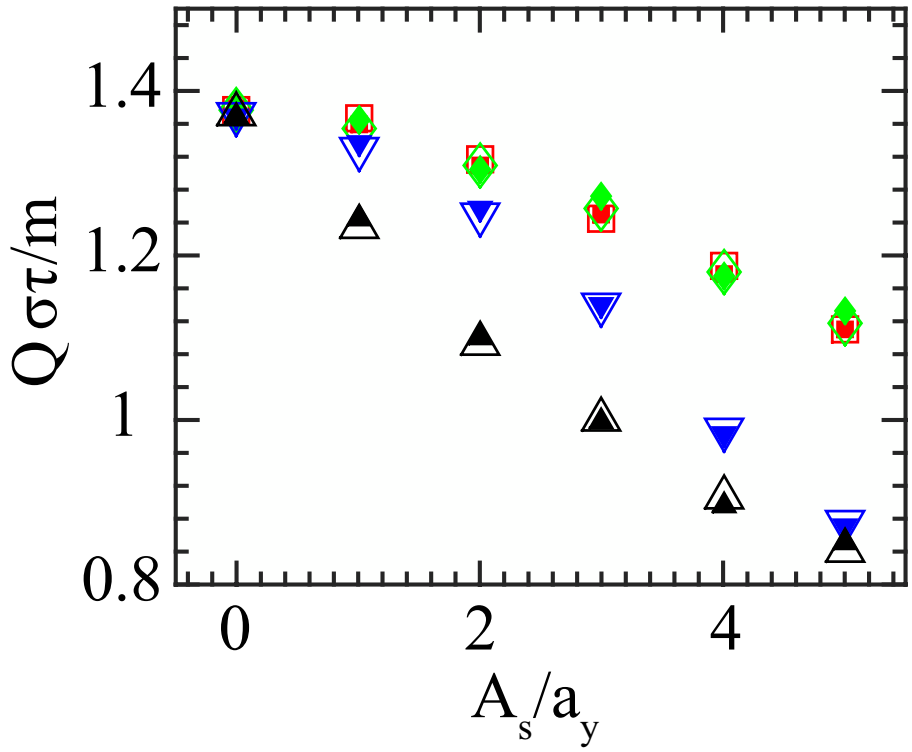

Figure 4.16: Mass flow rate as a function of the amplitude A_s normalized by the interlayer distance a_y with constant wavelength $\lambda_s = 34\sigma$ for both the electroosmotic (triangles) and gravity driven (diamonds and squares) flows. The symbol orientation indicates the type of surface: bent (squares and down-pointed triangles) or stepped (diamonds and up-pointed triangles). The hybrid and full MD results are represented by the solid and open symbols, respectively.

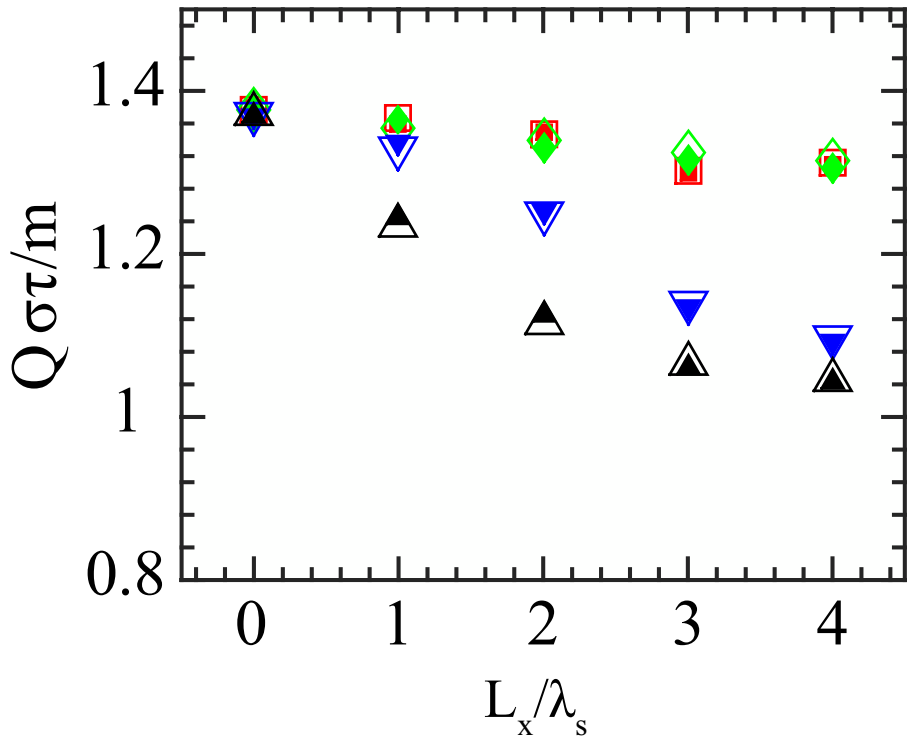

Figure 4.17: Mass flow rate as a function of L_x/λ_s with constant amplitude $A_s = a_y = 0.81\sigma$, for both electroosmotic (triangles) and gravity driven (diamonds and squares) flows. The symbol orientation indicates the type of the surface: bent (squares and down-pointed triangles) or stepped (diamonds and up-pointed triangles). The hybrid and full MD results are represented by the solid and open symbols, respectively.

faces produce a faster initial reduction in Q because of the increased drag associated with the step edges. Their impact is pronounced because the charges contributing most to the driving force are in the first fluid layer where they are easily trapped by edges. The difference is suppressed at large amplitudes where the spacing between step edges approaches the lattice constant and new facets are generated. Very similar affects are seen in Figure 4.17 where the amplitude is fixed at $A_s = a_y = 0.71\sigma$ and the number of wavelengths per system size, L_x/λ_s is varied. As found in Ref. [208], the effect of roughness is reduced as the wavelength increases, and tends to saturate at large λ_s,

As mentioned above, the gravity driven flow rate decreases much more slowly with increasing roughness. The effects of the variation in A_s and λ_s has been studied both analytically[29,38,180–182] and numerically.[35,36,44] It has been shown that Q decreases linearly with A_s^2/λ_s when A_s is small and with A_s when A_s is large. We find our results for $A_s \lesssim 2a_y$ and $A_s \gtrsim 2a_y$ correspond well to the former and the latter predictions, respectively. Note that the difference between bent and stepped surfaces is also suppressed. Once again the lower fluid velocity and velocity gradient make gravity driven flow less sensitive to surface details.

The difference between stepped and bent surfaces highlights the importance of atomic details at the solid surface in determining electroosmotic flows. Accurately coupling a fully-resolved near-wall molecular dynamics simulation with well modeled bulk dynamics is the only way of ensuring that these details are completely captured.

The results presented in this section show that our hybrid scheme achieves this goal and demonstrates a remarkable agreement with full MD simulations.

4.4 Summary and Conclusions

In this work, we have developed a multi-scale hybrid scheme to simulate electroosmotic flows. Following the idea of domain decomposition,[97,98,192] molecular dynamics is used in the near-wall subdomain where the atomistic details are important, while the continuum hydrodynamics are solved in the remaining bulk region. The two descriptions are coupled in a finite overlap region. Charges are included in the simulations and their long-range electrostatic interactions are solved with a multi-grid particle-particle particle-mesh method[208] throughout the entire domain. A discrete description of ions is retained in the continuum bulk region because of the low density of ions and the long-range of electrostatic interactions. A stochastic Euler-Lagrangian method is used to simulate the dynamics of these ions coupled to an implicit continuum fluid. Thermal fluctuations are incorporated in the continuum hydrodynamics, so that the diffusive transport of the SELM ions can be accurately matched to the MD description. The SELM and MD descriptions seamlessly exchange ions in the middle of the overlap region.

The hybrid approach is validated against full molecular dynamics simulations for different geometries and types of flows. A subject for our future studies will be extending this approach to larger systems for practical applications. The computa-

tional cost of the current hybrid simulation is roughly that of computing the LJ and Coulomb interactions for the particles. The former is proportional to the size of the MD domain. The calculation of the Coulomb potential involves solving a Poisson equation over the entire domain,[208] and the cost increases with the total system size. However, this can be sped up by using a spatially adaptive mesh with fine grids only in the near-wall region where the charge density is high, which can be naturally implemented through the multigrid PPPM method.[208] The continuum hydrodynamic solver can be accelerated in the same manner when necessary.[100,259]

Bibliography

[1] H. A. Stone, A. D. Stroock, and A. Ajdari, "Engineering flows in small devices: microfluidics toward a lab-on-a-chip."

[2] T. M. Squires and S. R. Quake, "Microfluidics: Fluid physics at the nanoliter scale," *Rev. Mod. Phys.*, vol. 77, no. 3, p. 977, 2005.

[3] W. Sparreboom, A. Van Den Berg, and J. Eijkel, "Transport in nanofluidic systems: a review of theory and applications," *New J. Phys.*, vol. 12, no. 1, p. 015004, 2010.

[4] R. B. Schoch, J. Han, and P. Renaud, "Transport phenomena in nanofluidics," *Rev. Mod. Phys.*, vol. 80, no. 3, p. 839, 2008.

[5] J. C. Eijkel and A. Van Den Berg, "Nanofluidics: what is it and what can we expect from it?" *Microfluid. Nanofluid.*, vol. 1, no. 3, pp. 249–267, 2005.

[6] E. Lauga, M. Brenner, and H. Stone, "Microfluidics: the no-slip boundary condition," in *Springer Handbook of Experimental Fluid Mechanics*. Springer, 2007, pp. 1219–1240.

[7] C. Neto, D. R. Evans, E. Bonaccurso, H.-J. Butt, and V. S. Craig, "Boundary slip in newtonian liquids: a review of experimental studies," *Rep. Prog. Phys.*, vol. 68, no. 12, p. 2859, 2005.

BIBLIOGRAPHY

[8] T. Lee, E. Charrault, and C. Neto, "Interfacial slip on rough, patterned and soft surfaces: A review of experiments and simulations," *Adv. Colloid Interf.*, vol. 210, pp. 21–38, 2014.

[9] O. I. Vinogradova, "Slippage of water over hydrophobic surfaces," *Int. J. of Miner. Process*, vol. 56, no. 1, pp. 31–60, 1999.

[10] E. Schnell, "Slippage of water over nonwettable surfaces," *J. Appl. Phys.*, vol. 27, no. 10, pp. 1149–1152, 1956.

[11] J. Baudry, E. Charlaix, A. Tonck, and D. Mazuyer, "Experimental evidence for a large slip effect at a nonwetting fluid-solid interface," *Langmuir*, vol. 17, no. 17, pp. 5232–5236, 2001.

[12] U.-C. Boehnke, T. Remmler, H. Motschmann, S. Wurlitzer, J. Hauwede, and T. M. Fischer, "Partial air wetting on solvophobic surfaces in polar liquids," *J. Colloid Interf. Sci.*, vol. 211, no. 2, pp. 243–251, 1999.

[13] C. Cottin-Bizonne, B. Cross, A. Steinberger, and E. Charlaix, "Boundary slip on smooth hydrophobic surfaces: Intrinsic effects and possible artifacts," *Phys. Rev. Lett.*, vol. 94, no. 5, p. 056102, 2005.

[14] C. Cottin-Bizonne, S. Jurine, J. Baudry, J. Crassous, F. Restagno, and E. Charlaix, "Nanorheology: an investigation of the boundary condition at hydrophobic and hydrophilic interfaces," *Eur. Phys.l J. E*, vol. 9, no. 1, pp. 47–53, 2002.

BIBLIOGRAPHY

[15] V. S. Craig, C. Neto, and D. R. Williams, "Shear-dependent boundary slip in an aqueous newtonian liquid," *Phys. Rev. Lett.*, vol. 87, no. 5, p. 054504, 2001.

[16] H. Hervet and L. Léger, "Flow with slip at the wall: from simple to complex fluids," *Comptes Rendus Physique*, vol. 4, no. 2, pp. 241–249, 2003.

[17] C. Neto, V. Craig, and D. Williams, "Evidence of shear-dependent boundary slip in newtonian liquids," *Eur. Phys.l J. E*, vol. 12, no. 1, pp. 71–74, 2003.

[18] R. Pit, H. Hervet, and L. Léger, "Direct experimental evidence of slip in hexadecane: solid interfaces," *Phys. Rev. Lett.*, vol. 85, no. 5, p. 980, 2000.

[19] E. Bonaccurso, M. Kappl, and H.-J. Butt, "Hydrodynamic force measurements: boundary slip of water on hydrophilic surfaces and electrokinetic effects," *Phys. Rev. Lett.*, vol. 88, no. 7, p. 076103, 2002.

[20] Y. Zhu and S. Granick, "No-slip boundary condition switches to partial slip when fluid contains surfactant," *Langmuir*, vol. 18, no. 26, pp. 10 058–10 063, 2002.

[21] C. Navier, "Mémoire sur les lois du mouvement des fluides," *Mémoires de lAcadémie Royale des Sciences de lInstitut de France*, vol. 6, pp. 389–440, 1823.

[22] P. A. Thompson and M. O. Robbins, "Shear flow near solids: epitaxial order and flow boundary conditions," *Phys. Rev. A*, vol. 41, no. 12, p. 6830, 1990.

[23] P. A. Thompson and S. M. Troian, "A general boundary condition for liquid flow at solid surfaces," *Nature*, vol. 389, no. 6649, pp. 360–362, 1997.

[24] M. Cieplak, J. Koplik, and J. R. Banavar, "Boundary conditions at a fluid-solid interface," *Phys. Rev. Lett.*, vol. 86, no. 5, p. 803, 2001.

[25] T.-M. Galea and P. Attard, "Molecular dynamics study of the effect of atomic roughness on the slip length at the fluid-solid boundary during shear flow," *Langmuir*, vol. 20, no. 8, pp. 3477–3482, 2004.

[26] N. V. Priezjev, "Effect of surface roughness on rate-dependent slip in simple fluids," *J. Chem. Phys.*, vol. 127, no. 14, p. 144708, 2007.

[27] N. Priezjev, "Rate-dependent slip boundary conditions for simple fluids," *Phys. Rev. E*, vol. 75, no. 5, p. 051605, 2007.

[28] D. Einzel, P. Panzer, and M. Liu, "Boundary condition for fluid flow: curved or rough surfaces," *Phys. Rev. Lett.*, vol. 64, no. 19, p. 2269, 1990.

[29] P. Panzer, M. Liu, and D. Einzel, "The effects of boundary curvature on hydrodynamic fluid flow: calculation of slip lengths," *Int. J. Mod. Phys. B*, vol. 6, no. 20, pp. 3251–3278, 1992.

[30] K. Falk, F. Sedlmeier, L. Joly, R. R. Netz, and L. Bocquet, "Molecular origin of fast water transport in carbon nanotube membranes: Superlubricity versus curvature dependent friction," *Nano Lett.*, vol. 10, no. 10, pp. 4067–4073, 2010.

[31] K. Falk, F. Sedlmeier, L. Joly, R. Netz, and L. Bocquet, "Ultralow liquid/solid friction in carbon nanotubes: comprehensive theory for alcohols, alkanes, omcts, and water," *Langmuir*, vol. 28, no. 40, pp. 14 261–14 272, 2012.

[32] W. Chen, R. Zhang, and J. Koplik, "Velocity slip on curved surfaces," *Phys. Rev. E*, vol. 89, no. 2, p. 023005, 2014.

[33] M. Cieplak, E. D. Smith, and M. O. Robbins, "Molecular origins of friction: The force on adsorbed layers," *Science*, vol. 265, no. 5176, pp. 1209–1212, 1994.

[34] E. D. Smith, M. O. Robbins, and M. Cieplak, "Friction on adsorbed monolayers," *Phys. Rev. B*, vol. 54, no. 11, p. 8252, 1996.

[35] N. V. Priezjev and S. M. Troian, "Influence of periodic wall roughness on the slip behaviour at liquid/solid interfaces: molecular-scale simulations versus continuum predictions," *J. Fluid Mech.*, vol. 554, pp. 25–46, 2006.

[36] A. Niavarani and N. V. Priezjev, "The effective slip length and vortex formation in laminar flow over a rough surface," *Phys. Fluids*, vol. 21, no. 5, p. 052105, 2009.

[37] A. Niavarani and N. Priezjev, "Modeling the combined effect of surface roughness and shear rate on slip flow of simple fluids," *Phys. Rev. E*, vol. 81, no. 1, p. 011606, 2010.

[38] K. Kamrin, M. Z. Bazant, and H. A. Stone, "Effective slip boundary conditions

for arbitrary periodic surfaces: the surface mobility tensor," *J. Fluid Mech.*, vol. 658, pp. 409–437, 2010.

[39] E. Lauga and H. A. Stone, "Effective slip in pressure-driven stokes flow," *J. Fluid Mech.*, vol. 489, pp. 55–77, 2003.

[40] K. Sarkar and A. Prosperetti, "Effective boundary conditions for stokes flow over a rough surface," *J. Fluid Mech.*, vol. 316, pp. 223–240, 1996.

[41] S. Granick, Y. Zhu, and H. Lee, "Slippery questions about complex fluids flowing past solids," *Nature Mater.*, vol. 2, no. 4, pp. 221–227, 2003.

[42] Y. Zhu and S. Granick, "Limits of the hydrodynamic no-slip boundary condition," *Phys. Rev. Lett.*, vol. 88, no. 10, p. 106102, 2002.

[43] C. Kunert, J. Harting, and O. I. Vinogradova, "Random-roughness hydrodynamic boundary conditions," *Phys. Rev. Lett.*, vol. 105, no. 1, p. 016001, 2010.

[44] C. Kunert and J. Harting, "Roughness induced boundary slip in microchannel flows," *Phys. Rev. Lett.*, vol. 99, no. 17, p. 176001, 2007.

[45] J. Harting, C. Kunert, and J. Hyväluoma, "Lattice boltzmann simulations in microfluidics: probing the no-slip boundary condition in hydrophobic, rough, and surface nanobubble laden microchannels," *Microfluid. Nanofluid.*, vol. 8, no. 1, pp. 1–10, 2010.

[46] G. McHale and M. Newton, "Surface roughness and interfacial slip boundary condition for quartz crystal microbalances," *J. Appl. Phys.*, vol. 95, no. 1, pp. 373–380, 2004.

[47] O. Vinogradova, N. Bunkin, N. Churaev, O. Kiseleva, A. Lobeyev, and B. Ninham, "Submicrocavity structure of water between hydrophobic and hydrophilic walls as revealed by optical cavitation," *J. Colloid Interf. Sci.*, vol. 173, no. 2, pp. 443–447, 1995.

[48] C. Cottin-Bizonne, J.-L. Barrat, L. Bocquet, and E. Charlaix, "Low-friction flows of liquid at nanopatterned interfaces," *Nature Mater.*, vol. 2, no. 4, pp. 237–240, 2003.

[49] A. Maali, Y. Pan, B. Bhushan, and E. Charlaix, "Hydrodynamic drag-force measurement and slip length on microstructured surfaces," *Phys. Rev. E*, vol. 85, no. 6, p. 066310, 2012.

[50] R. S. Voronov, D. V. Papavassiliou, and L. L. Lee, "Review of fluid slip over superhydrophobic surfaces and its dependence on the contact angle," *Ind. Eng. Chem. Res.*, vol. 47, no. 8, pp. 2455–2477, 2008.

[51] J. P. Rothstein, "Slip on superhydrophobic surfaces," *Annu. Rev. Fluid Mech.*, vol. 42, pp. 89–109, 2010.

[52] R. Truesdell, A. Mammoli, P. Vorobieff, F. van Swol, and C. J. Brinker, "Drag

reduction on a patterned superhydrophobic surface," *Phys. Rev. Lett.*, vol. 97, no. 4, p. 044504, 2006.

[53] Y. C. Jung and B. Bhushan, "Biomimetic structures for fluid drag reduction in laminar and turbulent flows," *J. Phys.: Condens. Mat.*, vol. 22, no. 3, p. 035104, 2009.

[54] A. M. Davis and E. Lauga, "Hydrodynamic friction of fakir-like superhydrophobic surfaces," *J. Fluid Mech.*, vol. 661, pp. 402–411, 2010.

[55] B.-Y. Cao, M. Chen, and Z.-Y. Guo, "Liquid flow in surface-nanostructured channels studied by molecular dynamics simulation," *Phys. Rev. E*, vol. 74, no. 6, p. 066311, 2006.

[56] A. Steinberger, C. Cottin-Bizonne, P. Kleimann, and E. Charlaix, "High friction on a bubble mattress," *Nature Mater.*, vol. 6, no. 9, pp. 665–668, 2007.

[57] C.-O. Ng and C. Wang, "Effective slip for stokes flow over a surface patterned with two-or three-dimensional protrusions," *Fluid Dyn. Res.*, vol. 43, no. 6, p. 065504, 2011.

[58] L. Joly and T. Biben, "Wetting and friction on superoleophobic surfaces," *Soft Matter*, vol. 5, no. 13, pp. 2549–2557, 2009.

[59] E. Bonaccurso, H.-J. Butt, and V. S. Craig, "Surface roughness and hydro-

dynamic boundary slip of a newtonian fluid in a completely wetting system," *Phys. Rev. Lett.*, vol. 90, no. 14, p. 144501, 2003.

[60] X. Dai, B. B. Stogin, S. Yang, and T.-S. Wong, "Slippery wenzel state," *ACS Nano*, vol. 9, no. 9, pp. 9260–9267, 2015.

[61] C.-O. Ng and C. Wang, "Apparent slip arising from stokes shear flow over a bidimensional patterned surface," *Microfluid. Nanofluid.*, vol. 8, no. 3, pp. 361–371, 2010.

[62] E. S. Asmolov, J. Zhou, F. Schmid, and O. I. Vinogradova, "Effective slip-length tensor for a flow over weakly slipping stripes," *Phys. Rev. E*, vol. 88, no. 2, p. 023004, 2013.

[63] C. Wang, "Flow over a surface with parallel grooves," *Phys. Fluids*, vol. 15, no. 5, pp. 1114–1121, 2003.

[64] E. S. Asmolov, S. Schmieschek, J. Harting, and O. I. Vinogradova, "Flow past superhydrophobic surfaces with cosine variation in local slip length," *Phys. Rev. E*, vol. 87, no. 2, p. 023005, 2013.

[65] A. V. Belyaev and O. I. Vinogradova, "Effective slip in pressure-driven flow past super-hydrophobic stripes," *J. Fluid Mech.*, vol. 652, pp. 489–499, 2010.

[66] E. S. Asmolov, A. V. Belyaev, and O. I. Vinogradova, "Drag force on a sphere

moving toward an anisotropic superhydrophobic plane," *Phys. Rev. E*, vol. 84, no. 2, p. 026330, 2011.

[67] A. D. Stroock, S. K. Dertinger, G. M. Whitesides, and A. Ajdari, "Patterning flows using grooved surfaces," *Anal. Chem.*, vol. 74, no. 20, pp. 5306–5312, 2002.

[68] K. A. Sharp and B. Honig, "Electrostatic interactions in macromolecules: theory and applications," *Annu. Rev. Biophys. Bio.*, vol. 19, no. 1, pp. 301–332, 1990.

[69] B. Honig and A. Nicholls, "Classical electrostatics in biology and chemistry," *Science*, vol. 268, no. 5214, pp. 1144–1149, 1995.

[70] D. J. Harrison, K. Fluri, K. Seiler, Z. Fan, C. S. Effenhauser, A. Manz *et al.*, "Micromachining a miniaturized capillary electrophoresis-based chemical analysis system on a chip," *Science*, vol. 261, pp. 895–895, 1993.

[71] D. R. Reyes, D. Iossifidis, P.-A. Auroux, and A. Manz, "Micro total analysis systems. 1. introduction, theory, and technology," *Anal. Chem.*, vol. 74, no. 12, pp. 2623–2636, 2002.

[72] P. J. Kemery, J. K. Steehler, and P. W. Bohn, "Electric field mediated transport in nanometer diameter channels," *Langmuir*, vol. 14, no. 10, pp. 2884–2889, 1998.

BIBLIOGRAPHY

[73] T.-C. Kuo, L. A. Sloan, J. V. Sweedler, and P. W. Bohn, "Manipulating molecular transport through nanoporous membranes by control of electrokinetic flow: effect of surface charge density and debye length," *Langmuir*, vol. 17, no. 20, pp. 6298–6303, 2001.

[74] T.-C. Kuo, D. M. Cannon, Y. Chen, J. J. Tulock, M. A. Shannon, J. V. Sweedler, and P. W. Bohn, "Gateable nanofluidic interconnects for multilayered microfluidic separation systems," *Anal. Chem.*, vol. 75, no. 8, pp. 1861–1867, 2003.

[75] P. C. Hiemenz and R. Rajagopalan, *Principles of Colloid and Surface Chemistry*. CRC press, 1997, vol. 14.

[76] K. Seiler, Z. H. Fan, K. Fluri, and D. J. Harrison, "Electroosmotic pumping and valveless control of fluid flow within a manifold of capillaries on a glass chip," *Anal. Chem.*, vol. 66, no. 20, pp. 3485–3491, 1994.

[77] D. Q. Li, *Electrokinetics in Microfluidics*. Academic Press, 2004, vol. 2.

[78] R. J. Hunter, *Zeta Potential in Colloid Science: Principles and Applications*. Academic press, 2013, vol. 2.

[79] C. Yang and D. Li, "Analysis of electrokinetic effects on the liquid flow in rectangular microchannels," *Colloid Surf. A*, vol. 143, no. 2, pp. 339–353, 1998.

[80] D. Li, "Electro-viscous effects on pressure-driven liquid flow in microchannels," *Colloid Surf. A*, vol. 195, no. 1, pp. 35–57, 2001.

[81] Y. Hu, C. Werner, and D. Li, "Electrokinetic transport through rough microchannels," *Anal. Chem.*, vol. 75, no. 21, pp. 5747–5758, 2003.

[82] Y. Hu, C. Werner, and D. Q. Li, "Influence of the three-dimensional heterogeneous roughness on electrokinetic transport in microchannels," *J. Colloid Interf. Sci.*, vol. 280, no. 2, pp. 527–536, 2004.

[83] J. Wang, M. Wang, and Z. Li, "Lattice boltzmann simulations of mixing enhancement by the electro-osmotic flow in microchannels," *Mod. Phys. Lett. B*, vol. 19, no. 28n29, pp. 1515–1518, 2005.

[84] Z. Guo, T. Zhao, and Y. Shi, "A lattice boltzmann algorithm for electro-osmotic flows in microfluidic devices," *J. Chem. Phys.*, vol. 122, no. 14, p. 144907, 2005.

[85] J. Wang, M. Wang, and Z. Li, "Lattice poisson–boltzmann simulations of electro-osmotic flows in microchannels," *J. Colloid Interf. Sci.*, vol. 296, no. 2, pp. 729–736, 2006.

[86] N. A. Patankar and H. H. Hu, "Numerical simulation of electroosmotic flow," *Anal. Chem.*, vol. 70, no. 9, pp. 1870–1881, 1998.

[87] S. V. Ermakov, S. C. Jacobson, and J. M. Ramsey, "Computer simulations of

electrokinetic transport in microfabricated channel structures," *Anal. Chem.*, vol. 70, no. 21, pp. 4494–4504, 1998.

[88] M. Mitchell, R. Qiao, and N. Aluru, "Meshless analysis of steady-state electroosmotic transport," *J. MEMS.*, vol. 9, no. 4, pp. 435–449, 2000.

[89] R. Qiao and N. Aluru, "Ion concentrations and velocity profiles in nanochannel electroosmotic flows," *J. Chem. Phys.*, vol. 118, no. 10, pp. 4692–4701, 2003.

[90] R. Qiao and N. R. Aluru, "Atomistic simulation of kcl transport in charged silicon nanochannels: interfacial effects," *Colloid Surf. A*, vol. 267, no. 1, pp. 103–109, 2005.

[91] M. S. Kilic, M. Z. Bazant, and A. Ajdari, "Steric effects in the dynamics of electrolytes at large applied voltages. i. double-layer charging," *Phys. Rev. E*, vol. 75, no. 2, p. 021502, 2007.

[92] M. Kilic, M. Z. Bazant, and A. Ajdari, "Steric effects in the dynamics of electrolytes at large applied voltages. ii. modified poisson-nernst-planck equations," *Phys. Rev. E*, vol. 75, no. 2, p. 021503, 2007.

[93] I. Borukhov, D. Andelman, and H. Orland, "Steric effects in electrolytes: A modified poisson-boltzmann equation," *Phys. Rev. Lett.*, vol. 79, no. 3, p. 435, 1997.

[94] P. Wu and R. Qiao, "Physical origins of apparently enhanced viscosity of interfacial fluids in electrokinetic transport," *Phys. Fluids*, vol. 23, no. 7, p. 072005, 2011.

[95] J. Koplik and J. R. Banavar, "Continuum deductions from molecular hydrodynamics."

[96] D. Frenkel and B. Smit, *Understanding Molecular Simulation: from Algorithms to Applications*. Academic press, 2001, vol. 1.

[97] S. T. OConnell and P. A. Thompson, "Molecular dynamics–continuum hybrid computations: a tool for studying complex fluid flows," *Phys. Rev. E*, vol. 52, no. 6, p. R5792, 1995.

[98] X. Nie, S. Chen, M. Robbins *et al.*, "A continuum and molecular dynamics hybrid method for micro-and nano-fluid flow," *J. Fluid Mech.*, vol. 500, pp. 55–64, 2004.

[99] X. Nie, S. Chen, and M. O. Robbins, "Hybrid continuum-atomistic simulation of singular corner flow," *Phys. Fluids*, vol. 16, no. 10, pp. 3579–3591, 2004.

[100] X. Nie, M. O. Robbins, and S. Chen, "Resolving singular forces in cavity flow: multiscale modeling from atomic to millimeter scales," *Phys. Rev. Lett.*, vol. 96, no. 13, p. 134501, 2006.

[101] J. Liu, S. Chen, X. Nie, and M. O. Robbins, "A continuum–atomistic simulation

of heat transfer in micro-and nano-flows," *J. Comput. Phys.*, vol. 227, no. 1, pp. 279–291, 2007.

[102] J. Liu, S. Chen, X. B. Nie, and M. O. Robbins, "A continuum-atomistic multi-timescale algorithm for micro/nano flows," *Commun. in Comput. Phys.*, vol. 4, no. 5, pp. 1279–1291, 2008.

[103] N. G. Hadjiconstantinou, "Hybrid atomistic–continuum formulations and the moving contact-line problem," *J. Comput. Phys.*, vol. 154, no. 2, pp. 245–265, 1999.

[104] N. G. Hadjiconstantinou and A. T. Patera, "Heterogeneous atomistic-continuum representations for dense fluid systems," *Int. J. Mod. Phys. C*, vol. 8, no. 04, pp. 967–976, 1997.

[105] G. Wagner and E. Flekkoy, "Hybrid computations with flux exchange," *Phil. Trans. Roy. Soc. London A*, vol. 362, pp. 1655–1666, 2004.

[106] G. Wagner, E. Flekkøy, J. Feder, and T. Jøssang, "Coupling molecular dynamics and continuum dynamics," *Comput. Phys. Commun.*, vol. 147, no. 1, pp. 670–673, 2002.

[107] G. De Fabritiis, R. Delgado-Buscalioni, and P. Coveney, "Multiscale modeling of liquids with molecular specificity," *Phys. Rev. Lett.*, vol. 97, no. 13, p. 134501, 2006.

[108] R. Delgado-Buscalioni, E. Flekkøy, and P. Coveney, "Fluctuations and continuity in particle-continuum hybrid simulations of unsteady flows based on flux-exchange," *Europhys. Lett.*, vol. 69, no. 6, p. 959, 2005.

[109] R. Delgado-Buscalioni and G. De Fabritiis, "Embedding molecular dynamics within fluctuating hydrodynamics in multiscale simulations of liquids," *Phys. Rev. E*, vol. 76, no. 3, p. 036709, 2007.

[110] R. Delgado-Buscalioni, K. Kremer, and M. Praprotnik, "Concurrent triple-scale simulation of molecular liquids," *J. Chem. Phys.*, vol. 128, no. 11, p. 114110, 2008.

[111] R. Delgado-Buscalioni and A. Dejoan, "Nonreflecting boundaries for ultrasound in fluctuating hydrodynamics of open systems," *Phys. Rev. E*, vol. 78, no. 4, p. 046708, 2008.

[112] R. Delgado-Buscalioni, K. Kremer, and M. Praprotnik, "Coupling atomistic and continuum hydrodynamics through a mesoscopic model: Application to liquid water," *J. Chem. Phys.*, vol. 131, no. 24, p. 244107, 2009.

[113] E. Flekkøy, G. Wagner, and J. Feder, "Hybrid model for combined particle and continuum dynamics," *Europhys. Lett.*, vol. 52, no. 3, p. 271, 2000.

[114] E. G. Flekkøy, R. Delgado-Buscalioni, and P. V. Coveney, "Flux boundary

conditions in particle simulations," *Phys. Rev. E*, vol. 72, no. 2, p. 026703, 2005.

[115] W. E, W. Ren, and E. Vanden-Eijnden, "A general strategy for designing seamless multiscale methods," *Journal of Computational Physics*, vol. 228, no. 15, pp. 5437 – 5453, 2009.

[116] E. Weinan, B. Engquist, X. Li, W. Ren, and E. Vanden-Eijnden, "Heterogeneous multiscale methods: a review," *Commun. in Comput. Phys.*, vol. 2, no. 3, pp. 367–450, 2007.

[117] A. Donev, J. B. Bell, A. L. Garcia, and B. J. Alder, "A hybrid particle-continuum method for hydrodynamics of complex fluids," *Multiscale Model. Sim.*, vol. 8, no. 3, pp. 871–911, 2010.

[118] O. B. Usta, A. J. Ladd, and J. E. Butler, "lattice-boltzmann simulations of the dynamics of polymer solutions in periodic and confined geometries," *J. Chem. Phys.*, vol. 122, no. 9, p. 094902, 2005.

[119] O. B. Usta, J. E. Butler, and A. J. Ladd, "Flow-induced migration of polymers in dilute solution," *Phys. Fluids*, vol. 18, no. 3, p. 031703, 2006.

[120] G. Giupponi, G. De Fabritiis, and P. V. Coveney, "A coupled molecular-continuum hybrid model for the simulation of macromolecular dynamics," *Int. J. Mod. Phys. C*, vol. 18, no. 04, pp. 520–527, 2007.

[121] G. Giupponi, G. De Fabritiis, and P. Coveney, "Hybrid method coupling fluctuating hydrodynamics and molecular dynamics for the simulation of macromolecules," *J. Chem. Phys.*, vol. 126, no. 15, p. 154903, 2007.

[122] R. Kapral, "Multiparticle collision dynamics: simulation of complex systems on mesoscales," *Adv. Chem. Phys.*, vol. 140, p. 89, 2008.

[123] C. S. Peskin, "The immersed boundary method," *Acta numerica*, vol. 11, pp. 479–517, 2002.

[124] P. Ahlrichs and B. Dünweg, "Simulation of a single polymer chain in solution by combining lattice boltzmann and molecular dynamics," *J. Chem. Phys.*, vol. 111, no. 17, pp. 8225–8239, 1999.

[125] P. Ahlrichs, R. Everaers, and B. Dünweg, "Screening of hydrodynamic interactions in semidilute polymer solutions: A computer simulation study," *Phys. Rev. E*, vol. 64, no. 4, p. 040501, 2001.

[126] M. G. Fyta, S. Melchionna, E. Kaxiras, and S. Succi, "Multiscale coupling of molecular dynamics and hydrodynamics: application to dna translocation through a nanopore," *Multiscale Model. Sim.*, vol. 5, no. 4, pp. 1156–1173, 2006.

[127] T. T. Pham, U. D. Schiller, J. R. Prakash, and B. Dünweg, "Implicit and explicit solvent models for the simulation of a single polymer chain in solution: Lattice

boltzmann versus brownian dynamics," *J. Chem. Phys.*, vol. 131, no. 16, p. 164114, 2009.

[128] V. Lobaskin and B. Dünweg, "A new model for simulating colloidal dynamics," *New J. Phys.*, vol. 6, no. 1, p. 54, 2004.

[129] V. Lobaskin, B. Dünweg, and C. Holm, "Electrophoretic mobility of a charged colloidal particle: a computer simulation study," *J. Phys.: Condens. Mat.*, vol. 16, no. 38, p. S4063, 2004.

[130] V. Lobaskin, B. Dünweg, M. Medebach, T. Palberg, and C. Holm, "Electrophoresis of colloidal dispersions in the low-salt regime," *Phys. Rev. Lett.*, vol. 98, no. 17, p. 176105, 2007.

[131] A. Chatterji and J. Horbach, "Combining molecular dynamics with lattice boltzmann: A hybrid method for the simulation of (charged) colloidal systems," *J. Chem. Phys.*, vol. 122, no. 18, p. 184903, 2005.

[132] J. Smiatek, M. Sega, C. Holm, U. D. Schiller, and F. Schmid, "Mesoscopic simulations of the counterion-induced electro-osmotic flow: A comparative study," *J. Chem. Phys.*, vol. 130, no. 24, p. 244702, 2009.

[133] L. Bocquet and J.-L. Barrat, "Flow boundary conditions from nano-to micro-scales," *Soft matter*, vol. 3, no. 6, pp. 685–693, 2007.

[134] C. Denniston and M. O. Robbins, "General continuum boundary conditions for

miscible binary fluids from molecular dynamics simulations," *J. Chem. Phys.*, vol. 125, no. 21, p. 214102, 2006.

[135] O. I. Vinogradova, "Drainage of a thin liquid film confined between hydrophobic surfaces," *Langmuir*, vol. 11, no. 6, pp. 2213–2220, 1995.

[136] S. Plimpton, "Fast parallel algorithms for short-range molecular dynamics," *J. Comput. Phys.*, vol. 117, no. 1, pp. 1–19, 1995.

[137] G. S. Grest and K. Kremer, "Molecular dynamics simulation for polymers in the presence of a heat bath," *Phys. Rev. A*, vol. 33, no. 5, p. 3628, 1986.

[138] R. Khare, J. J. de Pablo, and A. Yethiraj, "Rheology of confined polymer melts," *Macromolecules*, vol. 29, no. 24, pp. 7910–7918, 1996.

[139] X. Yong and L. T. Zhang, "Thermostats and thermostat strategies for molecular dynamics simulations of nanofluidics," *J. Chem. Phys.*, vol. 138, no. 8, p. 084503, 2013.

[140] N. Tretyakov and M. Müller, "Correlation between surface topography and slippage: a molecular dynamics study," *Soft Matter*, vol. 9, no. 13, pp. 3613–3623, 2013.

[141] P. Hoogerbrugge and J. Koelman, "Simulating microscopic hydrodynamic phenomena with dissipative particle dynamics," *Europhys. Lett.*, vol. 19, no. 3, p. 155, 1992.

[142] P. Espanol and P. Warren, "Statistical mechanics of dissipative particle dynamics," *Europhys. Lett.*, vol. 30, no. 4, p. 191, 1995.

[143] M. S. Dresselhaus, G. Dresselhaus, and P. C. Eklund, *Science of Fullerenes and Carbon Nanotubes*. Academic press, 1996.

[144] T. W. Ebbesen, H. J. Lezec, H. Hiura, J. W. Bennett, H. F. Ghaemi, and T. Thio, "Electrical conductivity of individual carbon nanotubes," *Nature*, vol. 382, no. 6586, pp. 54–56, Jul 1996.

[145] R. H. Baughman, A. A. Zakhidov, and W. A. de Heer, "Carbon nanotubes–the route toward applications," *Science*, vol. 297, no. 5582, pp. 787–792, 2002.

[146] J. W. Mintmire, B. I. Dunlap, and C. T. White, "Are fullerene tubules metallic?" *Physical Review Letters*, vol. 68, pp. 631–634, Feb 1992.

[147] R. Saito, M. Fujita, G. Dresselhaus, and M. S. Dresselhaus, "Electronic structure of graphene tubules based on c_{60}," *Physical Review B*, vol. 46, pp. 1804–1811, Jul 1992.

[148] R. G. Horn and J. N. Israelachvili, "Direct measurement of structural forces between two surfaces in a nonpolar liquid," *J. Chem. Phys.*, vol. 75, no. 3, pp. 1400–1411, 1981.

[149] F. F. Abraham, "The interfacial density profile of a lennard-jones fluid in contact with a (100) lennard-jones wall and its relationship to idealized fluid/wall

systems: A monte carlo simulation," *J. Chem. Phys.*, vol. 68, no. 8, pp. 3713–3716, 1978.

[150] S. Toxvaerd, "The structure and thermodynamics of a solid–fluid interface," *J. Chem. Phys.*, vol. 74, no. 3, p. 1998, 1981.

[151] M. Plischke and D. Henderson, "Density profiles and pair correlation functions of lennard-jones fluids near a hard wall," *J. Chem. Phys.*, vol. 84, no. 5, pp. 2846–2852, 1986.

[152] I. Bitsanis, S. A. Somers, H. T. Davis, and M. Tirrell, "Microscopic dynamics of flow in molecularly narrow pores," *J. Chem. Phys.*, vol. 93, no. 5, pp. 3427–3431, 1990.

[153] I. Bitsanis and G. Hadziioannou, "Molecular dynamics simulations of the structure and dynamics of confined polymer melts," *J. Chem. Phys.*, vol. 92, no. 6, pp. 3827–3847, 1990.

[154] P. A. Thompson, M. O. Robbins, and G. S. Grest, "Structure and shear response in nanometer-thick films," *Isr. J. Chem.*, vol. 35, no. 1, pp. 93–106, 1995.

[155] J.-L. Barrat *et al.*, "Influence of wetting properties on hydrodynamic boundary conditions at a fluid/solid interface," *Faraday Discuss.*, vol. 112, pp. 119–128, 1999.

BIBLIOGRAPHY

[156] J. Koplik, J. R. Banavar, and J. F. Willemsen, "Molecular dynamics of fluid flow at solid surfaces," *Phys. Fluids A: Fluid*, vol. 1, no. 5, pp. 781–794, 1989.

[157] J. Gao, W. D. Luedtke, and U. Landman, "Layering transitions and dynamics of confined liquid films," *Phys. Rev. Lett.*, vol. 79, no. 4, p. 705, 1997.

[158] N. V. Priezjev, "Shear rate threshold for the boundary slip in dense polymer films," *Phys. Rev. E*, vol. 80, no. 3, p. 031608, 2009.

[159] N. Priezjev, "Relationship between induced fluid structure and boundary slip in nanoscale polymer films," *Phys. Rev. E*, vol. 82, no. 5, p. 051603, 2010.

[160] A. Niavarani and N. V. Priezjev, "Slip boundary conditions for shear flow of polymer melts past atomically flat surfaces," *Phys. Rev. E*, vol. 77, no. 4, p. 041606, 2008.

[161] L. Bocquet and J.-L. Barrat, "Hydrodynamic boundary conditions, correlation functions, and kubo relations for confined fluids," *Phys. Rev. E*, vol. 49, no. 4, p. 3079, 1994.

[162] N. V. Priezjev and S. M. Troian, "Molecular origin and dynamic behavior of slip in sheared polymer films," *Phys. Rev. Lett.*, vol. 92, no. 1, p. 018302, 2004.

[163] U. Heinbuch and J. Fischer, "Liquid flow in pores: slip, no-slip, or multilayer sticking," *Phys. Rev. A*, vol. 40, no. 2, p. 1144, 1989.

[164] M. O. Robbins and M. H. Müser, "Computer simulations of friction, lubrication and wear," *arXiv preprint cond-mat/0001056*, 2000.

[165] M. O. Robbins and M. H. Müser, "Computer simulations of friction, lubrication and wear," in *Modern Tribology Handbook*, B. Bhushan, Ed. Boca Raton, FL: CRC Press, 2001, pp. 717–765.

[166] N. V. Priezjev, "Molecular dynamics simulations of oscillatory couette flows with slip boundary conditions," *Microfluid. Nanofluid.*, vol. 14, no. 1-2, pp. 225–233, 2013.

[167] M. Whitby, L. Cagnon, M. Thanou, and N. Quirke, "Enhanced fluid flow through nanoscale carbon pipes," *Nano Lett.*, vol. 8, no. 9, pp. 2632–2637, 2008.

[168] M. Majumder, N. Chopra, R. Andrews, and B. J. Hinds, "Nanoscale hydrodynamics: enhanced flow in carbon nanotubes," *Nature*, vol. 438, no. 7064, pp. 44–44, 2005.

[169] J. Thomas and A. McGaughey, "Density, distribution, and orientation of water molecules inside and outside carbon nanotubes," *J. Chem. Phys.*, vol. 128, no. 8, pp. 84 715–84 900, 2008.

[170] A. Vanossi, N. Manini, M. Urbakh, S. Zapperi, and E. Tosatti, "Colloquium:

Modeling friction: From nanoscale to mesoscale," *Rev. Mod. Phys.*, vol. 85, no. 2, p. 529, 2013.

[171] S. K. Kannam, B. D. Todd, J. S. Hansen, and P. J. Daivis, "How fast does water flow in carbon nanotubes?" *J. Chem. Phys.*, vol. 138, no. 9, p. 094701, 2013.

[172] K. Huang and I. Szlufarska, "Green-kubo relation for friction at liquid-solid interfaces," *Phys. Rev. E*, vol. 89, no. 3, p. 032119, 2014.

[173] A. E. Kobryn and A. Kovalenko, "Molecular theory of hydrodynamic boundary conditions in nanofluidics," *J. Chem. Phys.*, vol. 129, no. 13, p. 134701, 2008.

[174] M. sbragaglia and A. Prosperetti, "Effective velocity boundary condition at a mixed slip surface," *J. Fluid Mech.*, vol. 578, pp. 435–451, 2007.

[175] M. Sbragaglia and A. Prosperetti, "A note on the effective slip properties for microchannel flows with ultrahydrophobic surfaces," *Phys. Fluids*, vol. 19, no. 4, p. 043603, 2007.

[176] L. Guo, S. Chen, and M. O. Robbins, "Slip boundary conditions over curved surfaces," *Phys. Rev. E*, vol. 93, p. 013105, Jan 2016.

[177] S. Cheng and M. O. Robbins, "Capillary adhesion at the nanometer scale," *Phys. Rev. E*, vol. 89, no. 6, p. 062402, 2014.

[178] N. V. Priezjev, "Molecular diffusion and slip boundary conditions at smooth surfaces with periodic and random nanoscale textures," *J. Chem. Phys.*, vol. 135, no. 20, p. 204704, 2011.

[179] M. Z. Bazant and O. I. Vinogradova, "Tensorial hydrodynamic slip," *Journal of Fluid Mechanics*, vol. 613, pp. 125–134, 2008.

[180] L. Hocking, "A moving fluid interface on a rough surface," *J. Fluid Mech.*, vol. 76, no. 04, pp. 801–817, 1976.

[181] S. Richardson, "On the no-slip boundary condition," *J. Fluid Mech.*, vol. 59, no. 04, pp. 707–719, 1973.

[182] E. Tuck and A. Kouzoubov, "A laminar roughness boundary condition," *J. Fluid Mech.*, vol. 300, pp. 59–70, 1995.

[183] D. Bechert and M. Bartenwerfer, "The viscous flow on surfaces with longitudinal ribs," *J. Fluid Mech.*, vol. 206, pp. 105–129, 1989.

[184] K. M. Jansons, "Determination of the macroscopic (partial) slip boundary condition for a viscous flow over a randomly rough surface with a perfect slip microscopic boundary condition," *Phys. Fluids*, vol. 31, no. 1, pp. 15–17, 1988.

[185] C. Pozrikidis, "Creeping flow in two-dimensional channels," *J. Fluid Mech.*, vol. 180, pp. 495–514, 1987.

[186] C. Soong, T. Yen, and P. Tzeng, "Molecular dynamics simulation of nanochannel flows with effects of wall lattice-fluid interactions," *Phys. Rev. E*, vol. 76, no. 3, p. 036303, 2007.

[187] R. Qiao and N. R. Aluru, "Multiscale simulation of electroosmotic transport using embedding techniques," *Int. J. Multiscale Comput. Eng.*, vol. 2, no. 2, 2004.

[188] J. Haile, "Molecular dynamics simulation: Elementary methods," *Comput. Phys.*, vol. 7, no. 6, pp. 625–625, 1993.

[189] M. P. Allen and D. J. Tildesley, *Computer simulation of liquids*. Oxford university press, 1989.

[190] P. Ahlrichs and B. Dünweg, "Lattice-boltzmann simulation of polymer-solvent systems," *Int. J. Mod. Phys. C*, vol. 9, no. 08, pp. 1429–1438, 1998.

[191] A. Chatterji and J. Horbach, "The role of effective charges in the electrophoresis of highly charged colloids," *J. Phys.: Condens. Mat.*, vol. 22, no. 49, p. 494102, 2010.

[192] S. Kohlhoff, P. Gumbsch, and H. Fischmeister, "Crack propagation in bcc crystals studied with a combined finite-element and atomistic model," *Philos. Mag. A*, vol. 64, no. 4, pp. 851–878, 1991.

[193] L. Landau and E. Lifshitz, "Fluid mechanics," 1959.

[194] R. F. Fox and G. E. Uhlenbeck, "Contributions to non-equilibrium thermodynamics. i. theory of hydrodynamical fluctuations," *Phys. Fluids*, vol. 13, no. 8, pp. 1893–1902, 1970.

[195] J.-P. Hansen and I. R. McDonald, *Theory of Simple Liquids*. Elsevier, 1990.

[196] J. M. O. De Zarate and J. V. Sengers, *Hydrodynamic Fluctuations in Fluids and Fluid Mixtures*. Elsevier, 2006.

[197] A. Donev, J. B. Bell, A. De la Fuente, and A. L. Garcia, "Enhancement of diffusive transport by non-equilibrium thermal fluctuations," *J. Stat. Mech.: Theory E.*, vol. 2011, no. 06, p. P06014, 2011.

[198] D. Bedeaux, I. Pagonabarraga, J. O. De Zárate, J. Sengers, and S. Kjelstrup, "Mesoscopic non-equilibrium thermodynamics of non-isothermal reaction-diffusion," *Phys. Chem. Chem. Phys.*, vol. 12, no. 39, pp. 12 780–12 793, 2010.

[199] J. Howard *et al.*, "Mechanics of motor proteins and the cytoskeleton," 2001.

[200] A. Evilevitch, L. Lavelle, C. M. Knobler, E. Raspaud, and W. M. Gelbart, "Osmotic pressure inhibition of dna ejection from phage," *P. Natl. A. Sci.*, vol. 100, no. 16, pp. 9292–9295, 2003.

[201] F. Balboa, J. B. Bell, R. Delgado-Buscalioni, A. Donev, T. G. Fai, B. E. Griffith, and C. S. Peskin, "Staggered schemes for fluctuating hydrodynamics," *Multiscale Model. Sim.*, vol. 10, no. 4, pp. 1369–1408, 2012.

[202] F. B. Usabiaga, I. Pagonabarraga, and R. Delgado-Buscalioni, "Inertial coupling for point particle fluctuating hydrodynamics," *J. Comput. Phys.*, vol. 235, pp. 701–722, 2013.

[203] F. B. Usabiaga, R. Delgado-Buscalioni, B. E. Griffith, and A. Donev, "Inertial coupling method for particles in an incompressible fluctuating fluid," *Comput. Method. Appl. M.*, vol. 269, pp. 139–172, 2014.

[204] P. J. Atzberger, "Velocity correlations of a thermally fluctuating brownian particle: A novel model of the hydrodynamic coupling," *Phys. Lett. A*, vol. 351, no. 4, pp. 225–230, 2006.

[205] P. J. Atzberger, P. R. Kramer, and C. S. Peskin, "A stochastic immersed boundary method for fluid-structure dynamics at microscopic length scales," *J. Comput. Phys.*, vol. 224, no. 2, pp. 1255–1292, 2007.

[206] P. J. Atzberger, "Stochastic eulerian lagrangian methods for fluid–structure interactions with thermal fluctuations," *J. Comput. Phys.*, vol. 230, no. 8, pp. 2821–2837, 2011.

[207] Y. Wang, J. K. Sigurdsson, E. Brandt, and P. J. Atzberger, "Dynamic implicit-solvent coarse-grained models of lipid bilayer membranes: Fluctuating hydrodynamics thermostat," *Physical Review E*, vol. 88, p. 023301, Aug 2013.

[208] J. Liu, M. Wang, S. Chen, and M. O. Robbins, "Molecular simulations of elec-

troosmotic flows in rough nanochannels," *J. Comput. Phys.*, vol. 229, no. 20, pp. 7834–7847, 2010.

[209] I.-C. Yeh and M. L. Berkowitz, "Ewald summation for systems with slab geometry," *J. Chem. Phys.*, vol. 111, no. 7, pp. 3155–3162, 1999.

[210] W. T. Coffey and Y. P. Kalmykov, *The Langevin Equation.* World Scientific, 2012.

[211] C. W. Gardiner, "Handbook of stochastic methods for physics, chemistry and the natural sciences, vol. 13 of," *Springer Series Syne.*, 1985.

[212] N. G. Van Kampen, *Stochastic Processes in Physics and Chemistry.* Elsevier, 1992, vol. 1.

[213] M. O. Robbins and M. H. Müser, "Computer simulations of friction, lubrication and wear," in *Handbook of Modern Tribology*, B. Bhushan, Ed. Boca Raton: CRC Press, 2000 (cond-mat/0001056), pp. 717–765.

[214] A. J. Ladd, R. Kekre, and J. E. Butler, "Comparison of the static and dynamic properties of a semiflexible polymer using lattice boltzmann and brownian-dynamics simulations," *Phys. Rev. E*, vol. 80, no. 3, p. 036704, 2009.

[215] N. K. Voulgarakis, B. Z. Shang, and J.-W. Chu, "Linking hydrophobicity and hydrodynamics by the hybrid fluctuating hydrodynamics and molecular dynamics methodologies," *Phys. Rev. E*, vol. 88, no. 2, p. 023305, 2013.

[216] A. M. Roma, C. S. Peskin, and M. J. Berger, "An adaptive version of the immersed boundary method," *J. Comput. Phys.*, vol. 153, no. 2, pp. 509–534, 1999.

[217] B. Dünweg and A. J. Ladd, "Lattice boltzmann simulations of soft matter systems," *Adv. Polym. Sci.*, vol. 221, p. 89, 2009.

[218] A. Chatterji and J. Horbach, "Electrophoretic properties of charged colloidal suspensions: Application of a hybrid md/lb method," *Math. Comput. Sim.*, vol. 72, no. 2, pp. 98–102, 2006.

[219] A. Brünger, C. L. Brooks, and M. Karplus, "Stochastic boundary conditions for molecular dynamics simulations of st2 water," *Chem. Phys. Lett.*, vol. 105, no. 5, pp. 495–500, 1984.

[220] L. Reichl, "A modern course in statistical physics," 1998.

[221] S. Delong, B. E. Griffith, E. Vanden-Eijnden, and A. Donev, "Temporal integrators for fluctuating hydrodynamics," *Phys. Rev. E*, vol. 87, no. 3, p. 033302, 2013.

[222] P. Español, J. G. Anero, and I. Zúñiga, "Microscopic derivation of discrete hydrodynamics," *J. Chem. Phys.*, vol. 131, no. 24, p. 244117, 2009.

[223] P. Español and I. Zúñiga, "On the definition of discrete hydrodynamic variables," *J. Chem. Phys.*, vol. 131, no. 16, p. 164106, 2009.

[224] A. Donev, T. G. Fai, and E. Vanden-Eijnden, "A reversible mesoscopic model of diffusion in liquids: from giant fluctuations to ficks law," *J. Stat. Mech.: Theory E.*, vol. 2014, no. 4, p. P04004, 2014.

[225] G. De Fabritiis, M. Serrano, R. Delgado-Buscalioni, and P. Coveney, "Fluctuating hydrodynamic modeling of fluids at the nanoscale," *Phys. Rev. E*, vol. 75, no. 2, p. 026307, 2007.

[226] B. E. Griffith, "An accurate and efficient method for the incompressible navier–stokes equations using the projection method as a preconditioner," *J. Comput. Phys.*, vol. 228, no. 20, pp. 7565–7595, 2009.

[227] J. Kim and P. Moin, "Application of a fractional-step method to incompressible navier-stokes equations," *J. Comput. Phys.*, vol. 59, no. 2, pp. 308–323, 1985.

[228] A. J. Chorin, "Numerical solution of the navier-stokes equations," *Math. comput.*, vol. 22, no. 104, pp. 745–762, 1968.

[229] J. B. Bell, P. Colella, and H. M. Glaz, "A second-order projection method for the incompressible navier-stokes equations," *J. Comput. Phys.*, vol. 85, no. 2, pp. 257–283, 1989.

[230] K. Mohamed and A. Mohamad, "A review of the development of hybrid atomistic–continuum methods for dense fluids," *Microfluid. Nanofluid.*, vol. 8, no. 3, pp. 283–302, 2010.

[231] R. Delgado-Buscalioni, "Tools for multiscale simulation of liquids using open molecular dynamics," in *Numerical Analysis of Multiscale Computations*. Springer, 2012, pp. 145–166.

[232] W. Ren, "Analytical and numerical study of coupled atomistic-continuum methods for fluids," *J. Comput. Phys.*, vol. 227, no. 2, pp. 1353–1371, 2007.

[233] R. Delgado-Buscalioni and P. Coveney, "Usher: an algorithm for particle insertion in dense fluids," *J. Chem. Phys.*, vol. 119, no. 2, pp. 978–987, 2003.

[234] J. P. Boon and S. Yip, *Molecular Hydrodynamics*. Courier Corporation, 1980.

[235] J. Keizer, *Statistical Thermodynamics of Nonequilibrium Processes*. Springer Science & Business Media, 2012.

[236] A. Donev, E. Vanden-Eijnden, A. Garcia, and J. Bell, "On the accuracy of finite-volume schemes for fluctuating hydrodynamics," *Commun. Appl. Math. Comput. Sci.*, vol. 5, no. 2, pp. 149–197, 2010.

[237] B. Dünweg and K. Kremer, "Molecular dynamics simulation of a polymer chain in solution," *J. Chem. Phys.*, vol. 99, no. 9, pp. 6983–6997, 1993.

[238] R. M. Jendrejack, D. C. Schwartz, M. D. Graham, and J. J. de Pablo, "Effect of confinement on dna dynamics in microfluidic devices," *J. Chem. Phys.*, vol. 119, no. 2, pp. 1165–1173, 2003.

[239] H. Hasimoto, "On the periodic fundamental solutions of the stokes equations and their application to viscous flow past a cubic array of spheres," *J. Fluid Mech.*, vol. 5, no. 02, pp. 317–328, 1959.

[240] I.-C. Yeh and G. Hummer, "System-size dependence of diffusion coefficients and viscosities from molecular dynamics simulations with periodic boundary conditions," *J. Phys. Chem. B*, vol. 108, no. 40, pp. 15 873–15 879, 2004.

[241] J. Lyklema, S. Rovillard, and J. De Coninck, "Electrokinetics: the properties of the stagnant layer unraveled," *Langmuir*, vol. 14, no. 20, pp. 5659–5663, 1998.

[242] J. B. Freund, "Electro-osmosis in a nanometer-scale channel studied by atomistic simulation," *J. Chem. Phys.*, vol. 116, no. 5, pp. 2194–2200, 2002.

[243] A. Beskok and G. E. Karniadakis, "Report: a model for flows in channels, pipes, and ducts at micro and nano scales," *Microscale Therm. Eng.*, vol. 3, no. 1, pp. 43–77, 1999.

[244] E. Spohr, "Computer simulation of the water/platinum interface," *J. Phys. Chem.*, vol. 93, no. 16, pp. 6171–6180, 1989.

[245] N. Cuvillier and F. Rondelez, "Breakdown of the poisson-boltzmann description for electrical double layers involving large multivalent ions," *Thin Solid Films*, vol. 327, pp. 19–23, 1998.

[246] S. Cui and H. Cochran, "Molecular dynamics simulation of interfacial electrolyte

behaviors in nanoscale cylindrical pores," *J. Chem. Phys.*, vol. 117, no. 12, pp. 5850–5854, 2002.

[247] M. J. Stevens and M. O. Robbins, "Melting of yukawa systems: a test of phenomenological melting criteria," *Europhys. Lett.*, vol. 12, no. 1, pp. 81–86, 1990.

[248] T. Das, D. Bratko, L. Bhuiyan, and C. Outhwaite, "Modified poisson-boltzmann theory applied to linear polyelectrolyte solutions," *J. Phys. Chem.*, vol. 99, no. 1, pp. 410–418, 1995.

[249] M. Deserno, C. Holm, and S. May, "Fraction of condensed counterions around a charged rod: Comparison of poisson-boltzmann theory and computer simulations," *Macromolecules*, vol. 33, no. 1, pp. 199–206, 2000.

[250] R. Messina, "Electrostatics in soft matter," *J. Phys.: Condens. Mat.*, vol. 21, no. 11, p. 113102, 2009.

[251] M. Gouy, "Sur la constitution de la charge electrique a la surface d'un electrolyte," *J. Phys. Theor. Appl.*, vol. 9, no. 1, pp. 457–468, 1910.

[252] D. L. Chapman, "Li. a contribution to the theory of electrocapillarity," *Philos. Mag.*, vol. 25, no. 148, pp. 475–481, 1913.

[253] R. R. Netz and H. Orland, "One and two-component hard-core plasmas," *Eur. Phys.l J. E*, vol. 1, no. 1, pp. 67–73, 2000.

[254] A. G. Moreira and R. R. Netz, "Binding of similarly charged plates with counterions only," *Phys. Rev. Lett.*, vol. 87, no. 7, p. 078301, 2001.

[255] A. G. Moreira and R. Netz, "Strong-coupling theory for counter-ion distributions," *Europhys. Lett.*, vol. 52, no. 6, p. 705, 2000.

[256] R. Netz, "Electrostatistics of counter-ions at and between planar charged walls: From poisson-boltzmann to the strong-coupling theory," *Eur. Phys.l J. E*, vol. 5, no. 1, pp. 557–574, 2001.

[257] L. Joly, C. Ybert, E. Trizac, and L. Bocquet, "Hydrodynamics within the electric double layer on slipping surfaces," *Phys. Rev. Lett.*, vol. 93, no. 25, p. 257805, 2004.

[258] T. Nishimura, Y. Ohori, and Y. Kawamura, "Flow characteristics in a channel with symmetric wavy wall for steady flow." *J. Chem. Eng. Jpn.*, vol. 17, no. 5, pp. 466–471, 1984.

[259] P. J. Atzberger, "Spatially adaptive stochastic multigrid methods for fluid-structure systems with thermal fluctuations," *arXiv preprint arXiv:1003.2680*, 2010.

Vita

Lin Guo was born in Linhai, Zhejiang Province, China. He received a B.S. degree in Mechanical Engineering, with a minor in Statistics from Peking University in Beijing, China, in 2008. In the fall of 2008, he was enrolled in the Department of Mechanical Engineering at Johns Hopkins University. He received his M.S.E. degree in Mechanical Engineering from Johns Hopkins University in 2010. His research focuses on molecular dynamics simulations and multi-scale modeling of micro- or nano-flows.